Optimization of Flow in a Flow Meter

Master Thesis

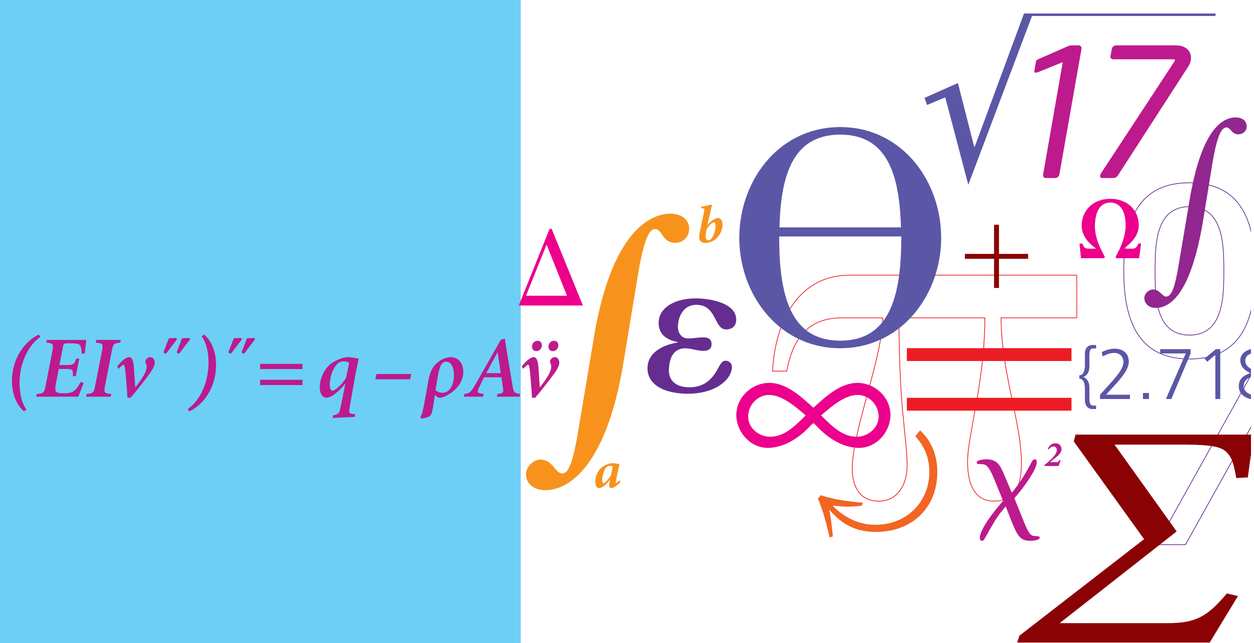

Áróra Björk Pétursdóttir
June 2017

DTU Mechanical Engineering
Department of Mechanical Engineering

ÁRÓRA BJÖRK PÉTURSDÓTTIR (S151321)

Optimization of flow in a flow meter

Master Thesis, June 2017

Supervisors:

Knud Erik Meyer, Professor at the Mechanical Engineering

Department of DTU

Torben Amby, Research Engineer at Danfoss

DTU - Technical University of Denmark, Kgs. Lyngby - 2017

Optimization of flow in a flow meter

This report was prepared by:
Áróra Björk Pétursdóttir (s151321)

Advisors:
Knud Erik Meyer, Professor at the Mechanical Engineering Department of DTU
Torben Amby, Research Engineer at Danfoss

DTU Mechanical Engineering
Fluid Mechanics, Costal and Maritime Engineering
Technical University of Denmark
Elektrovej, Building 326
2800 Kgs. Lyngby
Denmark
Tel: +45 4525 3576

info@mek.dtu.dk

Project period:	February 2017- June 2017
ECTS:	30
Education:	MSc
Field:	Mechanical Engineering
Remarks:	This report is submitted as partial fulfillment of the requirements for graduation in the above education at the Technical University of Denmark.
Copyrights:	

Abstract

Measurement of a fluid flow through a system is a critical parameter in many industrial processes. There are many different techniques used to measure the flow rate through a system, one of them being ultrasonic flow meters which are the subject of this thesis. Ultrasonic flow meters are used to measure the velocity of a fluid by transmitting and receiving ultrasound waves between two transmitters. This technique has become one of the most favored measurement methods for calculating volume flow since it has a high level of accuracy and does not include any moving parts.

The purpose of this study is to optimize the flow in an inline ultrasonic flow meter designed and produced by Danfoss A/S. The main goal of the research is to minimize pressure loss by optimizing the layout of a fixture inside the flow meter. This fixture holds two reflectors, used to transmit the ultrasonic signal between the transducers. The reflectors are positioned at an 45° angle perpendicular to the flow, therefore they cause quite the disturbance on the flow profile inside the pipe. The project was conducted using both experiments and CFD simulations. The prototypes used in the experiments were produced using rapid prototyping methodology. Multiple iterations were made during the design process, leading up to 19% improvement in the pressure drop. By implementing CFD into the analysis, the flow profiles could be studied to achieve a better understanding was gained on the effect of the flow meter to the flow.

Preface

This thesis was submitted in partial fulfillment of the requirement for the degree of Master of Science in Engineering (MSc) at the fluid mechanics section at the Technical University of Denmark (DTU). The thesis work was executed from 1st of February to 23rd of June 2017 and represents a workload of 30 ECTS. The thesis was written under the supervision of Knud Erik Meyer, associate professor at the Section of Fluid Mechanics, Coastal and Maritime Engineering. The industrial partner of the thesis is Danfoss A/S represented by Torben Amby, head of Mechanical Development & Technology in Energy Metering.

I would like to thank my supervisor, Knud Erik Meyer, for guidance and support and inspiration throughout the project. I would also like to thank my industrial supervisor at Danfoss, Torben Amby, for being there, giving good feedback and providing all the tools and materials for the research.

The reader is assumed to have an educational background at the same level of the author, but does not require particular knowledge or expertise within mechanical engineering to get a good understanding of the contents.

Áróra Pétursdóttir

Áróra Björk Pétursdóttir

Table of Contents

List of Figures

List of Tables

Nomenclature

Abbreviations

$2D$ Two Dimensional

$3D$ Three Dimensional

ABS Acrylonitrile Butadiene Styrene

CAD Computer Aided Design

CFD Computational Fluid Dynamics

CNC Computer Numerically Controlled

CV Control Volume

DN Diameter Nominal

DNS Direct Numerical Solving

FDM Finite Difference Method

FEM Finite Element Method

FVM Finite Volume Method

PC Polycarbonate

PLA PolyLactic Acid

$RANS$ Reynolds-Averaged Navier-Stokes

RP Rapid Prototyping

RSM	Reynolds Stress Transport Model	
UV	Ultraviolet	
IGES	Initial Graphics Exchange Specification	
SST	Shear Stress Transport	
STL	Stereolitography	

Dimensionless Numbers

Re	Reynolds Number	

Greek Symbols

ϵ	Roughness	$[\mathrm{mm}]$
κ	von Kárman Constant	$[-]$
μ	Dynamic viscosity	$[\mathrm{kg/(s\,m)}]$
μ_t	Eddy Viscosity	$\left[\mathrm{m^2/s)}\right]$
ν	Kinematic Viscosity	$\left[\mathrm{m^2/s}\right]$
ω	Specific Dissipation Rate	$\left[\mathrm{s^{-1})}\right]$
π	Pi	$[-]$
ρ	Density	$\left[\mathrm{kg/m^3}\right]$
τ	Stress Tensor	$\left[\mathrm{N/m^2}\right]$
ε	Energy Dissipation Rate	$[\mathrm{J/(kg \cdot s)}]$

Roman Symbols

$\bar{u}$	Mean Velocity	$[\mathrm{m/s}]$
ΔP	Pressure Drop	$[\mathrm{Pa}]$
$\mathbf{g}$	Gravitational Acceleration	$\left[\mathrm{m/s^2}\right]$
$\mathbf{U}$	Velocity vector	$[\mathrm{m/s}]$
A	Cross-sectional Area	$\left[\mathrm{m^2}\right]$
B	Log-layer Constant	$[-]$

D	Diameter	$[\mathrm{m}]$
D_H	Hydraulic Diameter	$[\mathrm{m}]$
f	Friction Factor	$[-]$
H	Total Head	$[\mathrm{m}]$
k	Coverage Factor	$[-]$
k	Kinetic Energy	$[\mathrm{J}]$
L	Pipe Length	$[\mathrm{m}]$
p	Pressure	$[\mathrm{Pa}]$
Q	Volumetric Flow Rate	$\left[\mathrm{m}^3/\mathrm{s}\right]$
q_c	Cutoff of Threshold Flow Rate	$\left[\mathrm{m}^3/\mathrm{h}\right]$
q_i	Minimum Legal Flow Rate	$\left[\mathrm{m}^3/\mathrm{h}\right]$
q_p	Nominal or Permanent Flow Rate	$\left[\mathrm{m}^3/\mathrm{h}\right]$
q_s	Maximum Legal Flow Rate	$\left[\mathrm{m}^3/\mathrm{h}\right]$
q_{ss}	Maximum Flow Rate	$\left[\mathrm{m}^3/\mathrm{h}\right]$
T	Time Averaging Period	$[\mathrm{s}]$
t	Time	$[\mathrm{s}]$
u	Velocity in the Flow Direction	$[\mathrm{m/s}]$
u'	Velocity of Fluctuations	$[\mathrm{m/s}]$
u^+	Dimensionless Near Wall Velocity	$[-]$
u_τ	Near Wall Velocity	$[\mathrm{m/s}]$
y	Distance From the Wall	$[\mathrm{m}]$
y^+	Dimensionless Distance From the Wall	$[-]$
Z	Elevation Head	$[\mathrm{m}]$

Mathematical Symbols

$\dfrac{\partial f(x,y)}{\partial x}$ Partial Derivative

$\frac{d\,y}{d\,x}$	Derivative
$\int$	Integral
∇	Gradient
$\sum$	Sum
E	Expanded Uncertainty
$e(y)$	Standard Uncertainty

CHAPTER 1

Introduction

Flow meter is a device that is used to measure the flow rate or quantity of gas or liquid that is moving through a pipe. There are many techniques that can be used to calculate the flow rate, each one more suitable to a certain application than the others. There is no universal flow meter that is the most suitable for all application, therefore the user must select the proper technology that matches his requirements in the best way. The flow meter that will be discussed in this project is an ultrasonic flow meter produced by Danfoss A/S. The flow meter comes in two different models, SonoSelect 10 and SonoSafe 10. In this chapter the SonoSelect 10 and SonoSafe 10 flow meters will be introduced, as well as the ultrasonic flow measuring technique will be discussed.

1.1 Ultrasonic Flow Meters

According to a half-century progress report that L.C. Lynnworth et al. [14] conducted in 2006, ultrasonic flow meters did not exist 60 years ago, which means that using ultrasonic signals to measure flow is a relative new technology. Nowadays it is however one of the fastest growing technologies within the field of instruments for process monitoring, measurement and control and it has been estimated that it represents about 12% of all flow meters sold. Considering the wide range of flow measuring technology, this is a high percentage.

Ultrasonic flow meters are based on a technology that uses sound waves to determine the velocity of a fluid flowing inside a pipe. When water flows through the pipe, an ultrasonic signal is simultaneously transmitted between two transducers. These signals are both sent in the upstream and downstream directions of the pipe. At no-flow conditions, it takes the same time to travel upstream and downstream between the transducers. Under flowing conditions, the upstream wave will travel slower and take more time than the (faster) downstream wave. When the fluid moves faster, the difference between the upstream and downstream times increases. The time difference between the signals is measured and used to calculate the flow velocity. Flow volume can then be precisely calculated based on the internal diameter of the pipe. Ultrasonic signals make it possible to measure velocity of water and calculate volume flow with the highest accuracy and most precise measurement in heat metering [1]. The measurement process can be explained by Figure 1.1 where two reflectors are used to send signal between the two transducers.

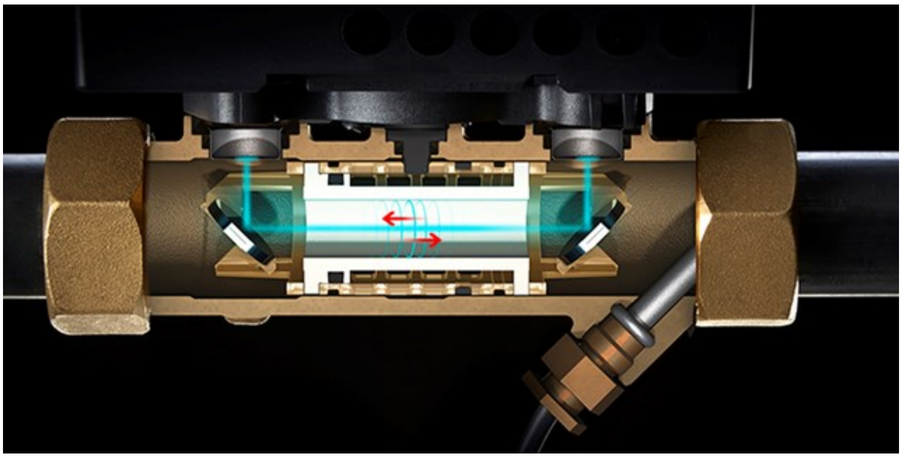

Figure 1.1: The measurement procedure in the SonoSelect flow meter. [1]

There are two types of ultrasonic flow meters, in-line flow meters and clamp-on flow meters. In-line meters are manufactured as a spool-piece with embedded transducers that is mounted directly into a pipeline (like the one in Figure 1.1), while in clamp-on configuration, transducers are mounted from the outside so the measurement does not affect the flow [20].

1.1.1 SonoSelect 10 and SonoSafe 10

The SonoSelect 10 and SonoSafe 10 flow meters are ultrasonic compact energy meters intended for measuring energy consumption in heating applications for billing purposes [5]. The two meters are identically designed but differ in some configurations, theses configurations are for example battery life, communication options with the meters, the measuring cycle and other. The flow measuring part of the meters is however the same and since this project was focused on exactly that, they will be referenced as a single flow meter from here on.

The flow meter consists of a flow sensor and a flow measuring circuit that is composed of electrical components. The flow sensor is the part that was of interest in this project. It consists of a brass spool piece, a liner, a liner fixture, two stainless steel ultrasonic transducers and two reflectors [6]. Furthermore, the energy meter consists of two temperature sensors, one on the inside of the pipe measuring the fluids temperature, and the other on the external, measuring the ambient temperature. An explanatory figure of the flow sensor unit with all the pieces can be seen in Figure 1.2.

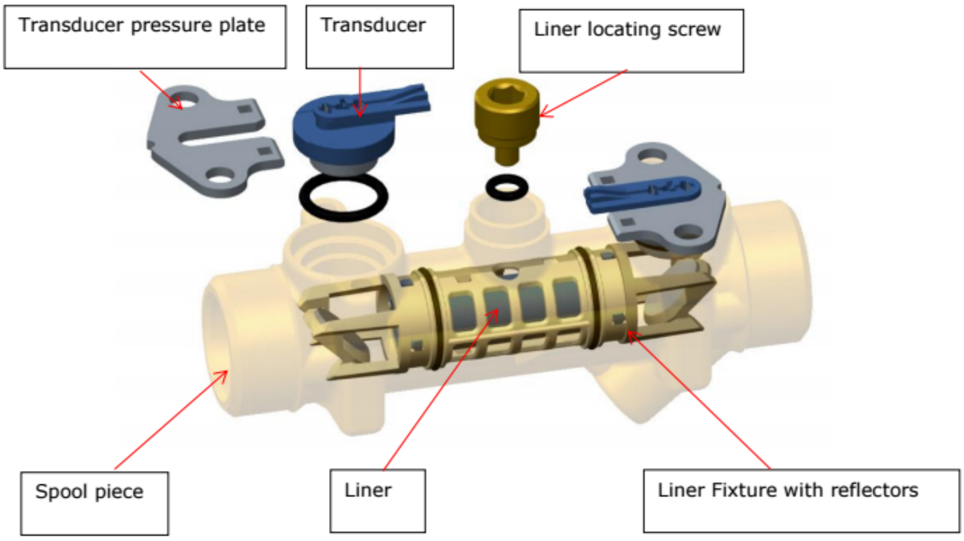

Figure 1.2: Explainatory figure of the parts of the flow meter. [6]

Like explained before (and can be seen in Figure 1.1), the two transducers send and receive signal from each other with the help of the two reflectors that are a part of the liner fixture. Inside the liner fixture is a liner which has a smaller diameter than the rest of the flow sensor. The liner is made from harder material than its fixture, this is due to acoustic reasons.

The optimization will concentrate on the liner fixture, which consists of two identical parts that are held together with O-rings. A more detailed drawing of the fixture part can be seen in Figure 1.3. As can be seen, the fixture can be divided into two major parts, the body and reflector part. The reflector is held in place by four arms, two on the upper half of the fixture and two on the lower half of the fixture. The dimensions of the liner fixture can be seen in Table A.1 in Appendix A.

The flow meter comes in five different variations, which differ in both diameter and nominal flow rate. The different variations and their nominal flow rates (q_p) can be seen in Table 1.1 as well as their cut-off flow rate (q_c), minimal flow rate (q_i), maximum legal flow rate (q_s) and maximum flow rate (q_{ss}).

This project focused on only one of these versions, the one of the nominal diameter 20 mm and with a nominal flow rate of 2.5 m^3/h.

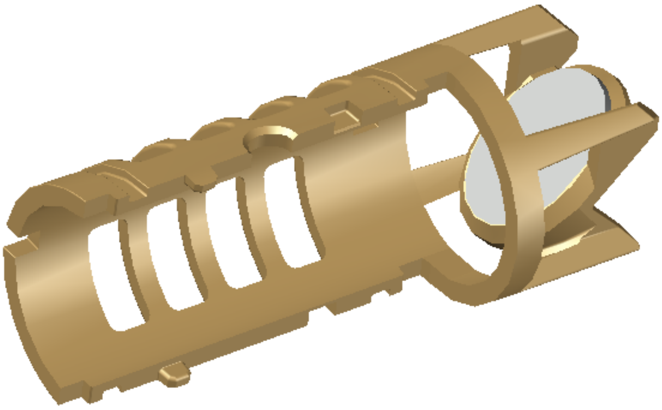

Figure 1.3: AutoCAD drawing of the flow meter fixture (DN50) with q_p = 2.5 m^3/h.

Table 1.1: Five variations of the flow meter. [6]

Size	q_c $[m^3/h]$	q_i $[m^3/h]$	q_p $[m^3/h]$	q_s $[m^3/h]$	q_{ss} $[m^3/h]$
DN15	0.0012	0.0060	0.6000	1.2000	1.2300
DN15	0.0030	0.0150	1.5000	3.0000	3.0750
DN20	0.0030	0.0150	1.5000	3.000	3.0750
DN20	0.0050	0.0250	2.5000	5.0000	5.1250
DN25	0.0070	0.0350	3.5000	7.0000	7.1750

1.2 Scope of the Thesis

The scope of this thesis was to optimize the flow meter with regards to the pressure drop. As stated before, the part that was worked on was the liner fixture. The fixture is the piece of the flow meter that holds the reflectors in place and since the reflectors are the parts that send the signal between the two transducers the size, shape, angle and position of them was something that could not be changed. Furthermore, the liner fixture is composed of two parts that must be identical due to ease of manufacturing.

This sets a lot of limitations regarding what could be done to minimize the pressure drop over the flow meter. By simply looking at the flow meter fixture it could be assumed that the reflectors are the critical parts that cause the loss in pressure, so these constraints will have a big influence on the results from this project. However, the flow meter was designed in the first place with mainly acoustics aspects in mind, so there should be some space for improvements regarding the flow pattern.

The work was conducted using both experiments and computational fluid dynamics (CFD). The experiments were performed using 3D printed prototypes in a special test-rig provided by Danfoss A/S. The simulations were conducted on the same prototypes by using the commercial CFD software, STAR-CCM+. Furthermore, it was investigated how shape optimization via 3D printing could be compared to CFD as an optimization tool. The flow through the meter had not been studied in this way before.

CHAPTER 2

Theory

This chapter is divided into three sections: Governing Equations, The Pipe Flow and The Numerical Modeling. In the first section the governing equations of flow are introduced. The second section describes the flow inside a pipe as well as it describes in which way the flow meter fixture effects the flow. The last section goes into the theory behind the numerical modeling.

2.1 Governing Equations

In all cases of flow, it must satisfy the three basic laws of mechanics, a thermodynamic state relation and associated boundary conditions [24]:

1. Conservation of mass.
2. Linear momentum (Newton's second law).
3. First law of thermodynamics (conservation of energy).
4. A state relation, like $\rho = \rho(p, t)$.
5. Appropriate boundary conditions at solid surfaces, interfaces, inlets and outlets.

In computational analysis, these five relations are modeled mathematically and solved by computational methods. By assuming that the fluid has a constant density (incompressible) and viscosity (Newtonian fluid), and that no thermal interaction is on the fluid, only the continuity and momentum equations are to be solved for velocity and pressure [24].

2.1.1 Continuity Equation

The continuity equation states that the rate of change of mass within its system is equal to zero [3]. Or in other words, the mass that goes into the system is equal to the mass that goes out of the system. This can also be expressed in the following way:

$$\frac{\partial \rho}{\partial t} + \nabla \cdot (\rho \mathbf{U}) = 0 \tag{2.1}$$

where ρ it the density of the fluid, t is the time and $\mathbf{U}$ denotes the velocity vector. If it is assumed that the fluid is incompressible (the density is constant), the continuity equation can therefore be simplified into the following form:

$$\nabla \cdot \mathbf{U} = \frac{\partial u}{\partial x} + \frac{\partial v}{\partial y} + \frac{\partial w}{\partial z} = 0 \tag{2.2}$$

where u, v and w are the time dependent velocity components. Equation (2.2) is called the three dimensional continuity equation for incompressible flow, the reason for that is because it expresses, in a mathematical way, that the flow is continuous [24].

This form of the continuity equation only deals with laminar flow cases. More detailed explanations for turbulent flow cases will be discussed later.

2.1.2 Momentum Equation

The conservation of momentum (Newton's second law) states that the rate of change of fluids momentum must be equal to the total external forces acting on the fluid. There are two kind of external forces acting on the fluid; gravity and viscous friction [3]. The momentum equation can be expressed in the following way:

$$\frac{\partial (\rho \mathbf{U})}{\partial t} + \nabla \cdot (\rho \mathbf{U}\mathbf{U}) = -\nabla p + \nabla \cdot \tau + \rho \mathbf{g} \tag{2.3}$$

where ρ is the density, $\mathbf{U}$ is the flow velocity vector, p is the pressure and τ is the stress tensor. The left side of the equation describes the acceleration, while the right side of the equation is a summation of the external forces. This form of the momentum equation is known by the name Cauchy momentum equation [24]. If it is assumed that the fluid is incompressible, the following assumption expression can be used for the stress tensor:

$$\tau = 2\mu \frac{1}{2}(\nabla \mathbf{U} + \nabla \mathbf{U}^T) \tag{2.4}$$

The divergence of the stress tensor is therefore given by:

$$\nabla \cdot \tau = 2\mu \nabla \cdot \epsilon = \mu \nabla \cdot (\nabla \mathbf{U} + \nabla \mathbf{U}^T) = \mu \nabla^2 \mathbf{U} \tag{2.5}$$

By inserting this into Equation (2.3), the momentum equation becomes:

$$\rho \left(\frac{\partial \mathbf{U}}{\partial t} + (\mathbf{U} \cdot \nabla)\mathbf{U} \right) = -\nabla p + \mu \nabla^2 \mathbf{U} + \rho \mathbf{g} \tag{2.6}$$

This form of the equation is known as the incompressible form of the Navier-Stokes equation. The first term in the equation represents the change in velocity over time. The second term is the change in momentum by convection. The third term is the change in pressure and the fourth term is the change in momentum due to diffusion. The fifth, and final term, represents the external forces on the fluid, or in other words the gravitational force [13].

As in the continuity equation, this form of the Navier-Stokes equation only deals with laminar flow cases. More detailed explanations for turbulent flow cases will be discussed later.

2.2 Pipe Flow

Fully developed turbulent pipe flows are the basis for most flow meter concepts and flow meters are usually calibrated in fully developed flow. A flow is considered to be fully developed when the velocity profile, $u(x, y)$, becomes independent of the downstream coordinate x, so that $u = u(y)$ [16].

Flow patterns in different fluid situations can be predicted by using the dimensionless quantity called the Reynolds number. The Reynolds number measures the relative importance of inertial and viscous forces and is used to predict whether the flow is laminar or turbulent and when it is in the transition in between. For flow in a pipe, the Reynolds number is defined as:

$$Re = \frac{Inertial forces}{Viscous forces} = \frac{\rho Q D_H}{\mu A} = \frac{Q D_H}{\nu A} \tag{2.7}$$

where Q is the flow rate, D_H is the hydraulic diameter, A is the pipe's cross-sectional area, ρ, μ and ν are the density, dynamic viscosity and kinematic viscosity of the fluid respectively. The hydraulic diameter is defined in such a way for pipes with a circular cross-section, that it reduces to its ordinary diameter, D. The flow in pipes is usually considered to be laminar if the Reynolds number is less than 2300 and turbulent if the Reynolds number is above 4000, hence

$$\begin{array}{cl} \text{Re} \leq 2300 & \text{Laminar flow} \\ 2300 \geq \text{Re} \leq 4000 & \text{Transitional flow} \\ \text{Re} \geq 4000 & \text{Turbulent flow} \end{array}$$

In laminar flow, the motion of the flow follows a well-defined and smooth path. That is, it has no unsteady mixing or overturning motion of the layers. While in turbulent flow, the motion of the fluid particles is irregular, or random, in a direction that is transverse to the direction of the main flow. This is often referred to as fluctuations [13]. The velocity distribution in a turbulent pipe flow is more uniform across the cross sectional area of the pipe than it is in a laminar flow, this is explained in Figure 2.1.

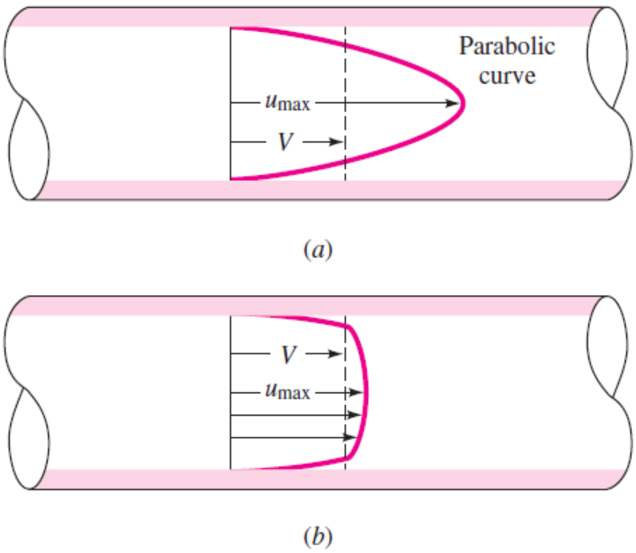

Figure 2.1: Comparison of laminar and turbulent pipe flow velocity profiles for the same volume flow: (a) laminar flow; (b) turbulent flow. [24]

As can be seen, the turbulent velocity profile is very flat in the center and drops sharply off to zero at the wall, while the laminar flow profile follows a parabolic curve.

Because of the fluctuations in turbulent flows, both the velocity and pressure are rapidly varying functions of time and space. The main interest is the mean values of the fluctuating variables, the time mean velocity, $\bar{u}$ of a turbulent function $(u(x, y, z, t))$, is defined by

$$\bar{u} = \frac{1}{T}\int_0^T u\,\mathrm{d}t$$

where T is the time averaging period that is taken to be longer than the significant period of the fluctuations themselves. The fluctuation u' is defined as the deviation of u from its average value,

$$u' = u - \bar{u} \tag{2.8}$$

This can be demonstrated in a better way with Figure 2.2, where both the mean and the fluctuating velocities are shown as a function of time.

In the same way, as with u, the other velocity variables, v and w, and the pressure, p, can also be decomposed into mean component and a fluctuating component, this is known as Reynolds averaging.

$$u = \bar{u} + u' \quad v = \bar{v} + v' \quad w = \bar{w} + w' \quad p = \bar{p} + p' \tag{2.9}$$

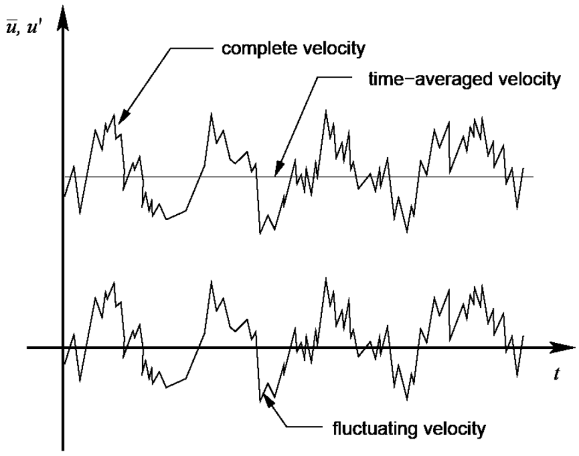

Figure 2.2: Definition of mean and fluctuating values. [12]

By definition, the mean value of the fluctuation is zero. However the mean square of the fluctuation, $\overline{u'^2}$, is not zero and is used as a measure of the intensity of the turbulence [24].

By implementing (2.9) into the Navier-Stokes equations, Eq. (2.2) and (2.6), and taking the time mean, the continuity equation reduces to:

$$\frac{\partial \bar{u}}{\partial x} + \frac{\partial \bar{v}}{\partial y} + \frac{\partial \bar{w}}{\partial z} = 0 \tag{2.10}$$

However, after time-averaging, each component of the momentum equation will contain mean values plus three mean products of fluctuating velocities. The x-component is the most important one, since it is in the direction of the main stream of the flow. The x-component of the momentum equation takes the following form:

$$\rho\frac{d\bar{u}}{dt} = -\frac{\partial \bar{p}}{\partial x} + \frac{\partial}{\partial x}\left(\mu\frac{\partial \bar{u}}{\partial x} - \rho\overline{u'^2}\right) + \frac{\partial}{\partial y}\left(\mu\frac{\partial \bar{u}}{\partial y} - \rho\overline{u'v'}\right) + \frac{\partial}{\partial z}\left(\mu\frac{\partial \bar{u}}{\partial z} - \rho\overline{u'w'}\right) + \rho g_x \tag{2.11}$$

The three correlation terms, $\rho\overline{u'^2}$, $\rho\overline{u'v'}$ and $\rho\overline{u'w'}$ are called turbulent stresses because they occur right alongside the laminar stress terms [24]. This form of the Navier-Stokes equations is better known as Reynolds-averaged Navier-Stokes equations (RANS).

2.2.1 Boundaries

The boundary surface divides the flow in a pipe into two main parts; the boundary region where there are viscous effects and the velocity changes are significant, and the core flow region where the frictional effects are negligible and the velocity remains essentially constant in the radial direction. The boundary region, or the near wall region, can further be divided into three layers; the viscous sublayer, the buffer layer and the log-law (inertial) sublayer.

Walls are a source of vorticity in most flow problems, therefore it is important to accurately predict the flow and turbulence parameters across the wall boundary layer. To describe the flow near a wall in the best way, a dimensionless wall distance, which is used to define layers in the region near the wall, must be presented

$$y^+ = \frac{yu_\tau}{\nu} \tag{2.12}$$

where y is the distance from the wall and u_τ is the near wall velocity and is defined as:

$$u_\tau = \sqrt{\frac{\tau_w}{\rho}} \tag{2.13}$$

where τ_w is the wall shear stress. In the wall layer, u must be independent of the shear layer thickness, thus another important dimensionless parameter must be introduced, the near wall velocity, which is defined as:

$$u^+ = \frac{u}{u_\tau} \tag{2.14}$$

in which u is the velocity parallel to the wall. [24]

Figure 2.3 shows the dimensionless wall velocity as a function of the dimensionless wall distance.

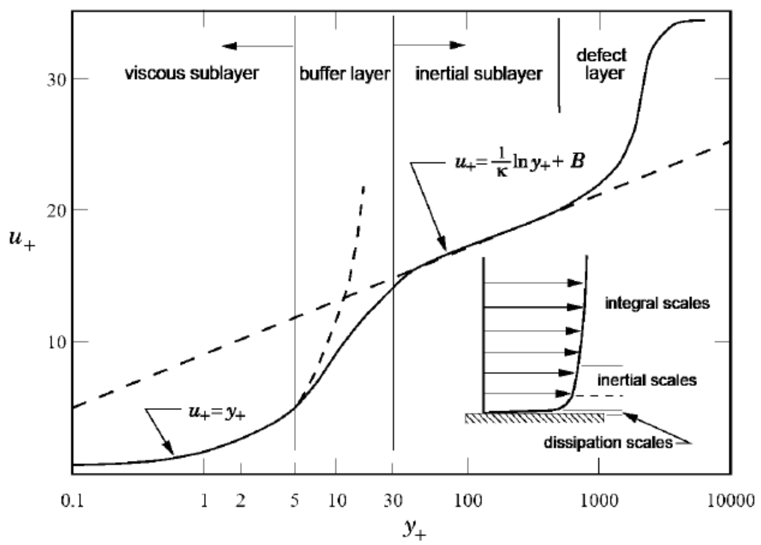

Figure 2.3: The non-dimensional velocity u^+ as a function of y^+. [12]

The viscous sublayer ($y^+ < 5$) is the region closest to the wall. That region is dominated by viscous shear effects and is almost laminar. There, the near wall velocity follows a curve where it is equal to the dimensionless distance from the wall ($u^+ = y^+$). The log-law layer ($30 < y^+ < 500$) is the boundary region which is the furthest from the wall without being in the outer region. It is dominated equally by viscous and turbulent effects [18]. The velocity profile in the log-law layer follows the following equation

$$u^+ = \frac{1}{\kappa}\ln(y^+) + B \tag{2.15}$$

where κ is the dimensionless von Kármán constant which has been found to have a value of 0.41 and B is the log-layer constant which is approximately equal to 5.0 for smooth walls [24]. The buffer layer ($5 < y^+ < 30$) is a transitional layer between the viscous sublayer and the log-law layer. An equation that describes the flow profile in the buffer layer does not exist but an interpolation between the viscous sublayer and the log-law layer can be used.

2.2.2 Effects of the flow meter on the flow

When fluid flows steadily within a long, straight pipe of uniform diameter, the flow pattern will follow a certain form, dependent of the flow velocity. Any obstacles inside the pipe, which changes the direction of the flow, or even just a part of the flow, will alter the characteristic flow pattern and create turbulence [21]. This creates loss of energy that is greater than the loss that normally occurs in a pipeline flow and are caused by the pipe walls. The total energy at any particular point in a straight pipe is equal to the sum of the elevation, the pressure and the velocity heads:

$$Z + \frac{p}{\rho g} + \frac{u^2}{2g} = H \tag{2.16}$$

where the first term in the equation, Z, is the elevation head, the second term is the pressure head, the third term is the velocity head and the last term, H, is the total head. The energy loss shows itself as a fall in pressure and varies with flow rate. The relationship between the flow rate and the pressure loss was first represented by Daniel Bernoulli in 1783 [24] and has since then become one of the fundamental equations in fluid dynamics. The general equation for pressure drop, known as Darcy's formula, is as follows:

$$\Delta P = \frac{\rho f L u^2}{2\,D} \tag{2.17}$$

where f is the friction factor that is dependent on the Reynolds number, diameter and the roughness of the material, and can be found in the Moody chart [24]. The Darcy equation is valid for both laminar and turbulent flow of any liquid in a straight pipe [2].

Many experiments have shown that the head loss due to constrictions in pipe flow is proportional to a square of the velocity. Since the flow pattern in fittings, valves, flow meters etc. is very complex, the theory around it is very weak. The losses are usually measured experimentally and correlated with the pipe flow parameters. The measured minor loss is usually given as a ratio of the head total loss, H, and the velocity head of the associated piping system. This value is known as the pressure loss coefficient and is calculated in the following way:

$$K = \frac{H}{u^2/(2g)} = \frac{\Delta P}{\frac{1}{2}\rho u^2} \tag{2.18}$$

where ΔP is the pressure drop between the inlet and outlet of the flow meter, ρ is the density of the fluid and u is the flow velocity.

The pressure loss in a piping system results from a number of system characteristics, which may be categorized as follows [2]:

1. The pipe friction, which is a function of the surface roughness of the interior pipe wall, the inside diameter and the Reynolds number.
2. Changes in the direction of flow path.
3. Obstructions in flow path.
4. Sudden or gradual changes in the cross-section and shape of flow path.

It is difficult to measure these effects separately and find out the pressure drop only due to the flow meters' fixture. The CFD simulations simulate a flow in a fully circular pipe with no imperfections other than the fixture inside. In order to compare the experimental results with the simulations in the best way possible, a well-known method was used. An additional experiment was run in the same way as all experiments, but without a fixture inside the flow meter. By doing so, the pressure drop due to other factors than the fixture, ΔP_0 can be subtracted from the pressure drop from the experimental results, ΔP_1. This can be explained better with Figure 2.4, where the lower figure represents the pressure drop caused by factors that are not the flow meter fixture. These factors are for example, a temperature sensor and diameter change between the pipe and the spool piece. By doing this, the pressure drop due to the fixture only, ΔP can be found and compared with results from simulations.

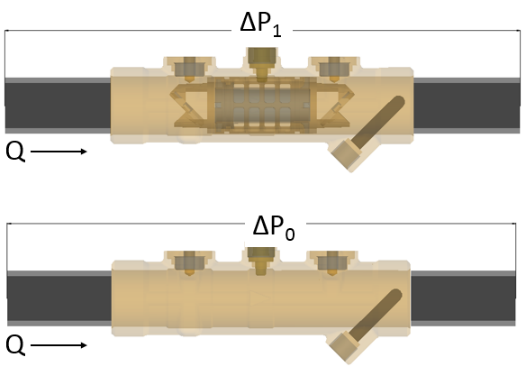

Figure 2.4: Explanatory figure of the spool piece with and without the liner and liner fixture.

2.3 Numerical Modeling

2.3.1 Finite Volume Method

Numerical modeling is the modern approach of solving and analyzing fluid flows. In numerical modeling, computers are used to perform the calculations that are required to simulate the interaction of gases and liquids with surfaces that are defined by boundary conditions. This technique can be used both on internal and external flows and is a very useful tool in industrial applications. There are three different main approaches in use in numerical modeling, they are [24]:

1. Finite Element Method (FEM)
2. Finite Difference Method (FDM)
3. Finite Volume Method (FVM)

The most common discretization approach in computational fluid dynamics, and the approach that STAR-CCM+ uses, is FVM. It is based on a technique that divides the total fluid volume into number of smaller control volumes (CVs). The conservation laws are then solved for each individual CV in the region, based on the neighboring CVs. Local conservation on each CV ensures global conservation over the entire fluid volume [3].

An attractive feature of this approach is that the numerical errors can only affect the conserved quantity of each CV, but not the total amount. This is unlike the FDM, where numerical errors can also lead to conservation errors [3].

2.3.2 Meshing

The method used to divide the fluid volume into the previously mentioned control volumes, is called meshing. The shape of each CV depends on the selected meshing technique. The mesh can both be structured or unstructured, the difference between those two is that the structured mesh follows an uniform pattern, while unstructured mesh does not. Therefore unstructured mesh is in general more flexible and gives a more accurate representation of a complex geometry than structured mesh. STAR-CCM+ offers a variety of meshers, which can be divided into three categories; surface meshers, volume meshers and mesh controls.

The technique that STAR-CCM+ uses when creating a mesh is to first create a surface mesh with its surface meshers. After the surface has been meshed in a satisfying way, the generated surface mesh is used to generate a volume mesh. There are a number of available volume meshers offered in STAR-CCM+, those meshers vary in the shape of the cells, or the CVs, and the difference between them can be seen in Figure 2.5.

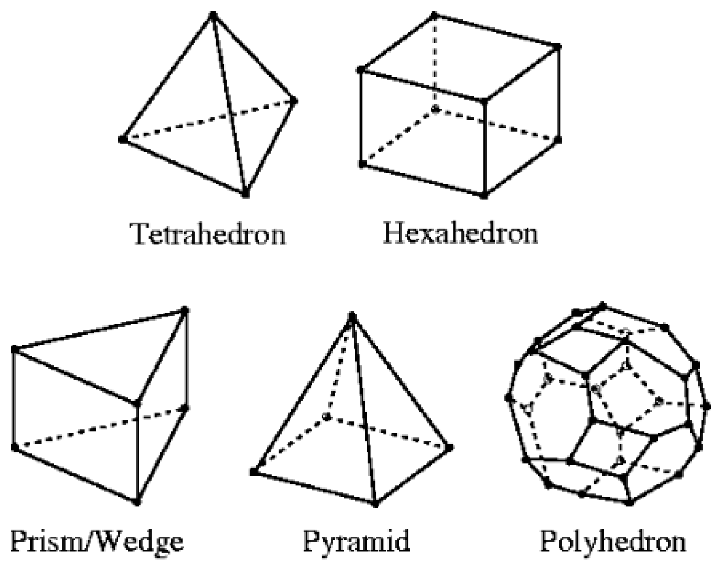

Figure 2.5: 3D cell types in numerical modeling.

Structured mesh is constructed of hexahedron shaped cells while the unstructured meshes are constructed of tetrahedron shaped cells. Several tetrahedrons can also be added together to create a polyhedron shaped mesh. Polyhedral mesh is in general a more complex mesh than a tetrahedral mesh and therefore it takes more effort to generate it. However, once the mesh is generated, it contains five times fewer cells than the tetrahedral mesh and can therefore pay off in the long run. Prism layers are used in the near wall regions of unstructured mesh in order to model the near wall boundary layer in the most accurate way.

An additional volumetric contol can also be applied to the mesh. This volumetric control is useful if there are certain parts of the geometry that require more attention than the rest of it. STAR-CCM+ also offers an extruder that generates an extrusion from the inlet or outlet to extend the flow visualization.

2.3.3 Turbulence models

The most accurate way to simulate turbulent flows is to use direct numerical simulation (DNS). The DNS method solves for the exact governing equations of turbulent flow and therefore has a high accuracy. However, it requires a very fine mesh and the computational cost is very high as the number of floating point operations grows as Re^3. So, for Reynolds number of a size usually encountered in an industrial application, the computational requirements of DNS would exceed even the capacity of the most powerful computers currently available [18].

Instead of solving the exact governing equations of turbulent flows (DNS), it is less computational demanding to solve for averaged, or filtered, quantities and approximate the impact of the small fluctuating structures. Turbulence models provide different approaches for modeling these structures. Many different turbulence models have been developed throughout the years and it is generally recognized that they all give an approximate representation of the physical phenomena of turbulence. The degree of approximation in each model depends on the nature of the flow it is used on. The turbulence models that are implemented in STAR-CCM+ can be divided into two categories; Reynolds-Averaged Navier-Stokes turbulence models and Scale-Resolving Simulations.

The Reynolds-Averaged Navier-Stokes (RANS) turbulence models provide closer relations for the RANS equations to solve for the transport of mean flow quantities. Two approaches of the RANS models are available in STAR-CCM+, they are the Eddy Viscosity Models and Reynolds Stress Transport Models (RSM).

The Eddy viscosity models are based on the analogy between the molecular gradient-diffusion process and turbulent motion. The concept of these models is that is it assumed that the turbulent flow contains small eddies that are constantly dissipating and forming. The Eddy viscosity models are for example, the Spallart-Allmaras Model, the k-ε Model, the k-ω Model, the Elliptic Blending Model and others. [18].

The Reynolds stress transport models are the most complex and computationally expensive models offered in STAR-CCM+. They are recommended for situations in which the turbulence is strongly anisotropic, or swirling, thus it is not applicable in the pipe flow case studied in this research [23].

In contrast to the RANS models, Scale-resolving Simulations are a transient technique that resolve the large scales of turbulence and model small scale motions. Two approaches of the Scale-Resolving Simulations are available in STAR-CCM+, they are Large Eddy Simulation and Detached Eddy Simulation [18]. Since the flow simulated in this research was considered to be stable, these turbulence models were not applicable.

After evaluating the flow, three different turbulence models were selected and tested, those models will be explained in more detail in the following subsections.

The k-ε Turbulence Model

The k-ε turbulence model is a two-equation model that determines the eddy (turbulent) viscosity, μ_t by solving transport equations for the turbulent kinetic energy, k, and its dissipation rate ε. The model gives a good compromise between robustness, computational cost and accuracy. The model is generally well suited for industrial applications, with, or without heat transfer [23].

The kinetic energy and the dissipation rate are calculated by using two different transport equations, one representing the kinetic energy and the other the eddy dissipation.

In its original form, the k-ε turbulence model was applied with wall functions, but was later modified to use either a Low-Reynolds Number Approach or a Two-Layer Approach for resolving the viscous sublayer.

The Low-Reynolds Number Approach is an approach that can be used to resolve the viscous sublayer. The approach applies damping factors on some or all the coefficients in the model. These factors modulate the coefficients as a function of a turbulent Reynolds number and often incorporate the wall distance.

The Two-Layer Approach is an alternative to the Low-Reynolds number approach that allows the k-ε model to be applied in the viscous sublayer. The approach divides the computation into two layers; a layer next to the wall and a layer further away from the wall. In the layer, next to the wall, the turbulent dissipation rate, ε, and the turbulent viscosity, μ_t, are specified as functions of wall distance.

One model of each kind was tested out in the flow modeling, the Realizable k-ε Two-Layer Model and the Standard Low-Re k-ε Model. The difference between the Realizable k-ε model and the Standard k-ε model is that the Realizable one is a newer model that is an improvement over the Standard one. STAR-CCM+ does however not offer a Realizable Low-Re model so the Standard model had to be selected.

The k-ω Turbulence Model

k-ω is a two-equation turbulence model that solves transport equations for the kinetic energy, k, and the specific dissipation rate, ω, to determine the turbulent viscosity. The original k-ω turbulence model has in the most significant advantage over the k-ε turbulence model that has improved performance for boundary layers under adverse pressure gradients.

There are two different versions of the k-ω model in Star-CCM+, the Standard k-ω and the SST k-ω. The Shear Stress Transport (SST) k-ω is a combination of both the k-ε model in the free stream and the Standard k-ω model near the walls. It does not use wall functions and tends to be most accurate when solving the flow near the wall.

The SST k-ω model was selected out of the two for this project since it was assumed that it would be important to solve for the viscous boundary layer.

CHAPTER 3

Methods & Materials

The project was carried out in a process that started with an initial idea. This idea was next sketched up in AutoCad. Once the prototype had been drawn, it was 3D printed. The prototype was then tested in experimental test-rig and the results were reviewed and evaluated. If the results were considered promising, CFD simulations were performed, else they were not. The idea was then refined, either with regards to the results or to follow up on a new and better idea. This process was repeated as often as thought was necessary. This process can be demonstrated by the cycle seen in Figure 3.1. Each step within the process cycle will be discussed in more detail in the following sections.

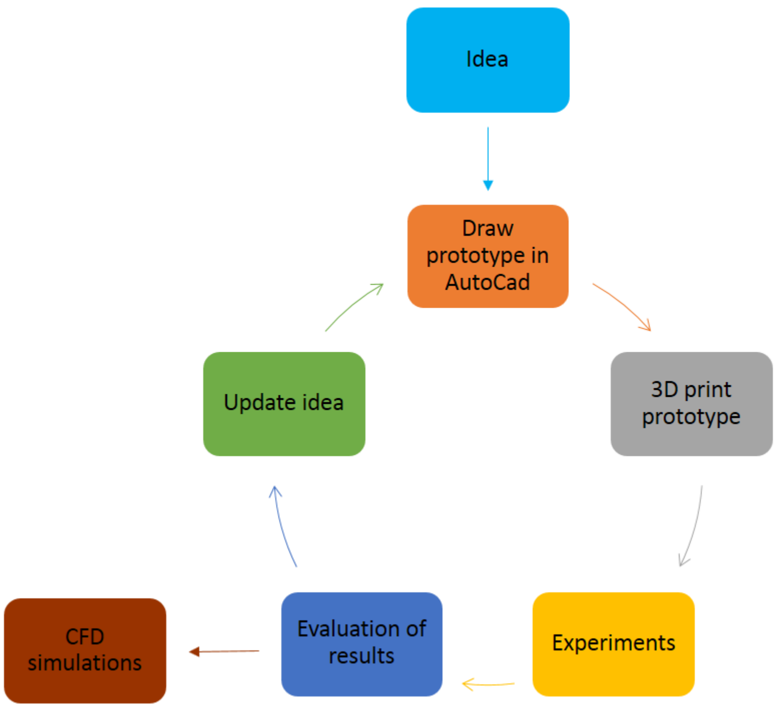

Figure 3.1: The work process; how it goes from an idea to a prototype to a CFD simulation.

3.1 Rapid prototyping

Rapid prototyping (RP) is used for direct manufacturing to quickly verify a design and fabricate a part. It is a technique for a direct conversion of three-dimensional CAD data into a physical prototype [22]. Figure 3.2 shows how general RP process works.

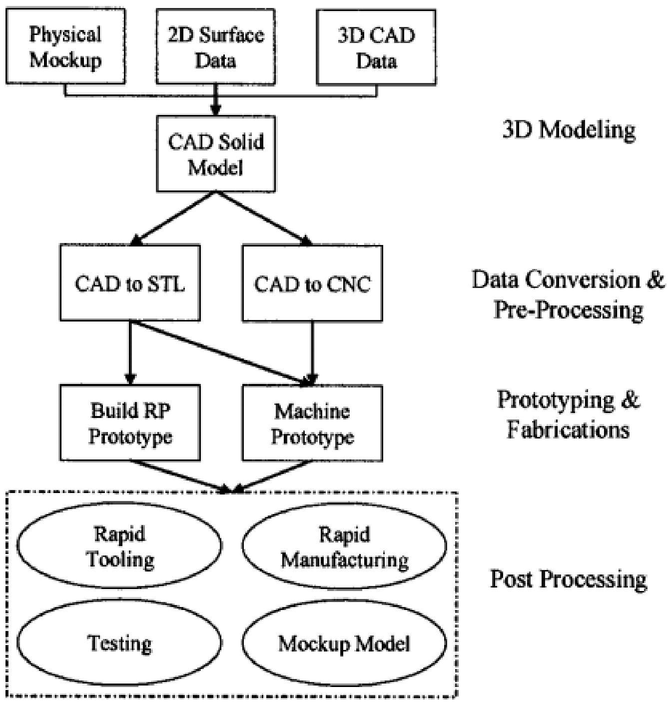

Figure 3.2: General RP process. [10]

All RP process starts with a CAD model. To draw such a model, AutoCad was used. The CAD drawing is then converted into Stereolithography data format. Stereolithography (STL), approximates the surface of the solid by using the least possible number of triangular faces with a normal vector pointing away from the surface in the solid [18]. In RP process, thin-horizontal-cross sections are used to transform materials into physical prototypes. The prototypes are then built using 3D printers or other devices [10]. Based on the device used to build the prototype, different post-processing methods have to be used, some require removal of supportive material, other require coating and some require nothing at all[22].

Three different types of 3D printers were used to create the prototypes, they are Afinia H800, Ultimaker2+ and FormLabs 2. The Afinia H800 printer was supplied by Danfoss while the other two are owned by DTU. At the beginning of the project, only the Afinia printer was used to print. It turned out to be very unstable and unreliable printer, but gave a good quality print. Too much time was spent repairing the printer and therefore a decision to switch over to the Ultimaker2+ printer was made. The Ultimaker2+ printer does not print with as good quality as the Afinia one, but it was all in all a more reliable printer that gave quicker results. Both the Afinia and the Ultimaker2+ printer are based on Fused Filament Fabrication. This type of 3D printers are the most common ones and are based on a technique where a plastic material is fed through a heated moving head. The head melts the material and extrudes it, depositing it, layer after layer, in the desired shape [10]. The third printer used was a high-quality printer of the type FormLabs2. This printer uses stereolithography technology which is a manufacturing process that works by focusing an ultraviolet (UV) laser on to a vat of photopolymer resin. The UV laser is then used to draw a pre-programmed design or shape on to the surface of the photopolymer vat. Because photopolymers are photosensitive under ultraviolet light, the resin is solidified and forms a single layer of the desired 3D object. This process is repeated for each layer of the design until the 3D object is fully formed [4].

PC-ABS material was used to print prototypes with the Afinia printer, while PLA material was used in the Ultimaker2+. The PC-ABS material is a combination of ABS and polycarbonate (PC), the ABS material is strong, ductile and heat tolerant, while the PC has extremely high temperature resistance. The PLA material does not have as high resistance for temperature as PC-ABS and is a more brittle and stiffer material. Tough resin was used in The FormLabs 2 printer. It is a material designed to simulate ABS plastic, with comparable tensile strength and modulus. It is perfect for functional prototyping and the sturdy, shatter-resistant material has been developed to withstand high stress and strain. [10]

Figure 3.3 features a sample print from all printers as well as the original geometry as it is manufactured by Danfoss.

Figure 3.3: Yellow: Original Flow Meter. Blue: High Quality 3D print from FormLabs 2. White: 3D print from Afinia H800. Silver: 3D print from Ultimaker2+.

3.2 Experiments in test-rig

Experiments on the flow meter prototypes were conducted in a test-rig provided by Danfoss. The experiments were conducted in the fluid laboratory facility at DTU during the period of March-June 2017. Figure 3.4 shows the experimental setup.

Figure 3.4: The test-rig provided by Danfoss.

3.2.1 The Test-rig

A rough sketch of the setup can be seen in Figure 3.5, the sketch shows all major parts of the setup along with the flow direction.

The water flows in the inlet of the rig and goes into the water circulation. The heating element was used to warm the water up to around 30°C. The setting of the heating elements was very sensitive to touch and therefore very un-precise to work with, the temperature of the water was therefore rocking from 28 - 32°C. This uncertainty in temperature did prove not to affect the resulting pressure drop in a significant way. Next, the water flows through the microbubble air separator which limits the amount of trapped air in the flow. The water then flows through the pump, which controls the flow rate of the system. The Alpha2 pump has three different operating modes so the flow can be controlled by three different methods; by proportional pressure curve, by a constant pressure curve and by constant speed [9]. The pump was set to be operating on a constant speed during the experiments. The speed can then be set in three different settings, but in order to take measurements at a wider range of flow rates, the flow rate was also controlled with an additional ball valve, marked number 9 on Figure 3.5. The water then flows through the reference flow meter which is of the type SonoSelect 10 with $q_p = 2.5$ m^3/h. Finally, the water flows through the flow meter to be tested. It is possible to dis-assembly the circuit in a way so the flow meter to be tested can be removed and the fixture inside can be changed. The pressure meter measures the pressure drop over the tested flow meter, the sensors are placed at a distance of 105 mm from the center of the flow meter. The Sitrans P DS III is a piezometer so it measures the pressure in two points and then calculates the difference between them [19]. The outlet in the circuit is placed lower than the rest of the system. This is done so the circuit can be emptied in a more efficient way. Before the water flows through the outlet, it flows past a pressure expansion tank. This tank is used to protect closed water heating systems from excessive pressure. The tank is partially filled with air, whose compressibility cushions shock caused by water hammer and absorbs excess water pressure caused by thermal expansion [11]. Additionally, the system features a safety valve, which lets out excess pressure from the circulation.

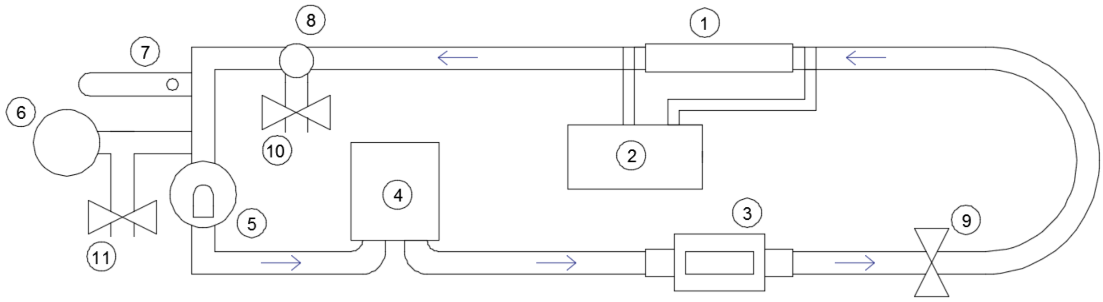

Figure 3.5: A sketch of the experimental setup.

The numbers in the sketch indicate the following:

1. Flow meter to be tested
2. Sitrans P DS III Pressure meter from Siemens [19]
3. SonoSelect 10 Reference flow meter [5]
4. Alpha2 pump from Grundfos [9]
5. Microbubble air seperator from Flamco [8]
6. Suprex Pressure expansion tank from Kierulff [11]
7. Heating element
8. Safety valve [7]
9. Ball valve to control flow
10. Inlet
11. Outlet

3.2.2 Experiment Procedure

The same procedure was followed for all experiments. To begin with, the desired fixture was placed in the flow meter to be tested and fastened with a screw. The circuit was then assembled back together and it was made sure that no leakage would occur. Once that had been done, the water was let into the circuit and the pump set to the highest flow rate setting. This setting usually resulted in a flow rate of approximately 1750 l/h. After the water was let in to the system, excess air was let out of the system. The system was then left undisturbed for a certain time until stability was reached in both water temperature, flow rate and pressure drop. After stability was reached, the results were noted down and the flow rate was lowered. Since the pump only had three different settings, a ball valve was used to get more measurement points. Once the system had reached stability again, the new results were noted down. This procedure was repeated until the last lowest achievable flow rate (around 100 l/h) was reached. However, due to high uncertainty in the measurements at those low flow rates, they were ignored in the comparisons. Once data from all measurement points was obtained, the circuit was emptied and disassembled to take the flow meter fixture out again. The last step was to inspect the fixture closely in order to see if it was still intact after the measurements.

3.2.3 The Fluid

The flow meter is used for measuring energy consumption in heating applications for billing purposes, the fluid of interest is therefore water. The temperature limit of the flow meters sensor is from 5 ^{o}C to 98 ^{o}C. Since the experimented featured 3D printed plastic-prototypes, that were easily deformed in high temperatures, a temperature that is not much higher than room-temperature was selected as a reference temperature. All experiments and simulations were therefore performed using water of 30 ^{o}C. The density and dynamic viscosity of water of that temperature are

$$\rho = 995.7 \mathrm{kg/m^3}$$

$$\mu = 0.801 \times 10^{-6} \mathrm{kg/(ms)}$$

As can be seen in Table 1.1, the flow rate in the flow meter can vary from 0.0050 m^3/h to 5.1250 m^3/h. The flow in the pipe is explained here with regards to the nominal flow rate. The Reynolds number, according to equation (2.7), for such a flow is $Re \approx 4.5 \times 10^4$, that means that the flow is turbulent and therefore dominated by inertial forces. The Reynolds number for the minimum flow rate is $Re \approx 450$, which means that for the lowest flow rates, the flow is laminar, the flow starts to turn turbulent when the flow rate is about 0.2 m^3/h and has become fully turbulent at around 0.3 m^3/h.

3.2.4 Error Estimation

When conducting an experiment, there are many factors that are unreliable and must be considered. Those errors are both due to time-varying conditions (such as temperature and so), and simply human errors. In order to minimize these errors, many things can be done, such as repeating measurements and having the eyes open for results that do not fit in with the rest. The error of a variable y ($y = f(x_1, x_2, ...x_N)$) is obtained by using the law of error estimation [15]:

$$e(y) = \sqrt{\sum_{i=1}^{N} \left(\frac{\delta f}{\delta x_i} e(x_i) \right)^2} \tag{3.1}$$

where $e(y)$ is the standard uncertainty and $e(x_i)$ is the standard uncertainty of each factor. The expanded uncertainty, E, is then obtained by multiplying the standard uncertainty with a coverage factor, k,

$$E = k\, e(y) \tag{3.2}$$

Common practice is to use $k = 2$, that corresponds to 95.4$\%$ confidence interval when the normal distribution applies [15]. By using the error estimation law (Equation (3.1)) to predict the size of the error for the pressure loss coefficient (Equation (2.18)) the following estimation is obtained:

$$e(K) = \sqrt{\left(\frac{1}{\frac{1}{2} D u^2} e(\Delta P) \right)^2 + \left(\frac{\Delta P}{\frac{1}{2} D^2 u^2} e(D) \right)^2 + \left(\frac{\Delta P}{\frac{1}{2} D u^3} e(u) \right)^2} \tag{3.3}$$

where the flow velocity, u, is obtained by using the following conversion equation:

$$u = \frac{Q}{\frac{1}{4} D^2 \pi} \tag{3.4}$$

and the error on the flow velocity is estimated in the same way as before as:

$$e(u) = \sqrt{\left(\frac{1}{\frac{1}{4} D^2 \pi} e(Q) \right)^2 + \left(\frac{Q}{\frac{1}{4} D^3 \pi} e(D) \right)^2} \tag{3.5}$$

The error for each factor was estimated for each factor in the experiment. The estimated errors can be seen in the Appendix A.2.

3.3 The CFD Simulation Setup

In the following sections, it will be described how the simulations were executed. The flow in the experimental test-rig was considered to be stable, therefore only stable simulations were performed. The difference between steady and transient simulations are that steady state simulations eliminate the time parameter from the turbulent transportation equations.

3.3.1 Geometry

All geometry models were created in AutoCad. The 3D-CAD models that were used in the CFD simulations were a simplified version of the versions that were tested in the experiments. All the details of the original meter that were negligible, like holes in the fixtures body, O-rings, hole for screw, screw, etc., were dismissed. The liner was then submerged with the fixture to create a one piece geometry. This was done in order to avoid having to perform surface repair or Boolean operations on the geometry in the CFD software. The most important part of the geometry, the mirror and its arms, were kept in full detail, as they are the most important part of the geometry and the part of interest in this report. Figure 3.6 shows the difference of the geometry used in the experiments and the geometry imported into STAR-CCM+.

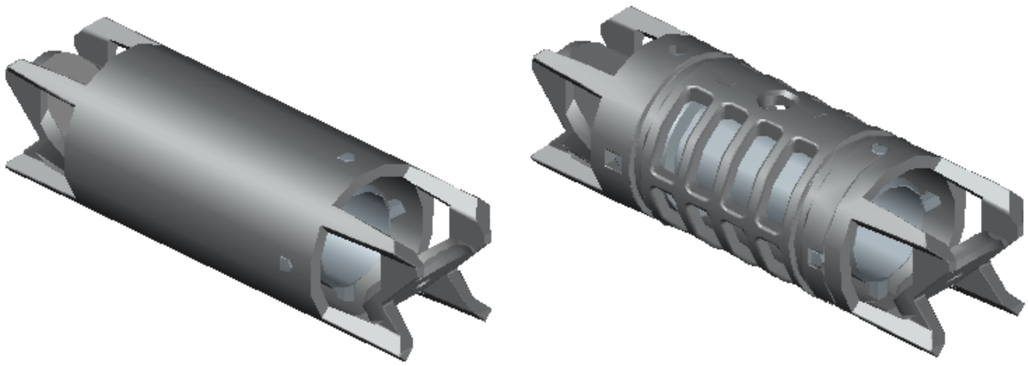

Figure 3.6: Original geometry as it was imported into STAR-CCM+ on the left and the original geometry as it was tested in experiments on the right.

The fixture geometry was imported into STAR-CCM+ from a IGES file and thus represented initially as a CAD part. A flow domain was then created in STAR-CCM+ by creating a simple cylinder to represent the inside of the pipe.

3.3.2 Mesh

In order to get as accurate results as possible, the mesh has to be well thought through. In general, it applies that the finer the mesh is, the more accurate the results are. Since the geometry is quite complex, the mesh must be quite fine to catch all details.

The generated meshes were created by first applying the Surface wrapper, which wraps the surface up and creates a closed, manifold, non-intersecting surface. This type of mesher is typically used when the imported geometry is either of poor quality or it is complex with many details. The surface wrapper can be used to close holes, gaps and mismatches as well as it can be used to remove internal features and unwanted details [18]. The resulting surface quality after applying the surface wrapper is poor, therefore, in order to result in a high quality starting surface for the volume meshers, it is used alongside the Surface remesher. The Surface mesher is used to retriangulate the surface to improve the overall quality of the existing surface mesh. After a suitable surface mesh had been generated, the next step was to create a volume mesh. A decision was made to use the Polyhedral mesher, since it is well suited for complex geometries. The Prism Layer mesher was used as well in order to improve the flow solution next to wall surfaces. The Prism Layer mesher creates orthogonal prismatic cells next to wall surfaces or boundaries. The last mesher used was the Extruder. It was used to extend the flow field from the outlet to visualize the flow after the fixture without increasing the number of cells in the way they would be increased if the cylindrical pipe would be elongated and meshed in the same way as the rest of the flow region. The resulting mesh, with a base size of 1 mm, 7 prism layers and an extrusion of 50 mm divided into 10 layers, is shown in Figure 3.7.

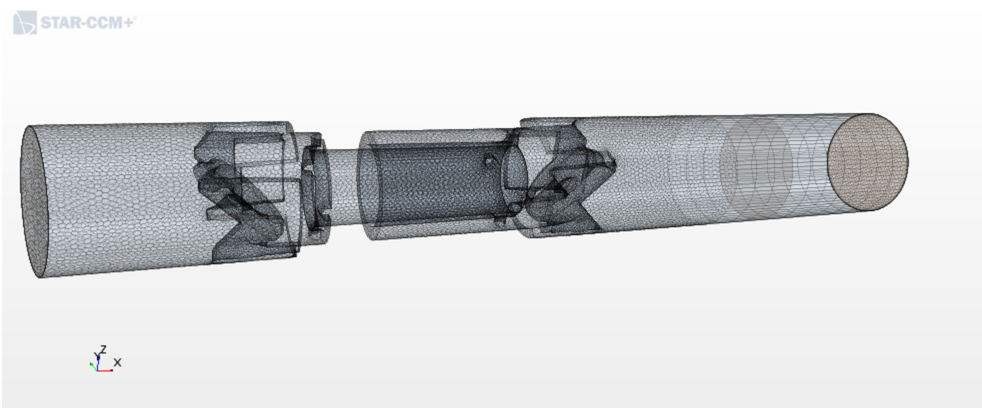

Figure 3.7: The mesh used in the simulations. This is the original geometry.

3.3.3 Boundary Conditions

To achieve a successful solution, it is vital to set the boundary conditions correctly. The two most widely known boundary conditions are the Dirichlet and the Neumann boundary conditions. In mathematical terms, Dirichlet boundary conditions are value specified, while Neumann boundary conditions are flux specified [17]. STAR-CCM+ offers a variety of different boundary conditions, each one more applicable than the others to simulate its own certain things.

The pipe wall and the fixture were set as walls. The Wall boundary condition can either be a slip, or a no-slip boundary condition. The no-slip condition assumes that at a solid boundary, the fluid will have zero velocity relative to the boundary [24]. Since the solution is prescribed at certain locations, this is an example of a Dirichlet boundary condition. The slip boundary condition computes the velocity at the wall by extrapolating the parallel component of velocity in the adjacent cell using reconstruction gradients [18], this is a Neumann type boundary condition. The no-slip boundary condition was assumed to be more applicable in this case. Furthermore, the wall surface specification can either be set as smooth or rough. Brass has a roughness of $\epsilon = 0.002$mm and plastic of $\epsilon = 0.0015$mm [24], which are small values compared to the diameter of the objects. The walls can therefore be assumed to be smooth.

The pipe inlet was set as a mass flow inlet. The mass flow inlet is a Dirichlet type boundary condition where the mass flow of the face is specified. The boundary face pressure is extrapolated from the adjacent cell using reconstruction gradients [18]. This boundary condition was thought to be the most applicable one of the inlet boundary conditions offered by STAR-CCM+.

Finally, the pipe outlet was set as a pressure outlet. The pressure outlet boundary condition is a Dirichlet boundary condition that lets the user specify the boundary pressure [18]. The boundary pressure was set as 0 Pa in the simulation, in that way the inlet pressure could give a good representation of the pressure drop over the fixture in the flow.

Like explained in Section 2.2.1, wall treatment is important in order to catch the viscous flow in the near wall region. STAR-CCM+ provides three kinds of wall treatment dependent on the turbulence model used. The wall treatments are; Low $y+$ wall treatment, High $y+$ wall treatment and All $y+$ wall treatment. The difference between the treatments is in the way they solve the viscous sublayer. The Low $y+$ wall treatment solves it, but the High y+ wall treatment does not and assumes that the near wall cells lie within log-law layer. The All $y+$ wall treatment is a mixture of the other two wall treatments and emulates the Low y+ wall treatment for fine meshes and the High $y+$ wall treatment for coarse meshes. This mixture produces a reasonable answer for meshes of intermediate resolution. It is recommended by STAR-CCM+ to use the All $y+$ wall treatment whenever it is available, this was followed in this project.

In order to solve for the viscous sublayer, the $y+$ value has to be less than five, like stated in Section 2.2.1. The values of $y+$ can be plotted in STAR-CCM+ and Figure 3.8 gives a good example of the wall treatment in the simulations. As can be seen, the $y+$ are all below five, which means that they the model solves for the viscous sublayer.

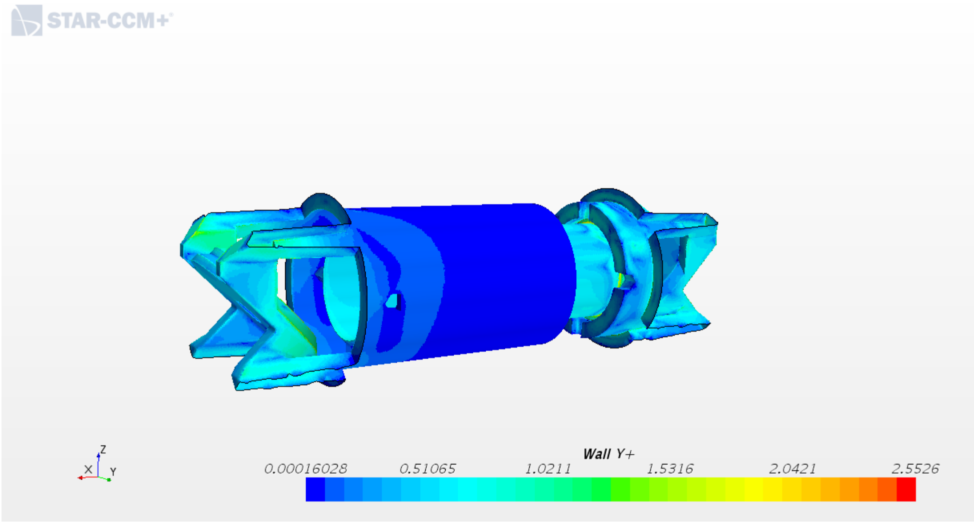

Figure 3.8: An example of values for $y+$ on the walls of the fixture.

3.3.4 Recording of Pressure Drop

The pressure drop was recorded in such a way that a surface average of the pressure was taken, both at a certain distance in front of the flow meter and at a certain distance after the flow meter. In order to get results that are were comparable to the experimental results, this distance was set as the same distance as the pressure is measured away from the flow meter in the experiments. That was 105 mm both in front and after the center of the flow meter. The surface average of the pressure in the outlet was then subtracted from the surface average of the pressure in the inlet. An example of a pressure drop monitor can be seen in Appendix A.3.

3.3.5 Visual Evaluation

The solutions of the simulations were evaluated using both horizontal and vertical planes as well as a line through the center of the geometry. The planes and line are presented in Figure 3.9. By doing this, all prototypes could be compared in a better way.

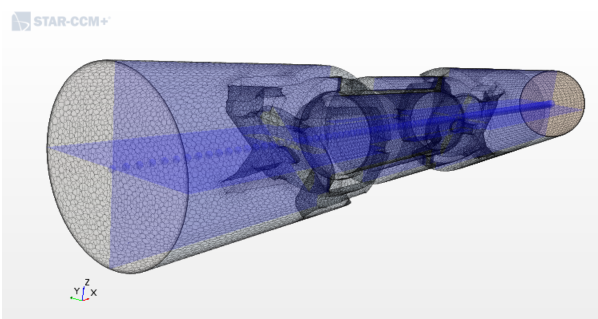

Figure 3.9: The two planes and line used to evaluate the results.

CHAPTER 4

Validation

4.1 Validation of Experimental Results

In order to validate whether the experimental setup and the fast prototyping would give correct results, a number of initial test were performed. Both versions of the actual fixture for pipes of sizes DN20, produced by Danfoss were first tested. A 3D printed version (printed with the Ultimaker2+) of the 2.5 m^3/h meter was tested and compared to the original one. In addition to this, a 3D printed version of the fixture that was used in the CFD simulations (see Figure 3.6) was tested in order to see if the simplification made to the model in the numerical simulations would affect the pressure drop in a significant way. The results from theses tests can be found in Appendix A.5. The experimental results can then be compared to the pressure drop chart from the flow meters data sheet, shown in Figure 4.1.

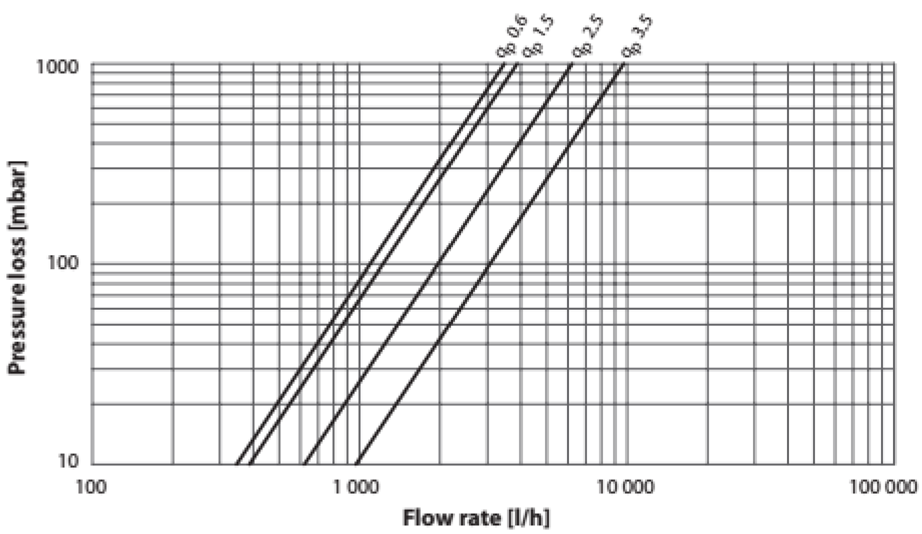

Figure 4.1: Pressure drop graph for all sizes of the flow meter. [5]

It can be noticed that the results presented in Figure 4.1 cover much wider flow range than the results from the experiments. This is due to the fact that the highest flow rate that could be reached with the experimental test rig was around 1.7 l/h. A comparison between the original geometry and the two 3D printed versions as well as the results read from Figure 4.1, is presented in Figure 4.2. As can be obtained, the 3D printed versions are both within 10% deviation from the original geometry. Larger deviations are experienced in the curve from the official values than the other two, this is due to how hard it was to read off the chart in Figure 4.1. These results show that the rapid prototyping gives adequate results compared to the original fixture as well as the experimental values are compatible to the official pressure drop that Danfoss publishes.

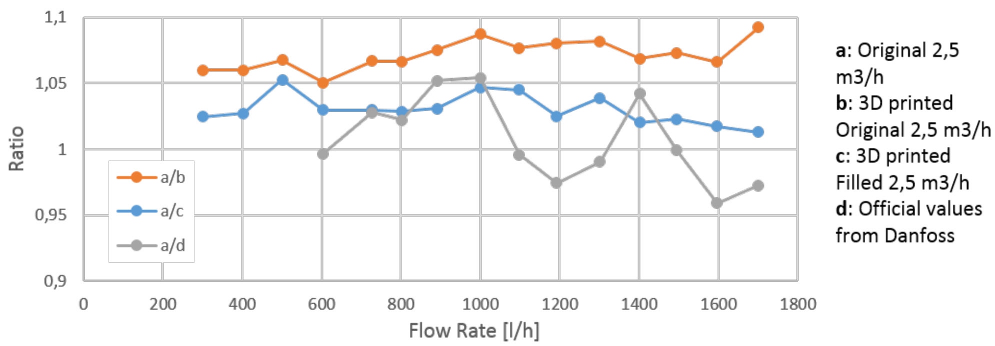

Figure 4.2: Validation of the experimental results.

It must be noted that the results shown in Figure A.3 were performed with a water of 30°C (like in all other experiments performed), while the pressure drop experiments that were performed in Danfoss were performed with a water of 50°C. To make sure that this would not effect the comparison, the original flow meter was tested at both temperature. The results showed that the temperature of the water does not effect the pressure drop in a significant way, the deviations between the two values were lower than 4% at all flow rates. The results from this temperature test can be seen in Appendix A.5.

4.2 Validation Of Flow Modeling

It is often hard to trust whether CFD results are giving the correct results or not. In order to validate if the CFD model was giving adequate results, and which of the tested turbulence models were giving the most compatible results to the experimental results. As mentioned before, three different turbulence models were tested. The comparison is presented in Figure 4.3. The experimental results presented in the graph are the un-disturbed pressure drop, that is the pressure drop after the empty pipe results were subtracted, like explained in Section 2.2.2.

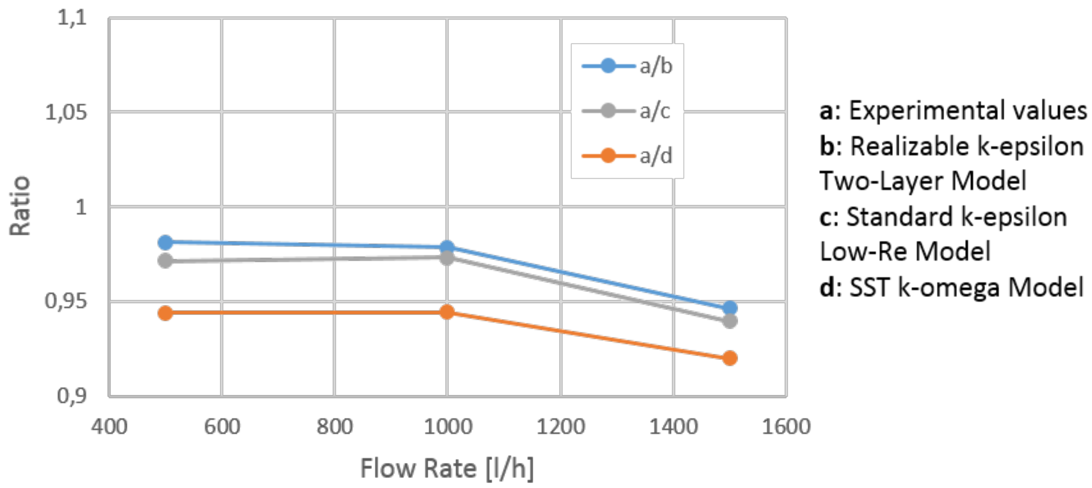

Figure 4.3: Comparison of the three turbulence models.

All the models proved to give a good representation of the experimental results for the lower flow rates. As the flow rate grows, the models start to give more variation between the two values. As can be seen, the results from the Realizable k-ε Two-Layer Models fit the experimental results in the best way and will therefore be used in further simulations. It would have been expected that the Low-Re model would have given better results than the Two-Layer model, since the Low-Re model has proven to solve the viscous sublayer in a better way than the other. The reason for the Two-Layer model giving more adequate results over the other must therefore be since it is a Realizable model and not Standard as the other, but as explained in Section 2.3.3, the Realizable model is an improved version of the Standard one.

4.2.1 Mesh Refinement

Three different mesh types were tested, to see how fine it should be in order to give as accurate results without too much computational effort. The details about the three meshes are given in Table 4.1. The volumetric control was only applied around the fixture in Mesh 3. The control was applied to the surface remesher, so the base size in that area is 30% of what it is in the rest of the flow region.

The three different mesh-types were applied with the Realizable Two-Layered $k-\varepsilon$ turbulence model for a flow with flow rates of 500, 1000 and 1500 l/h. The resulting pressure drop from the simulations is presented in Table 4.2.

The experimental pressure drop in the comparison, was as before, the un-disturbed pressure drop. As can be seen, all the meshes give a pretty good representation of the pressure drop for the lowest flow rate. As has been experienced before, and can be seen in Figure 4.3, the difference between the simulations and the experimental values grows

Table 4.1: Details about the three different meshes.

	Mesh 1	Mesh 2	Mesh 3
Base size	2 mm	1 mm	1 mm
Number of Prism Layers	7	7	10
Volumetric Control	No	No	30%
Number of Cells	130.653	352.810	1.872.483

Table 4.2: Pressure drop, ΔP, from the tree meshes.

	Mesh 1	Mesh 2	Mesh 3	Experiment
500 l/h	657 Pa	680 Pa	677 Pa	680 Pa
1000 l/h	2680 Pa	2587 Pa	2365 Pa	2570 Pa
1500 l/h	6043 Pa	5908 Pa	5873 Pa	5540 Pa

larger with increasing flow rate. At the first two flow rates, Mesh 2 is the mesh that is closest to the experimental value. However, it would be expected to get a lower pressure drop from simulations than from experiments, since there are a lot of factors that influence experimental results while simulations represent in some way a perfect world. The values from simulations using Mesh 3 are lower than the experimental values, this changes however as the flow rate in increased even more. For a flow rate of 1500 l/h, all meshes give a pressure drop significantly higher than the experiment. Mesh 3 is the mesh closest to the experimental values, they differ of 6%. Mesh 1 is the mesh that is the furthest away from the experimental results, or about 10%. The difference between the pressure drop from the meshes is not high, compared to the computational effort between them. The difference of the results from Mesh 2 and Mesh 3 is only 0.5% although the number of cells in Mesh 3 is 5 times larger than the number of cells in Mesh 2. Mesh 2 is therefore considered to be a good balance between accuracy and computational effort and will be used in further simulations. Since all geometries were quite similar, it was assumed that there would not be a need for mesh validation for the other geometries.

CHAPTER 5

Results & Discussion

Since there were many restrictions in the optimization, the options of what could be changed in the geometry to minimize pressure drop were not many. They could in general be divided into three categories, optimization of arms, optimization of the reflectors back and optimization of the inlet.

The results from both the experiments and numerical simulations are presented here, both for the original geometry of the flow meter and for a number of 15 prototypes. All flow profiles are presented for a flow rate of 1500 l/h, ideally the results would be presented for a flow rate equal to the nominal flow rate of 2500 l/h, but since the experimental test rig only reached up to around 1750 l/h, that was not possible.

5.1 The original flow meter

Before any attempts for optimization of the flow meters' geometry with regards to the pressure drop were made, the flow of the original flow meter was studied to see where the most critical points were. The results from the experiments with the original flow meter have already been discussed in the Validation chapter, therefore, only the CFD results are discussed here.

Figure 5.1 shows a horizontal slice through the center of the flow field around the geometry. From the figure, it can be obtained that there is a stagnation point a little above the center line of the flow (at location 1 on figure). Two separation points from the first reflector can also be seen, one on the top of the reflector and the other on the bottom (locations 2 and 3). Between the two separation points is a backflow (location 4) until the flow unites again and goes into the liner. As can be expected, the fluid has a higher velocity in the middle section of the fixture, since the diameter is smaller inside the liner. There is a deadwater region around the liner (location 5 and 6), where there is space between the liner and the fixture. This deadwater region goes around the liner, but since the figure is just a slice through the flow field, it is not very visible. Two eddies are visible around the second reflector. One situated where the flow expands after coming out of the liner (location 7) and the other behind the reflector (location 8). Behind the eddy on the back of the back of the reflector there are some flow disturbances where backflow occurs (location 9). Similar stagnation and separation points as are around the first reflector can also be seen around the second reflector. It must be noted that the stagnation point on the second reflector is much lower than the stagnation point on the first reflector.

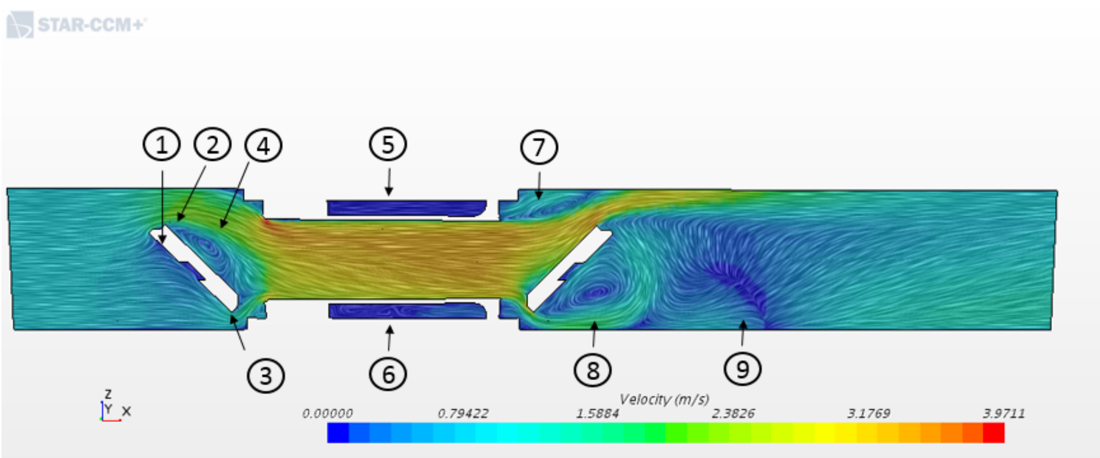

Figure 5.1: Horizontal slice through the center of the flow field of the original flow meter.

Figure 5.2 shows a vertical slice through the center of the flow field around the geometry. The vertical flow filed is symmetric, as would be expected since the flow meter fixture is symmetrical in the horizontal plane. A stagnation point can be seen in the center in front of the first reflector (location 1). There are separation points on either side of the reflector (location 2) and as could also be obtained from the horizontal flow field, there are swirling eddies on top of the first reflector. The deadwater region around the liner (location 4) can also be noticed. There are eddies on the sides of the second reflector, after the diameter expands again (location 5), as well as behind the same reflector (location 6). Finally, some backflow is obtained behind the two big eddies (location 7). This backflow is happening in the same location as the backflow obtained at location 9 in Figure 5.1 and is caused by the eddies on the back of the second reflector. From the velocity filed it can be assumed that the main pressure drop occurs at the second reflector.

Figure 5.3 shows a horizontal slice through the center of the total pressure field. The total pressure is the subtotal of the static pressure, dynamic pressure, and the gravitational head. It is the measure of the total energy of the flow, and is equal to static pressure plus velocity pressure. From the figure, it can be obtained that there is a drop in the pressure over the first reflector. Above the first reflector is a swirling eddy with low velocity (and therefore low kinetic energy), which explains the low total pressure in that place. The total pressure is high inside the liner, since the kinetic energy is high in that section. As could

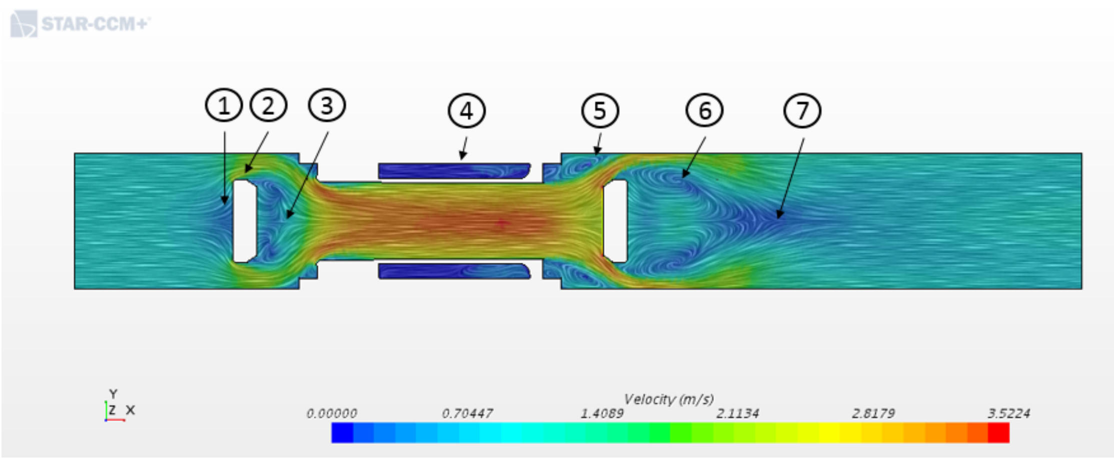

Figure 5.2: Vertical slice through the center of the flow field of the original flow meter.

be obtained from Figure 5.1, the velocity in the upper part inside the liner is higher than the velocity in the lower part, this can also be obtained from the total pressure, which is lower in the lower half. The total pressure remains high after the fluid flows out of the liner and over the second reflector. The lowest total pressure is behind the second reflector, this is due to the low velocity eddies that could be seen in the velocity flow fields.

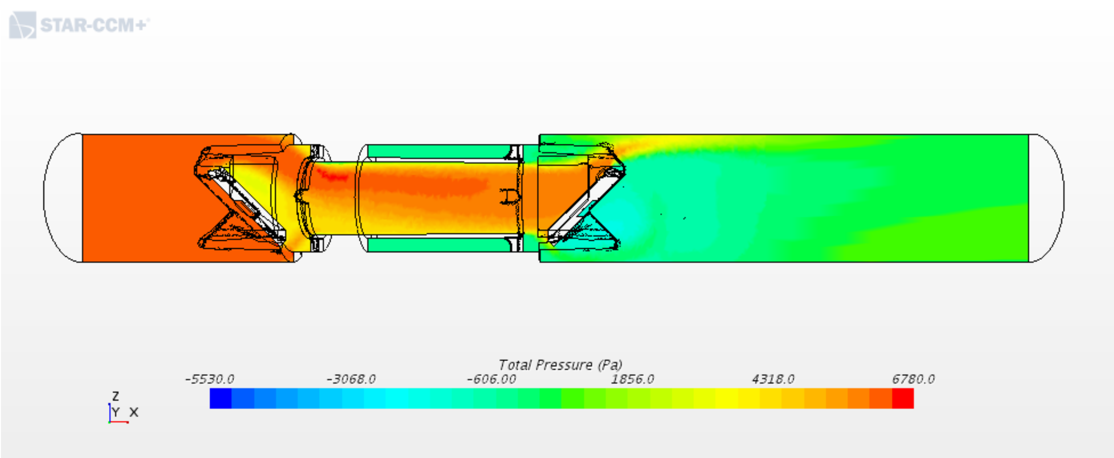

Figure 5.3: Horizontal slice through the total pressure field of the original flow meter fixture.

Figure 5.4 shows a vertical slice through the center of the total pressure field. As with the vertical velocity field, the vertical total pressure filed is also symmetric. It can be obtained that the highest total pressure inside the liner is in the center of the flow, while the total pressure is lower near the walls. This fits well to what was discussed in Section 2.2.2. All the discussed critical pressure zones that were discussed with regards to the horizontal slice through the total pressure filed also apply to the vertical one. After studying the total pressure field, the assumption about the main pressure drop occurring after the second reflector is concluded to be correct.

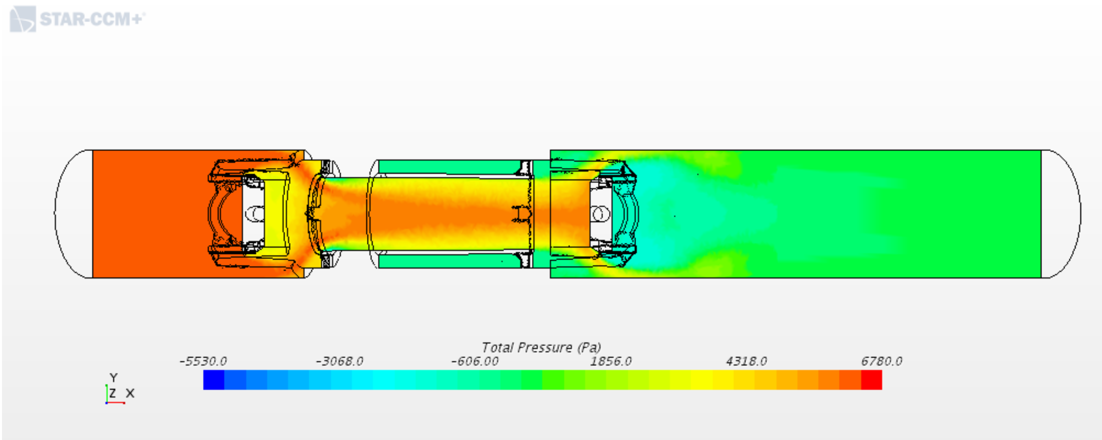

Figure 5.4: Vertical slice through the total pressure field of the original flow meter fixture.

Figures 5.5 and 5.6 show the horizontal and vertical slices through the pressure alone. A high-pressure zone behind the first reflector can be obtained from the figures. The pressure drop over the first reflector is used to accelerate the flow into the smaller diameter in the liner. It also shows how the pressure drops as the fluid gets further into the liner. The pressure then recovers in a way when the fluid moves out of the liner and drops again as it goes over the second reflector.

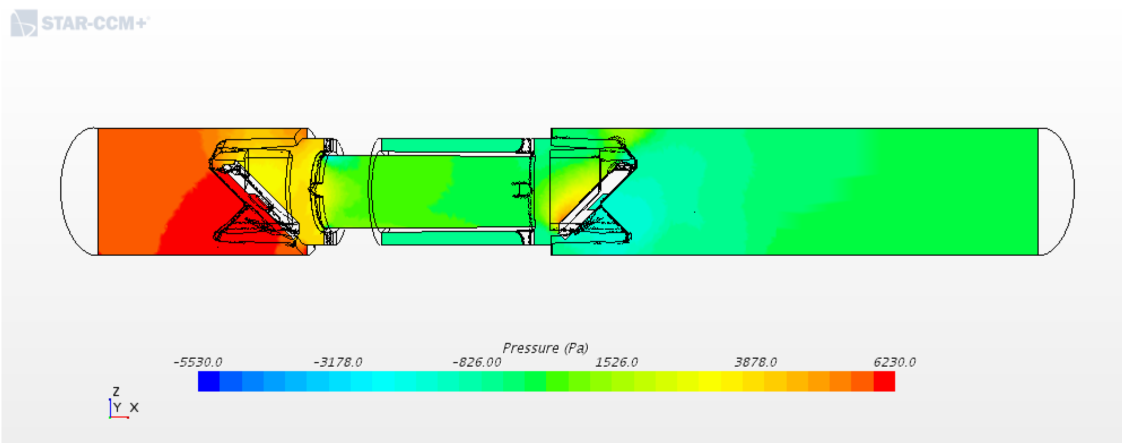

Figure 5.5: Horizontal slice through the pressure field of the original flow meter fixture.

Figures 5.1-5.6 can all be summarized up in Figure 5.7. The graphs in the figure are obtained by taking a line through the center of the flow field. In this way, it is easier to compare the results of different prototypes. From the total pressure graph, it can be concluded that the most critical point that is causing the pressure drop is the second reflector. Due to the constraints presented in Section 1.2 no changes can be made there.

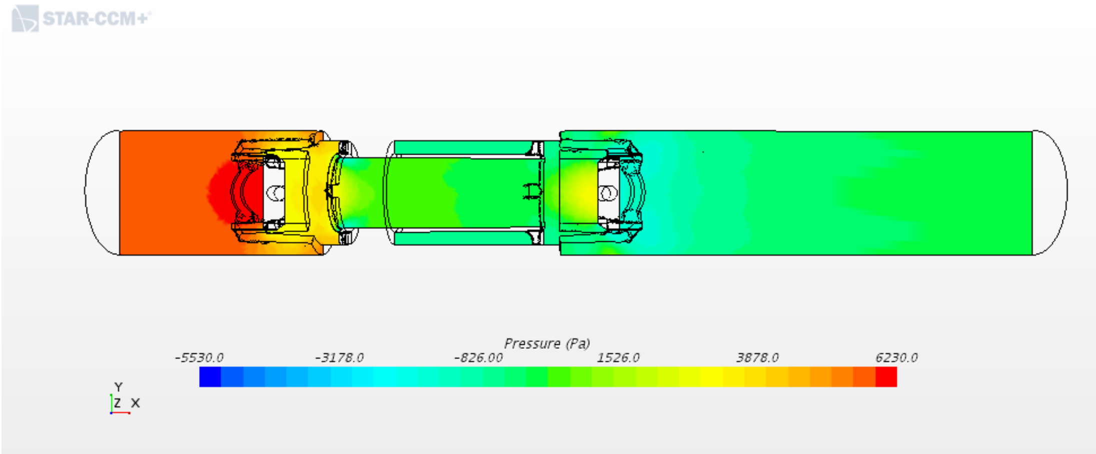

Figure 5.6: Vertical slice through the pressure field of the original flow meter fixture.

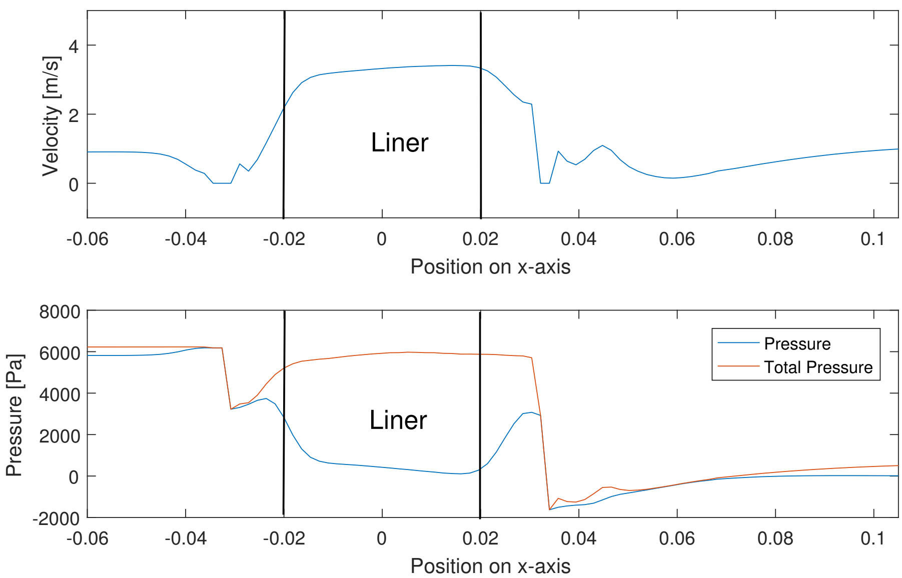

Figure 5.7: Above: The velocity through the center of the flow field with the original fixture. Below: The pressure and total pressure through the center of the flow field with the original fixture.

5.1.1 3D Printers

In order to see if there would be a significant difference between the three printers and printing materials, the original flow meter was printed with all three printers and results were compared. The results from this can be seen in Figure 5.8. The results are compared by using the pressure loss coefficient, K, that was introduced in Section 2.2.2. The pressure drop coefficient gives a good representation between flow rate and pressure drop, but pressure drop inside a pipe has been proven to be proportional to the square of the flow rate. In a perfect flow, the pressure drop coefficient would be stable, but as can be seen in the figure, the coefficient decreases as the flow rate increases. This could be explained by that the flow has not yet reached stability, the pressure loss coefficient seems to be reaching a stable state in the highest flow rates in the figure. As can also be seen, the uncertainty of the pressure loss coefficient is high for the lower flow rates, compared to the higher ones, this could be one of the reasons for the unstable values.

It is obvious from Figure 5.8 that the quality of the 3D print does make a difference. The worst quality print, the one from Ultimaker 2+, gives the lowest pressure drop, this could both be due to insufficient details in the print or due to that the material is not as strong as the others. The results from the Afinia H800 printer were the ones that resembled the original manufactured one in the best. It would have been the most preferable to use that printer for all other experiments, but as was stated before, the Afinia H800 printer was very unreliable and could therefore not be used. The results from FormLabs 2 lay in between the Ultimaker 2+ and the Afinia H800 results. This curve is more stable than the others. This could be because of the material that is used for this printer is the softest out of all of them although the quality of the print is the best. This printer was only used to print this one print due to how expensive it is to use.

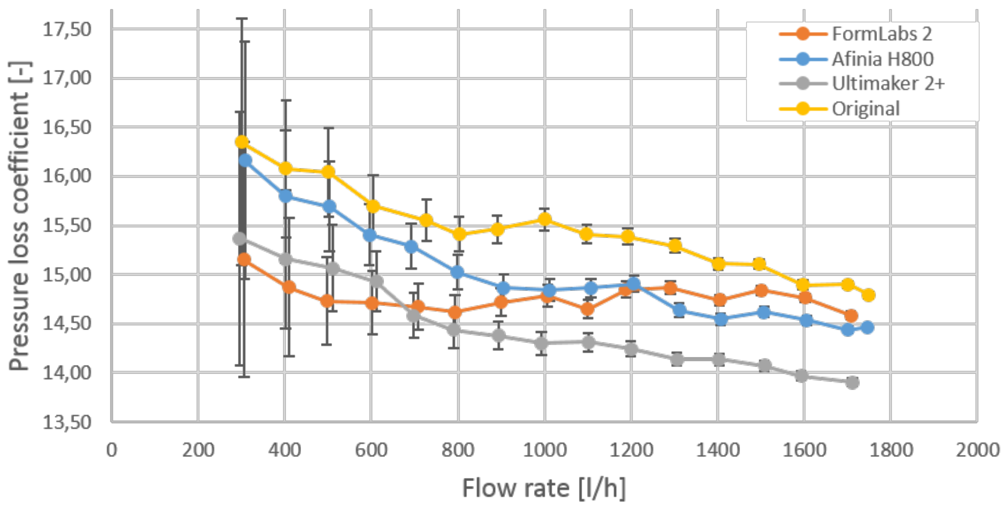

Figure 5.8: Experimental results from the original geometry printed with different 3D printers.

From this it can be concluded that the quality of the 3D print does effect the experimental results. In the upcoming sections, all experimental results are gotten by using 3D prints from the Ultimaker 2+. The results are then compared to the results of the original geometry that was printed with the same printer in order to give the best and most accurate perspective on the results.

5.2 Optimizations

As described in Section 3.1, the optimization process was carried out in an iterative process. The original geometry was at first only evaluated by eye. When looking at the original geometry, one might wonder the purpose of the large arms holding the lower part of the reflector. This was the initial idea in the process, to change the arms on the lower half. The idea then evolved from the lower arms to the upper arms, but after evaluating the ideas, only one modification on the upper arms was tested, apart from taking them away altogether. After performing CFD simulations on the original geometry, an idea to change the inlet and outlet from the liner was come up with. This was though as to try to eliminate the eddies that can be seen at location 7 in Figure 5.1 and location 5 in Figure 5.2, and lead the flow in a better way in and out of the liner. Furthermore, after seeing that the critical pressure drop occurs at the back of the second reflector, the idea of adding a shape on the back of the reflector was come up with. Finally, it was investigated how mixing the prototypes together would work out. This is all discussed in more details in the following subsections.

5.2.1 Adaptions of Arms

The adaption of arms is the change that offers the most possibilities. The most obvious change to make to the geometry would be to remove the arms and add one thick arm in the bottom part. Prototype I is a version of this, where all arms were removed and replaced with an 8 mm wide arm. Figure 5.9 gives a better representation of the geometry of Prototype I.

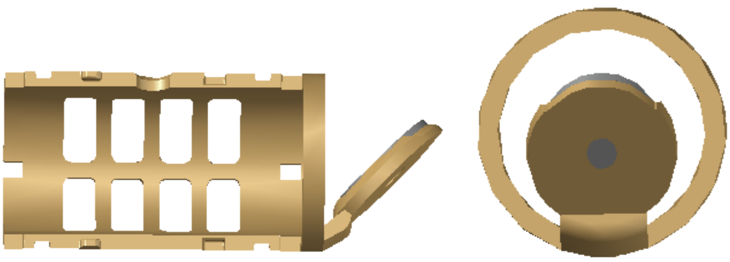

(a) Side view (b) Front view

Figure 5.9: Prototype I.

The next prototype, Prototype II, was made with the same idea in mind as Prototype I. The difference between them was that for Prototype II, the arm was wider and went straight down from the sides of the reflector, so it had the same width as the reflector. Prototype II is shown in Figure 5.10.

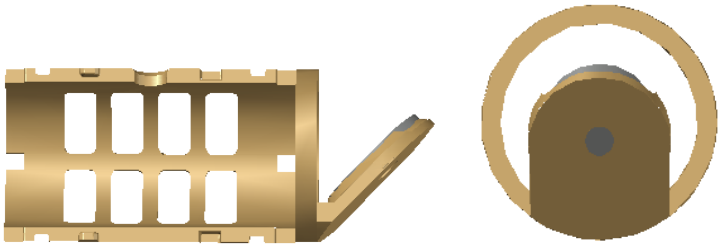

(a) Side view (b) Front view

Figure 5.10: Prototype II.

In the third prototype, Prototype III, the upper arms were kept in the same way as the original, but instead of the two lower arms, there was one in the middle that had the same width as the other arms. This version can be seen in Figure 5.11.

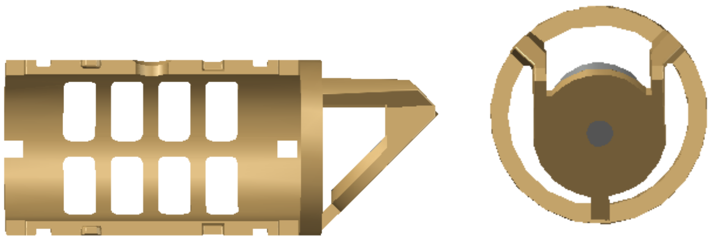

(a) Side view (b) Front view

Figure 5.11: Prototype III.

Prototype IV is basically the same as Prototype III, but the lower arm was made longer and with an angle. In that way, there was less shock created when the fluid particle hit the arm since the surface that was perpendicular to the flow was smaller. Prototype IV is shown in Figure 5.12.

(a) Side view (b) Front view

Figure 5.12: Prototype IV.

The last two prototypes in this section are with the same basic idea, to make the arms have an elliptical surface, in that way the arms were smaller than before. Prototype V features this on the upper arms and Prototype VI features it on the lower arms. This can be seen in Figures 5.14 and 5.13.

(a) Side view (b) Front view

Figure 5.13: Prototype V.

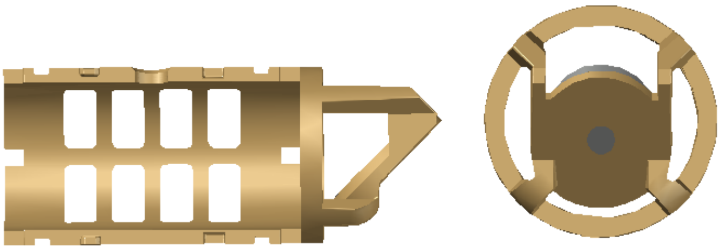

(a) Side view (b) Front view

Figure 5.14: Prototype VI.

The experimental results from these two prototypes are presented in Figure 5.15, where the resulting pressure coefficients were plotted up against the flow rate. As can be seen, all the prototypes had lower pressure coefficients than the original geometry. Prototype I resulted in the lowest pressure drop. Prototype II, that is very similar to Prototype I, however results in much higher pressure drop than Prototype I. Due to this, the flow through Prototype II was not simulated. As before, it can also be obtained that the pressure coefficients decrease with increasing flow rate. It could be that they have not yet reached stability. This means that the definition of the pressure coefficient is not a perfect model. However, since the variation is so modest, it is still relevant to use.

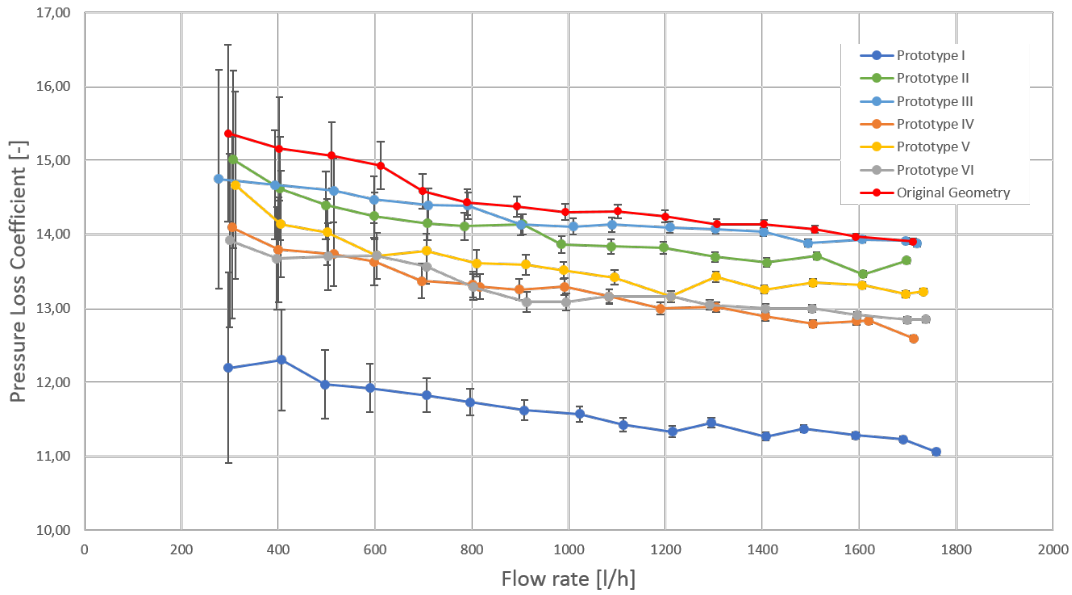

Figure 5.15: Experimental results from prototypes where changes were made to the arms of the fixture geometry.

The simulated flow profiles are all quite similar to the one of the original geometry that can be seen in Figures 5.1 and 5.2. Of course there are some changes but not in any significant way, therefore the flow profiles were compared by taking a line through the center of the flow, like was demonstrated in Figure 3.9. In that way, a better comparison can be made. The flow profiles themselves can be found in Appendix B. Figure 5.16 shows the velocity, the pressure and total pressure field of the prototypes compared to the original geometry. It is clear that the velocity inside the liner is the same for all prototypes and the original geometry, this is an indication of that the results are compatible since nothing was changed about the liner so the velocity inside it should be consistent. Some deviations can be noticed in the velocity, after the flow goes over both the first and second reflector. By looking at the total pressure, it can be noticed that not much changes in the main pressure loss behind the second reflector. The deviation is more in the first pressure drop, which makes sense since the arms holding the reflector have more impact on the flow there. The pressure drop of some prototypes seems to be higher than the pressure drop of the original geometry, this is however not the case when surface average is used. The change in pressure drop is therefore probably more drastic in other locations than the center. It may be assumed that these locations change with each prototype and therefore the center would be the most appropriate place to compare all the geometries together.

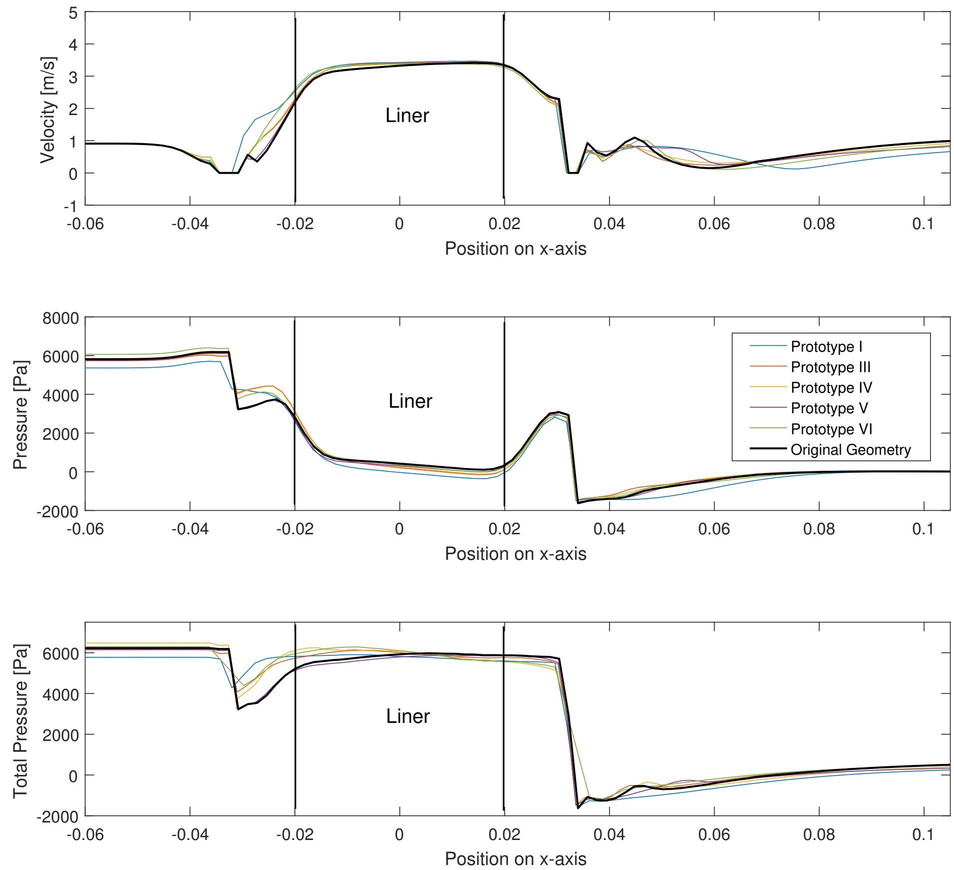

Figure 5.16: The velocity, pressure and total pressure through the center of the flow field of fixtures with changed arms. The legend is valid for all the figures.

The CFD model was run for three different flow rates for all prototypes, 500 l/h, 1000 l/h and 1500 l/h. Figure 5.17 shows the comparison of the experimental results and the CFD simulation results. The experimental results have been treated in such a way as was explained in Section 2.2.2, where the pressure drop through an empty pipe is subtracted from the results in order to get a better assumption of what should be expected from the CFD results. As can be seen the pressure drop is proportional to the square of the flow rate, which was expected according to the concept of the pressure loss factor. The CFD results all seem to follow the same curve as the experimental results, but are in general higher. The deviation between the two results are between 3-14% and it gets larger as the flow rate increases. It would be expected to get results from the CFD simulations that were lower than the experimental results but that is not the case here, some explanations for that might for example be the simplifications that were made to the geography, the mesh and other. The deviation can also be due to the method used to calculate the pressure drop. In the experiments a piezometer was used, but such a device measures the pressure in a point, while in the CFD simulations, the pressure was measured over a surface area.

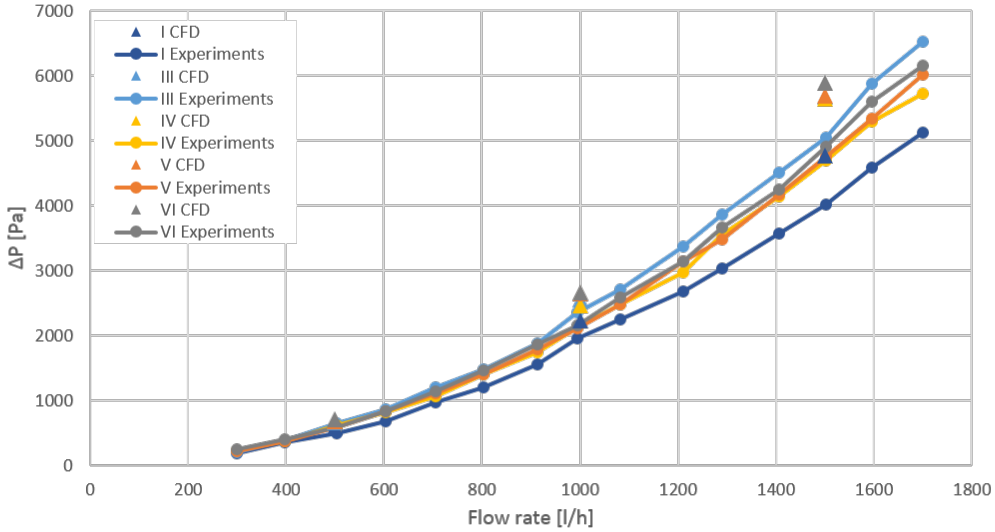

Figure 5.17: Comparison of experimental and CFD results.

5.2.2 Adaptions of Inlet

The inlet of the flow meter fixture has a sharp edge, and if looked at Figure 3.6, it can be seen that the flow is not lead in any way into the liner, which has a smaller diameter than the fixture. The changes made to the inlet of the fixture were made with it in mind to lead the fluid in a better and smoother way into the small diameter of the liner.

In the first attempt, Prototype VII, the fixtures body was made 6 mm longer and made to have an angle, so no part of it would be parallel to the flow. This is shown in Figure 5.18.

The second attempt, Prototype VII, has a diffuser-like inlet to the liner. This was thought of to eliminate the deadwater region in the corners outlet of the liner, seen in location 7 in Figure 5.1 and location 5 in Figure 5.2. This prototype is shown in Figure 5.19.

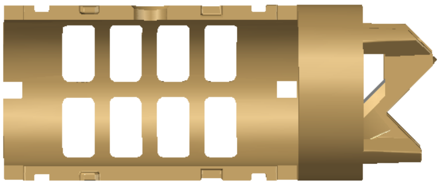

(a) Side view

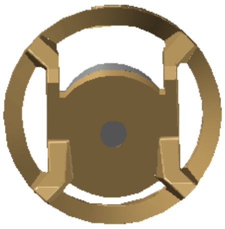

(b) Front view

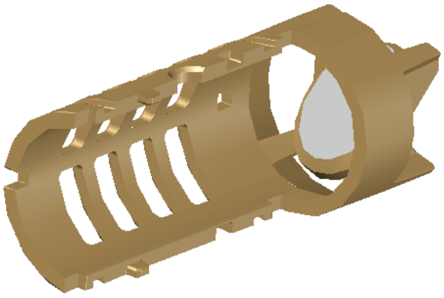

(c) Perspective view

Figure 5.18: Prototype VII.

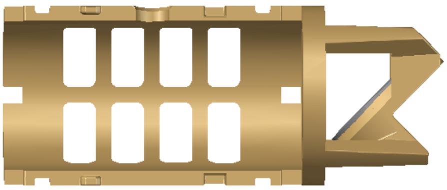

(a) Side view

(b) Front view

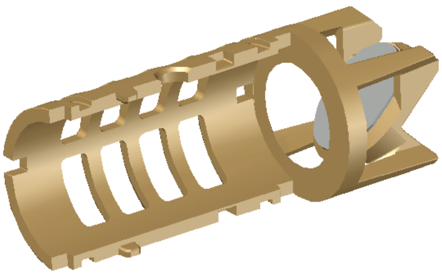

(c) Perspective view

Figure 5.19: Prototype VIII.

The experimental results from these two prototypes are presented in Figure 5.20, where the resulting pressure coefficients were plotted up against the flow rate. As can be seen, the diffuser-like inlet in Prototype VIII gives a slight improvement in the pressure drop coefficient. On the other hand, Prototype VII gives worse results than the Original geometry and will therefore not be discussed further.

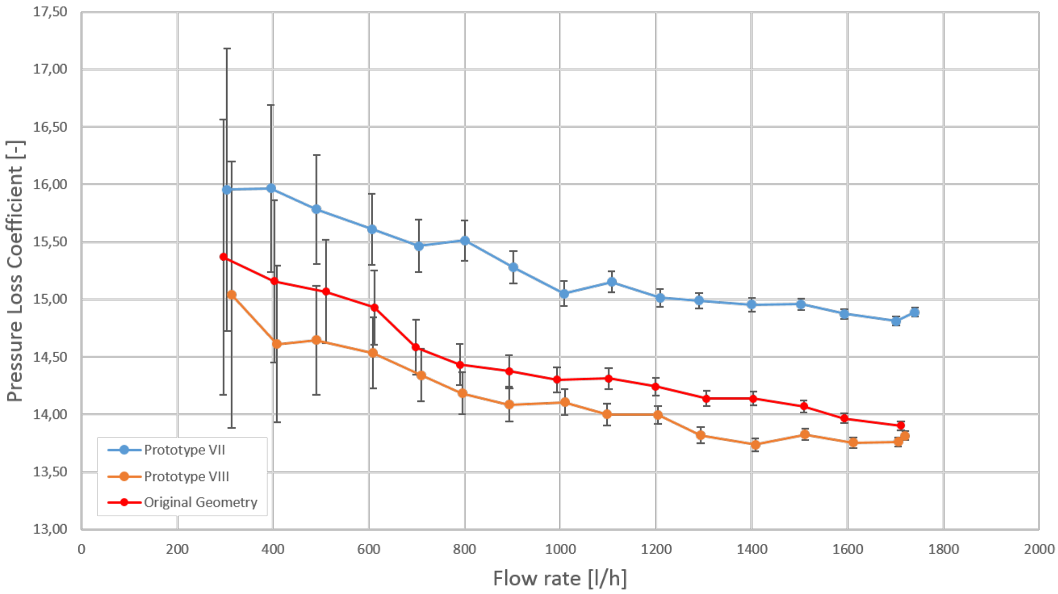

Figure 5.20: Experimental results from prototypes where changes were made to the inlet of the fixture geometry.

The flow profiles are similar to the one of the original geometry that can be seen in Figures 5.1 and 5.2. The horizontal velocity field of Prototype VIII can be seen in Figure 5.21. Like before, there are some changes but not any significant. The most noticeable difference is the disappearance of the deadwater region around the liner. The rest of the flow profiles can be found in Appendix B.

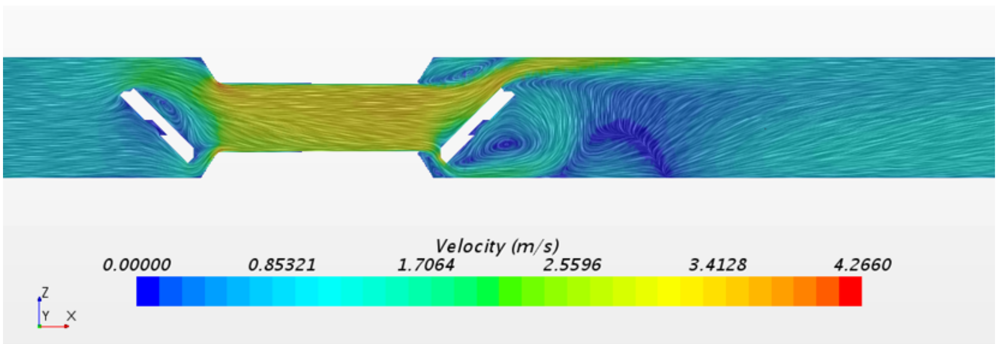

Figure 5.21: The horizontal velocity field of Prototype VIII.

Figure 5.22 shows the velocity, pressure and total pressure field of the prototypes with adapted inlets compared to the original geometry, through a line in the center of the flow field. All the curves follow the same path as for both geometry, the only significant difference is in the velocity curve after the second geometry and consequently there is also a small change in the same place in the total pressure curve.

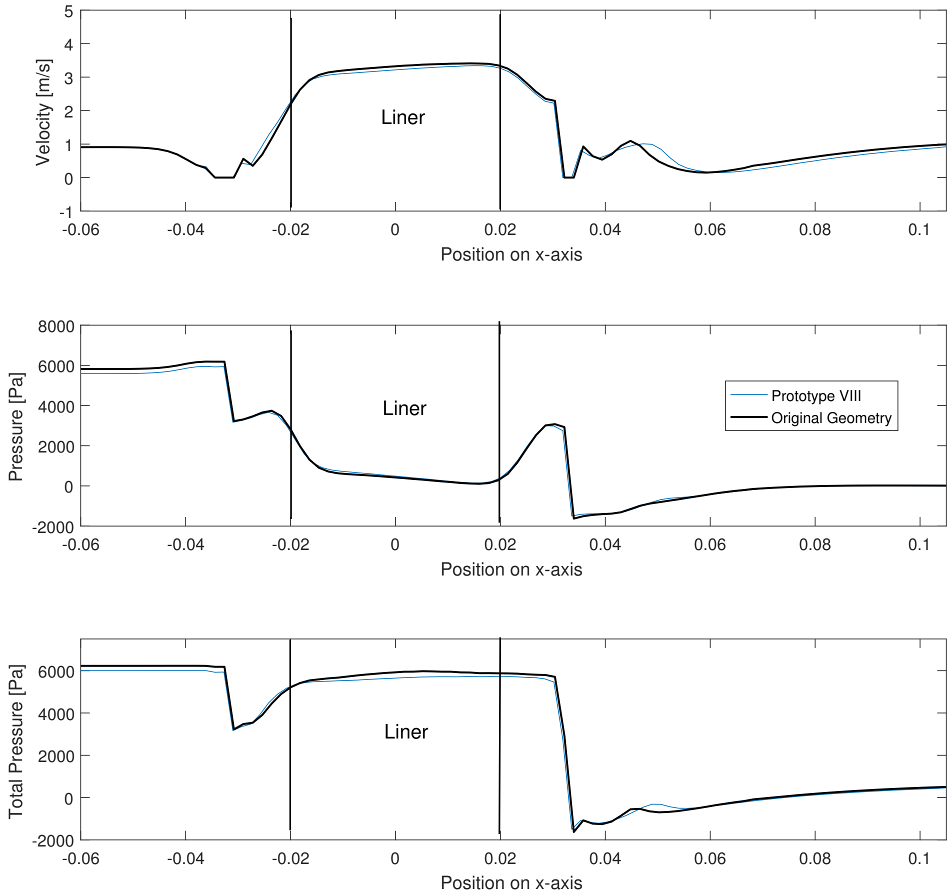

Figure 5.22: The velocity, pressure and total pressure through the center of the flow field of fixture with changed inlet. The legend is valid for all the figures.

Although the paths in Figure 5.22 are so similar in the center of the flow field, this might not be the case at other locations in the flow. An example of this can be seen in Figure 5.23, where the line through the flow field was moved 9 mm below the center. The figure therefore represents a location that goes through the lower part of the reflectors and not inside the liner, but in the deadwater zone in between the liner and the fixture. More detailed location can be seen in Appendix A.4. By implementing the changes of Prototype VIII, this dedwater zone has however been eliminated, this can be seen on the flow fields in Appendix B. It can be noticed that the total pressure and the pressure follow the same curve inside the deadwater region for both geometries, this is an indication of low velocity, or no flow as in the case of Prototype VIII, at this location. As can be seen in the figure there are more differences between Prototype VIII and the original geometry in this location than the center of the flow field. The velocity peaks higher for Prototype VIII than for the original geometry, where the flow goes under the reflectors.

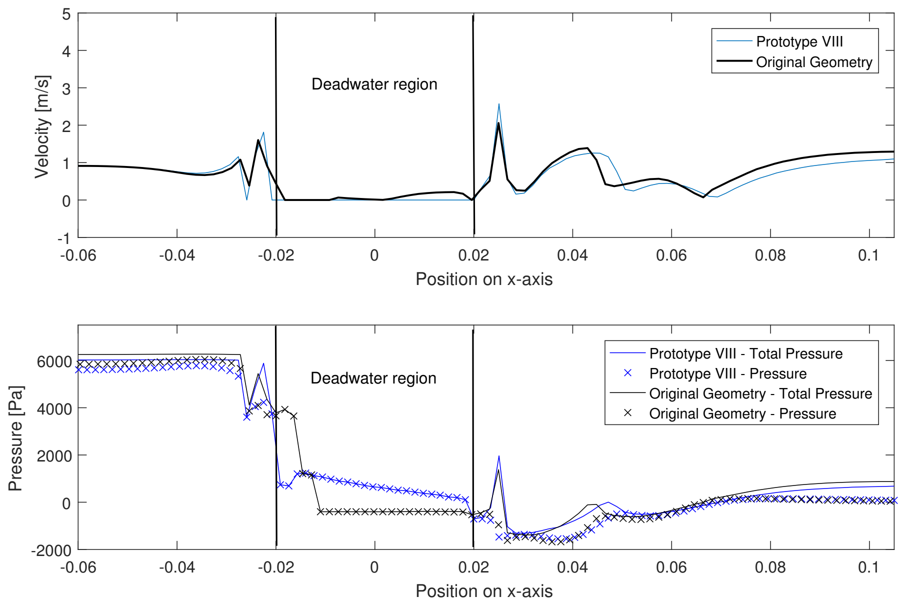

Figure 5.23: The velocity and total pressure through a line 9 mm below the center in the flow field of fixture with changed inlet.

The CFD model was run for three different flow rates, 500 l/h, 1000 l/h and 1500 l/h. Figure 5.24 shows the comparison of the experimental results and the CFD simulation results. The experimental results have been treated in the same way as before to get the pressure drop only from to the flow meter fixture. The CFD results seem to follow the same curve as the experimental results, but are in general higher, which is the same as has been experienced with previously discussed results. The deviation between the two results are between 8-12% and it gets larger as the flow rate increases.

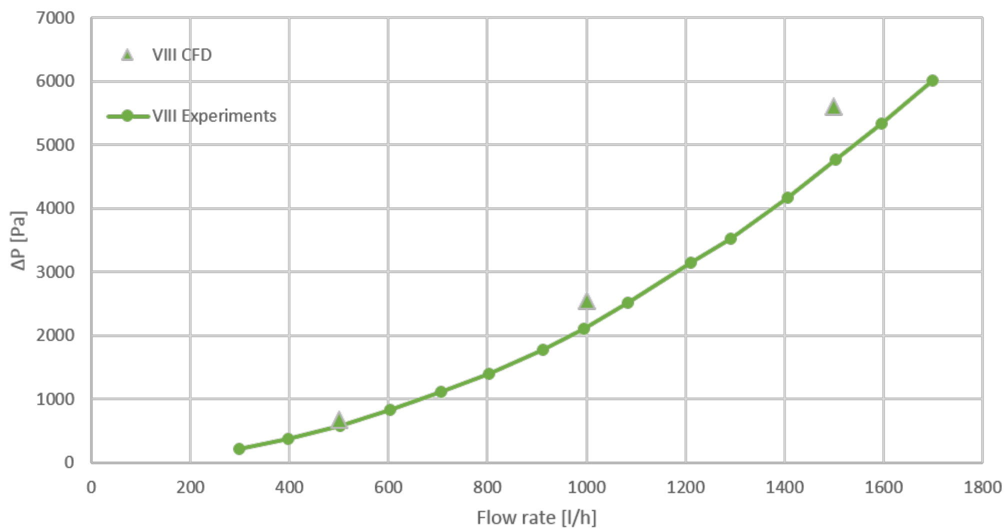

Figure 5.24: Comparison of experimental and CFD results.

5.2.3 Adaptions of Reflectors Back

The reflectors are the largest continuing surface that the flow hits, and as could be obtained in Figure 5.5, the critical parts that lead to the pressure drop. Since the reflectors could not be made smaller, nor have another orientation and further most, they could not be removed all together, the only viable option was to give the back of them a shape that is more streamlined than the flat plate of the original fixture.

In the first attempt, Prototype IX, an ellipse was put on the back of the reflector in order to make the reflector in a shape like a bullet, which has been proven to have a very streamlined body. This can be seen in Figure 5.25.

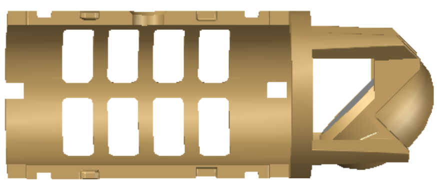

(a) Side view

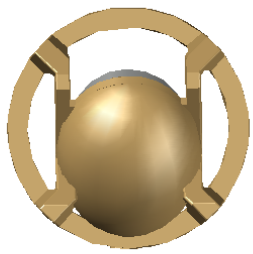

(b) Front view

Figure 5.25: Prototype IX.

In the second attempt, Prototype X, the ellipse was made to have a flat center. This can be seen in Figure 5.26. A third attempt, Prototype XI, was also made where the ellipse with the flat center was made slightly longer than the one of Prototype X. This version is not demonstrated visually since it is very much alike the previous one.

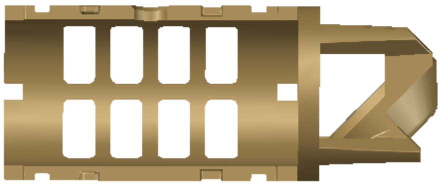

(a) Side view

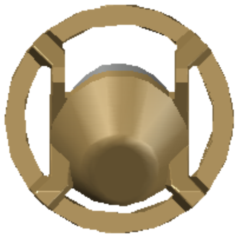

(b) Front view

Figure 5.26: Prototype X.

The fourth and final prototype, Prototype XII, was made with a cone on its back. In this way, the stagnation point of the fixture would be in the center of the flow, or on the end of the cone and not on the upper half like for the original geometry and was seen on Figure 5.1. This is demonstrated in Figure 5.27.

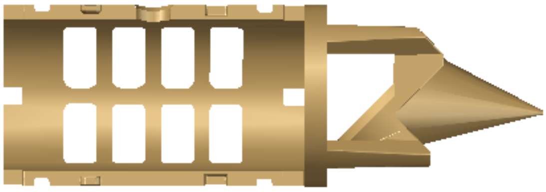

(a) Side view

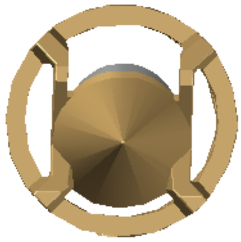

(b) Front view

Figure 5.27: Prototype XII.

The experimental results of these four prototypes are presented in Figure 5.28, where the resulting pressure coefficients were plotted up against the flow rate. As can be seen, the smaller elliptical back, or Prototype X, and the one with the cone shape back, Prototype XII, result in the near identical pressure drop. Those prototypes also have the lowest pressure drop out of the four prototypes. Prototype XI gives a significantly higher pressure drop then Prototype X, although the only difference is that the ellipse is longer. It can therefore be concluded that there is a fine line between how large the shape on the reflectors can be, for it to give the best possible results. If it is too big, it can affect the flow that goes under the reflector in such a way that it causes larger drop in pressure then it would do if the shape were smaller. The bullet shape, Prototype IX, gave even higher results then the larger ellipse shape. Because of the similarity of Prototype X and Prototype XI, only Prototype X was simulated in STAR-CCM+ since it gave better results in the experiments.

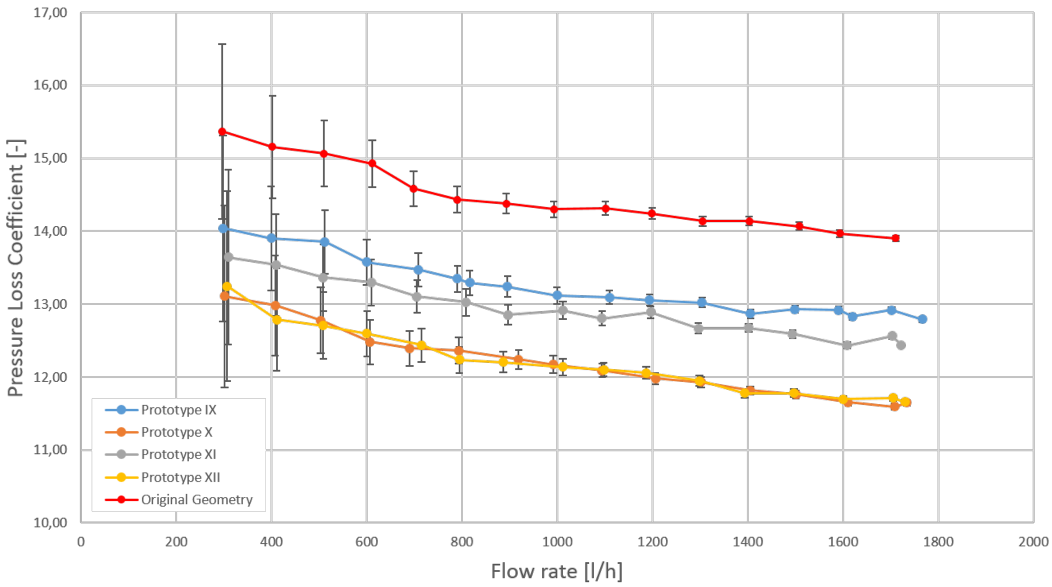

Figure 5.28: Experimental results from prototypes where changes were made to the reflectors on the fixture geometry.

Figure 5.29 features the horizontal velocity fields of the three simulated prototypes. As can be obtained from the figures, the main difference between the prototypes is the stagnation point on the first reflector and the flow behind the second reflector. The flow in front of the reflector is the smoothest for Prototype XII, while the flow behind the second reflector for the same prototype experiences a lot of backflow. The rest of the simulated flow profiles can be found in Appendix B.

Figure 5.30, shows in the same way as before, a comparison of the prototypes by taking a line through the center of the flow field. It can be observed from the total pressure field that the pressure drop from the second reflector is significantly lower when the back of the reflectors is modified. This is because the eddy formed in that locations changes.

The CFD model was run for three different flow rates, 500 l/h, 1000 l/h and 1500 l/h. Figure 5.17 shows the comparison of the experimental results and the CFD simulation results. The experimental results have been treated in the same way as before. The CFD results seem to follow the same curve as the experimental results, but they are in general higher, which is the same as has been experienced with previously discussed results. The deviation between the two results are between 8-16% and it gets larger as the flow rate increases.

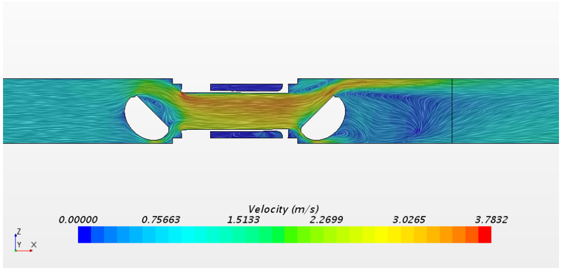

(a) Prototype IX

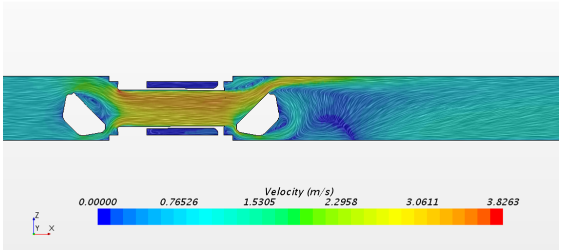

(b) Prototype X

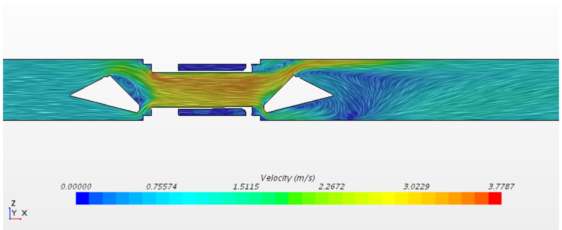

(c) Prototype XII

Figure 5.29: Horizontal velocity fields of prototypes with adapted reflectors back.

5.3 Mixing Prototypes Together

Finally, some attempts were made with mixing the prototypes together to see how they would work together. Figure 5.32 shows the three versions that are discussed here, since most of the attempts gave similar results it is not necessary to mention all of them.

The first one, Prototype A, was a mixture of Prototypes IV and IX, so it had a bullet shape on the back of the reflector and one long lower arm. The second one, Prototype B, was a mixture of Prototypes IV, VIII and IX, so it had a rounded inlet, bullet shape on the back of the reflector and one long lower arm. And the third one was a mixture of Prototypes IV, V and VIII, so it had a rounded inlet, ellipse shaped upper arms and one long lower arm.

Figure 5.33 shows how these three versions behaved in the experiments. As can be seen, they do not show any more improvement then the prototypes discussed in the previous sections and even in the case of Prototype B, the pressure drop coefficient is higher than the one of the original geometry.

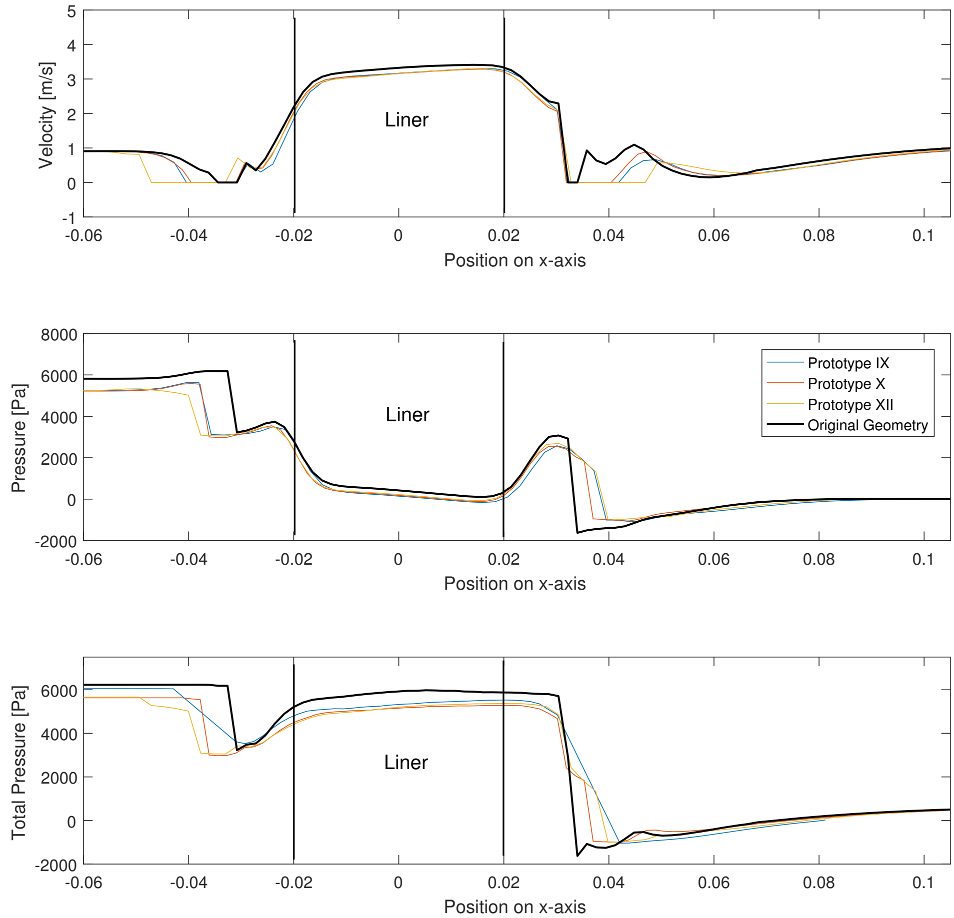

Figure 5.30: The velocity, pressure and total pressure through the center of the flow field of fixtures with changed reflectors. The legend is valid for all the figures.

These versions were not simulated in Star-CCM+, since they did not show any improvements regarding the pressure drop compared to the prototypes that were discussed previously.

5.4 Summary of the Results

To get a better overview of all the prototypes tested and their performance, their pressure loss coefficient can be compared. As could be obtained from the pressure loss coefficient graphs, the coefficient is not constant as it should be, but it is assumed that it will get constant with increasing flow rate and has not yet reached stability in the end of the experimental range. The pressure loss coefficients are therefore compared at a flow rate of 1500 l/h, this can be seen in Table 5.1.

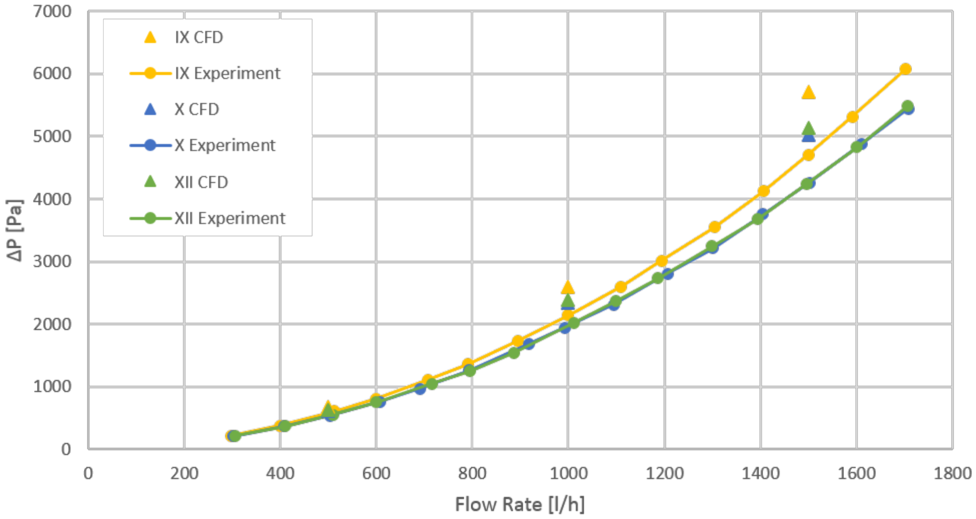

Figure 5.31: Comparison of experimental and CFD results.

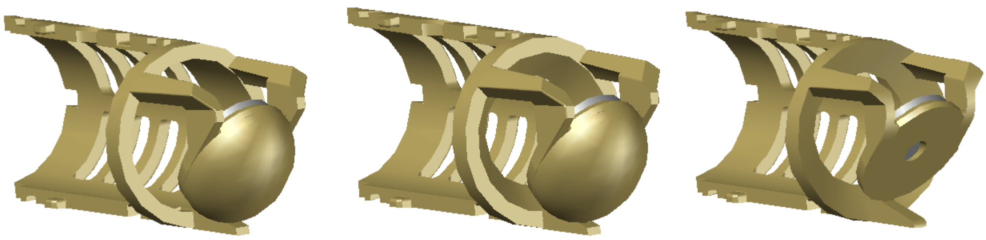

Figure 5.32: Prototype A to the left, Prototype B in the middle and Prototype C to the right.

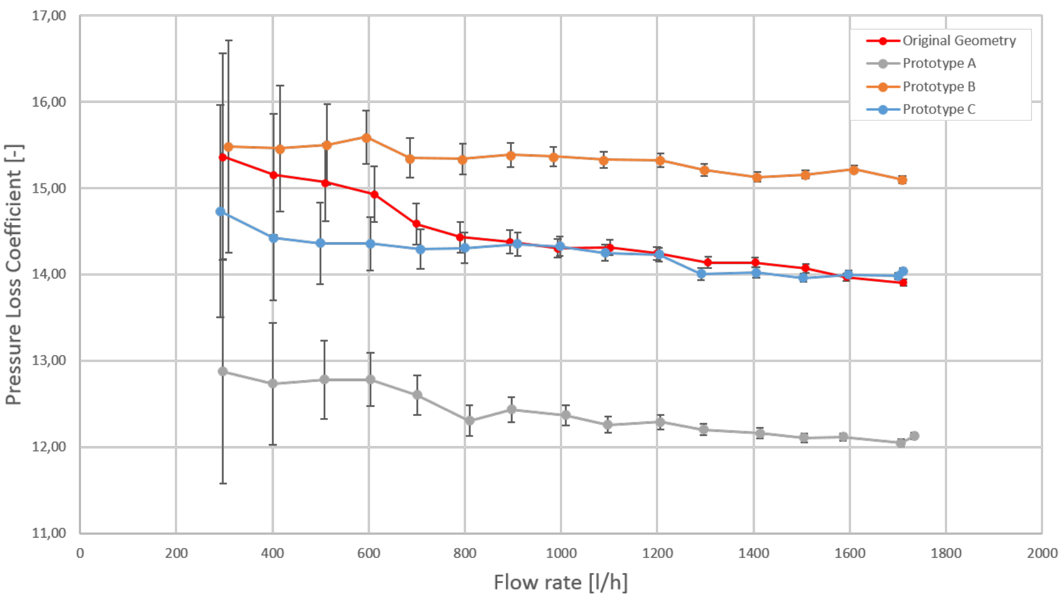

Figure 5.33: Experimental results from the mixed prototypes.

Table 5.1: Summary of the results from experiments with flow rate of 1500 l/h.

	Description	**K**	**% from Original**
Original	The original geometry	14.07±0.05	
Prototype I	One large foot in lower half	11.37±0.05	19%
Prototype II	One large foot in lower half	13.71±0.05	3%
Prototype III	One small foot in lower half	13.88±0.05	1%
Prototype IV	One small foot in lower half	12.57±0.05	11%
Prototype V	Arms in upper half with elliptical shape	13.00±0.05	8%
Prototype VI	Arms in lower half with elliptical shape	13.35±0.05	5%
Prototype VII	Elongated inlet	14.96±0.05	-6%
Prototype VII	Diffuser-like inlet	13.83±0.05	2%
Prototype IX	Bullet shape on back of reflector	12.76±0.05	9%
Prototype X	Ellipse shape on back of reflector	11.76±0.05	16%
Prototype XI	Ellipse shape on back of reflector	12.59±0.05	11%
Prototype XII	Cone shape on back of reflector	11.78±0.05	16%
Prototype A	IV+IX	12.11±0.05	14%
Prototype B	IV+VII+IX	15.16±0.05	-8%
Prototype C	IV+V+VII	13.96±0.05	1%

As can be seen in the table, the changes made on the back of the reflector generally has a quite high impact on the pressure drop. The changes made on the arms also show some improvements, both small and big. The changes of the inlet of the fixture prove to not make as much as an impact on the pressure drop.

The prototype that gave the best results, or about 19% from the original geometry, was Prototype I with no arms on the upper half and one large arm on the lower half. Although this gave the lowest pressure drop, this might not be the optimal design since it is more fragile than the rest of the prototypes and could therefore perhaps not meet all the standards the geometry has to meet with regards to durability or maximum flow rate for example. This has however not been looked further into. Adding a shape on the back of the reflectors might also not be the most optimal solution with regards to manufacturing of the fixture.

This was also not investigated further.

Prototype A is an improvement from the two prototypes it was combined from, but the other two combinations did not result in improvements. What can be concluded from this is that by combining improving factors together does not necessary end up in improvements, but these factors can have the opposite effect on each other. However, there are endless possibilities in regards to combinations of what can be done to improve the pressure drop and not all combinations out of the 12 prototypes were tested.

CHAPTER 6

Conclusion

In this thesis, it was studied how the geometry of an ultrasonic flow meter could be optimized with regards to pressure drop. The work was carried out both using experiments and CFD simulations in the commercial CFD software, STAR-CCM+.

The experimental work was carried out for a number of prototypes as well as for the original geometry. Rapid Prototyping was used to produce the prototypes. A validation study was performed that concluded in confirmation of that the prototypes were compatible to the original flow meter that is produced now. It was obtained that the pressure drop was proportional to the square of the flow rate, like was to be expected according to Bernoulli's principle. A study was made that compared the experimental results between three different 3D printers. From that it was concluded that the quality of the 3D printer did have an impact on the results, it was obtained that the lower the quality, the lower the pressure drop.

The flow through the flow meter was modelled through steady state calculations for both the original geometry and 8 of the prototypes. The flow profile of the original geometry was studied and the critical points that lead to the pressure drop were pinpointed. The flow profiles of each prototype were compared through a line where, they all showed some improvements compared to the original geometry. The simulations showed a good representation of the experimental results although they were in general slightly higher, or from 4-14%. The reasons which might cause inconsistency between the CFD results and the experimental results, are multiple and are listed below:

- The simplifications that were made to the geometry imported into the CFD software.
- The mesh used in the CFD simulations.
- The low quality of the 3D printer which resulted in a lower experimental pressure drop.
- The flow through the flow meter in the experimental test-rig might be influenced by

the close proximity to the U-bend, so the flow might not be fully developed when it went through the flow meter and the pressure drop is measured.

- The pressure drop in the CFD simulation was gotten by taking a surface average but the pressure meter used in the experiments used another approach which might cause slightly different results.
- There was a change in the diameter of the pipe, where the pipe inner diameter was 20 mm, but the inner diameter of the spool piece was 24.4 mm. This was neglected in the CFD simulations.

The results obtained in this study shows that CFD modelling in terms of fluid flow has proven to be a realistic and functional tool to simulate the flow through a flow meter. Both the Rapid Prototyping and the numerical simulations are very time consuming in its own way. Rapid Prototyping consists of long time spent 3D printing the prototypes as well as performing experiments with the highest accuracy. The prototypes are very fragile and tend to brake easily, which leads to many repetitions of the same thing. In CFD the most time-consuming part is in the first place to construct the mesh in an accurate enough way, and secondly to run the simulations. In the long run, when the correct mesh has been found and the simulations have been set up in the best representing way, CFD simulations are more time efficient then rapid prototyping, which always follows the same procedure cycle and thereby the same time-curve. In future work CFD-modelling can be used to simulate the flow inside a flow meter in a quite accurate way, while it is also a great tool in order to visualize the flow inside the meter in a better way.

6.1 Future Work

For future work, one could think more about the flow near the second mirror as that is the critical location in the pressure drop. This is however difficult due to all the constraints regarding the reflectors. One could also investigate how different geometries affect the flow measurement results by testing them with real reflectors inside working flow meters. It could be interesting to see if the results change with regards to these adjustments.

It would also be interesting to explore implementations on other sizes of the flow meter, for example one designed for lower nominal flow rate. According to the pressure loss graph published by Danfoss (Figure 4.1), the pressure drop grows for flow meters designed for lower nominal flow rates. This indicates that changes in the geometry of the fixture would make a more significant difference.

Bibliography

[1] Sonoselect. `http://heating.danfoss.com/new-solutions/sonoselect/`. Accessed: 2017-05-13.

[2] *Flow of fluid through valves, fittings and pipe. Technical Paper No. 410 M*. Crane, 1982.

[3] H. B. Bingham, P. S. Larsen, and A. V. Barker. *Computational Fluid Dynamics*. DTU, 2010.

[4] J. V. Crivello and E. Reichmanis. Photopolymer materials and processes for advanced technologies. *Chemistry of Materials Chem. Mater.*, 2014.

[5] Danfoss A/S. *SonoSelect 10 and SonoSafe 10 energy meters*, 09 2016.

[6] Danfoss A/S. *TF1096 - Danfoss Energymeter Technical Specification*, 02 2017.

[7] Duco. *Safety Valves DN15*.

[8] Flamco. *28020 - Flamcovent air separator 3/4*, 2017.

[9] Grundfos A/S. *ALPHA2 L - Circulator pumps*, 2017.

[10] A. K. Kamrani and E. A. Nasr. *Rapid Prototyping - Theory and Practice*. Springer, 2005.

[11] Kierulff A/S. *Suprex Trykekspansion Type N & E - Til varme- og køleanlæg*, 2012.

[12] H. Kudela. Turbulent flow. 2016.

[13] P. K. Kundu, I. M. Cohen, and D. R. Dowling. *Fluid Mechanics*. Elsevier, 5th edition, 2012.

[14] L. Lynnworth and Y. Liu. Ultrasonic flowmeters: Half-century progress report, 1955-2005. *Ultrasonics*, 2006.

[15] K. E. Mayer. Error analysis, lecture notes from experimental fluid mechanics, 41822. 04 2017.

[16] W. Merzkirch, K. Gersten, F. peters, V. V. Ram, E. von Lavante, and V. Hans. *Fluid Mechanics of Flow Metering*. Springer-Verlag-Berlin Heidelberg, 2005.

[17] F. Moukalled, M. Darwish, and L. Mangani. *The Finite Volume Method in Computational Fluid Dynamics*. Springer, 2016.

[18] Siemens. *User Guide STAR-CCM+*.

[19] Siemens. *Instruction Manual for Sitrans P DS III Series*, 2002.

[20] M. Simurda, L. Duggen, B. Lassen, and N. T. Basse. Modelling of transit-time ultrasonic flow meters under multi-phase flow conditions. *Ultrasonics Symposium (IUS), 2016 IEEE International*, 2016.

[21] N. C. Temperley, M. Behnia, and A. F. Collings. Flow patterns in an ultraonic liquid flow meter. *Flow Measurement and Instrumentation*, 1999.

[22] D. Um. Rapid prototyping. *Solid Modeling and Applications — 2015, pp. 191-221*, 2015.

[23] J. H. Walther. Turbulence modeling, lecture notes from applied cfd course, 41315. 04 2017.

[24] F. M. White. *Fluid Mechanics*. McGraw-Hill, 2011.

Appendices

APPENDIX **A**

First Appendix

A.1 Dimensions Of The Liner Fixture

Table A.1: Dimensions of the flow meter of the size DN20 with q_p = $2.5m^3/h$.

Length (l) [mm]	60.0
Length of body-part (l_b) [mm]	43.8
Length of reflector-part (l_r) [mm]	16.2
Outer diameter of body-part (d_o [mm]	24.4
Inner diameter of body-part (d_o) [mm]	20.4
Length of upper arms (l_{a_u}) [mm]	15.8
Length of lower arms (l_{a_l}) [mm]	14.1
Width of arms (w_a) [mm]	3.0
Length of reflector (l_r) [mm]	19.5
Width of reflector (w_r) [mm]	14.8
Angle of reflectors [°]	45

A.2 Error Estimations

Table A.2: Error estimations

Quantity	Uncertainity
ΔP	10 Pa
Q	2 l/h
D	0.5 mm

A.3 Pressure Drop Monitor

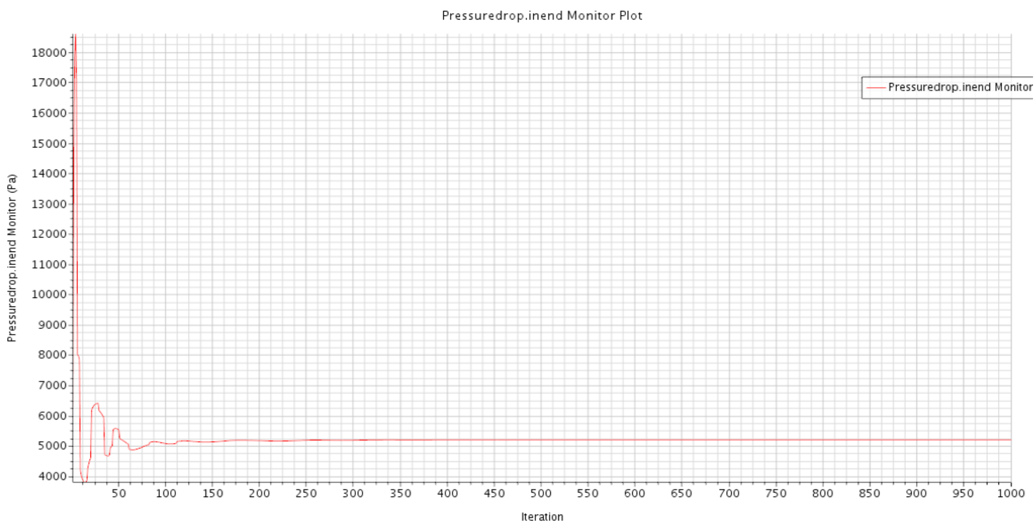

Figure A.1: An example of a pressure drop monitor.

A.4 Flow Visualization

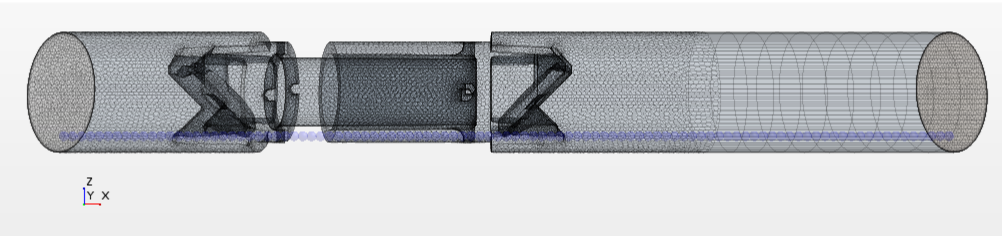

Figure A.2: A line trough the flow field, 9mm below the center on z-axis.

A.5 Validation

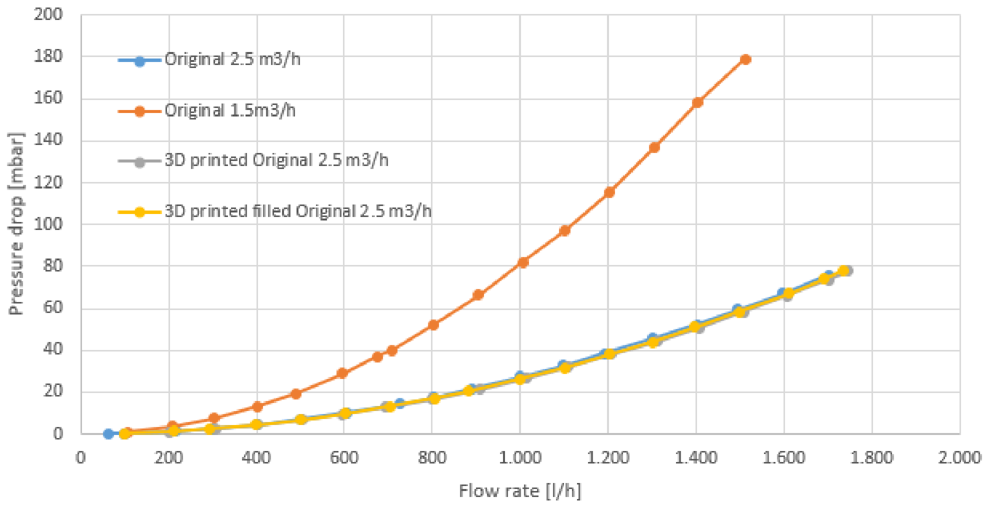

Figure A.3: Validation of the experimental results.

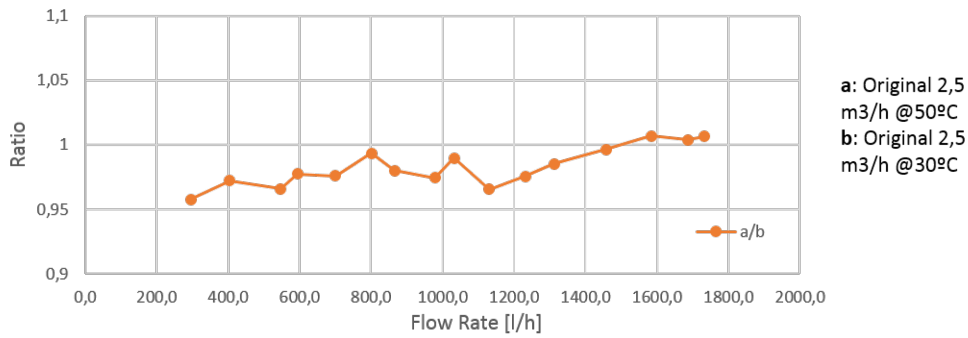

Figure A.4: Comparison of pressure drop for the original flow meter of the size 2.5 m^3/h at 30°C and 50°C.

APPENDIX B

Second Appendix

B.1 CFD Figures

B.1.1 Prototype I

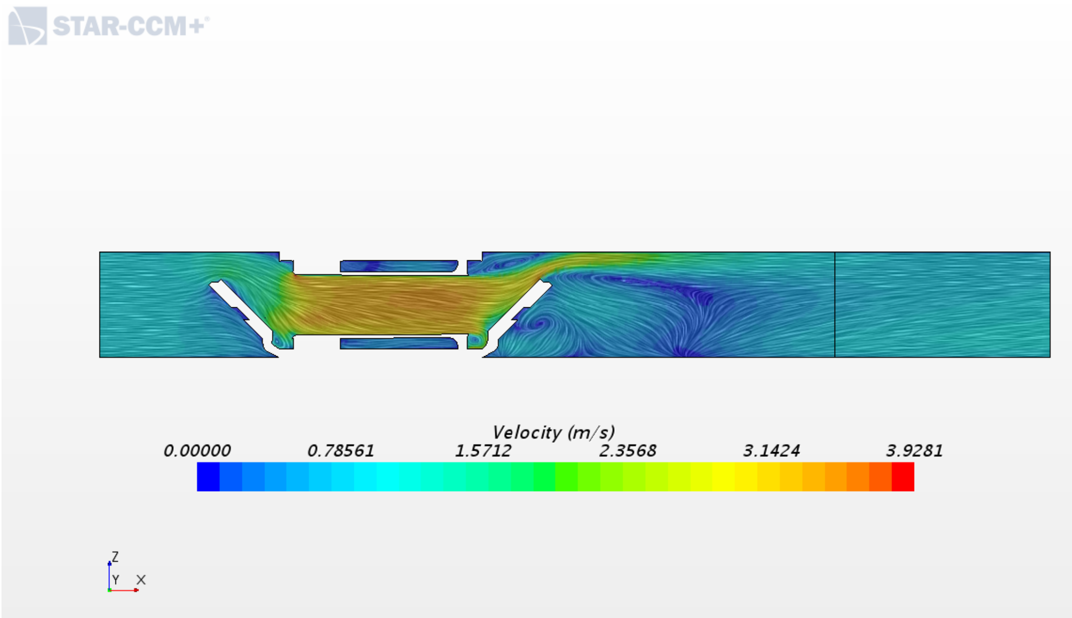

Figure B.1: The horizontal velocity field of Prototype I.

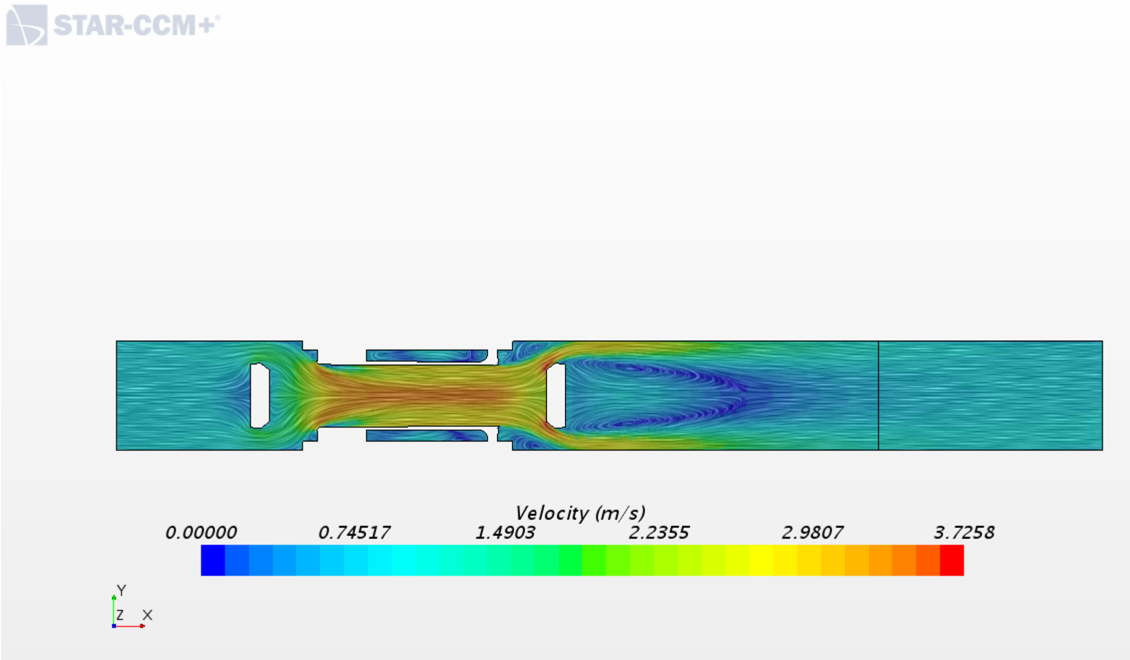

Figure B.2: The vertical velocity field of Prototype I.

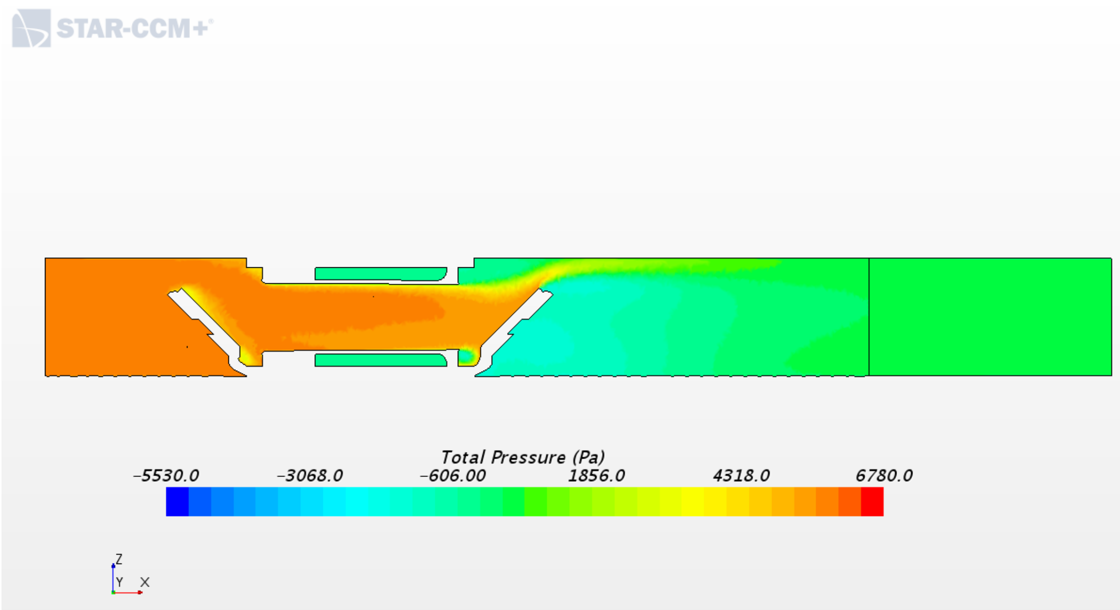

Figure B.3: The horizontal total pressure field of Prototype I.

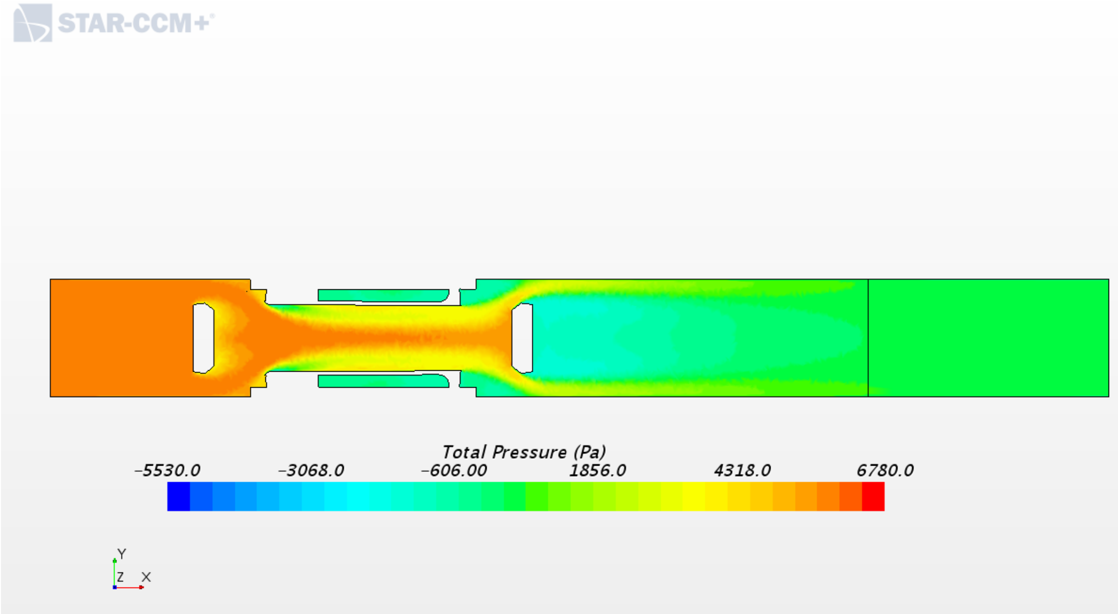

Figure B.4: The vertical total pressure field of Prototype I.

B.1.2 Prototype III

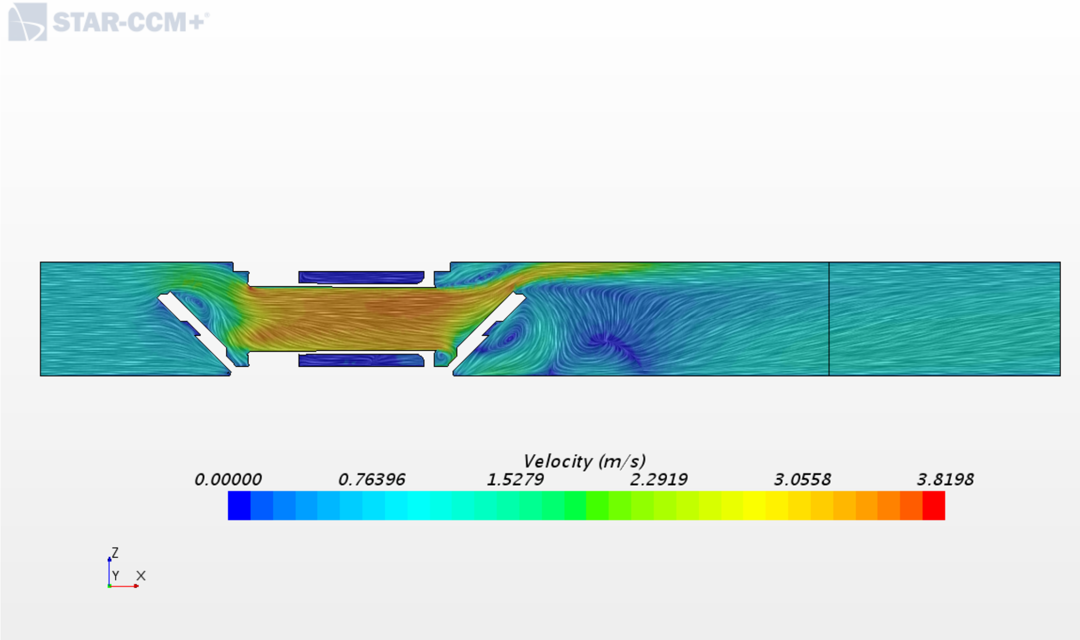

Figure B.5: The horizontal velocity field of Prototype III.

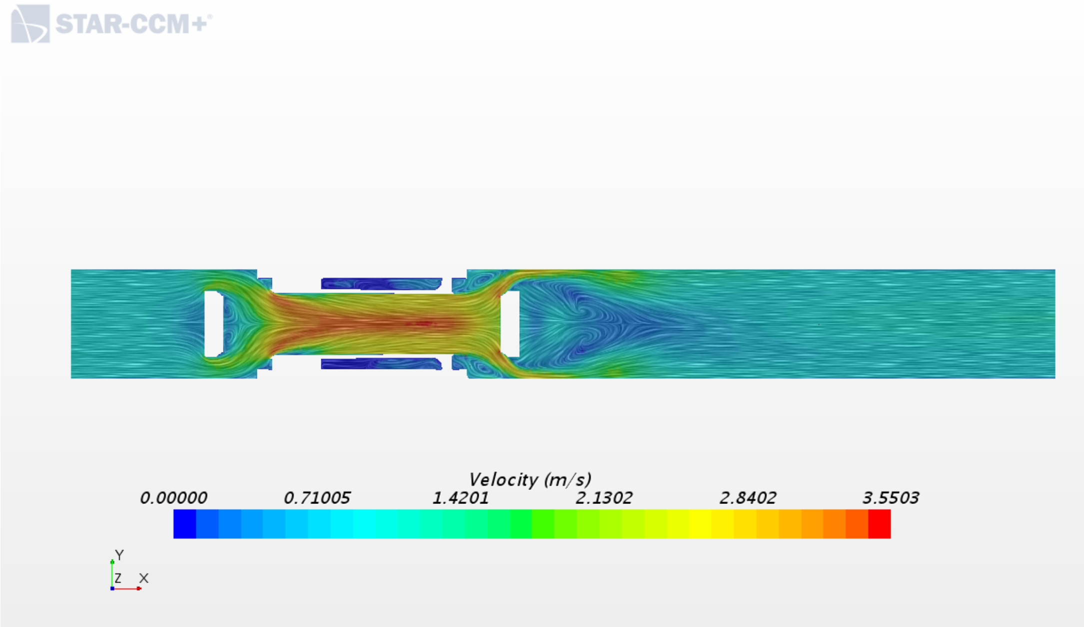

Figure B.6: The vertical velocity field of Prototype III.

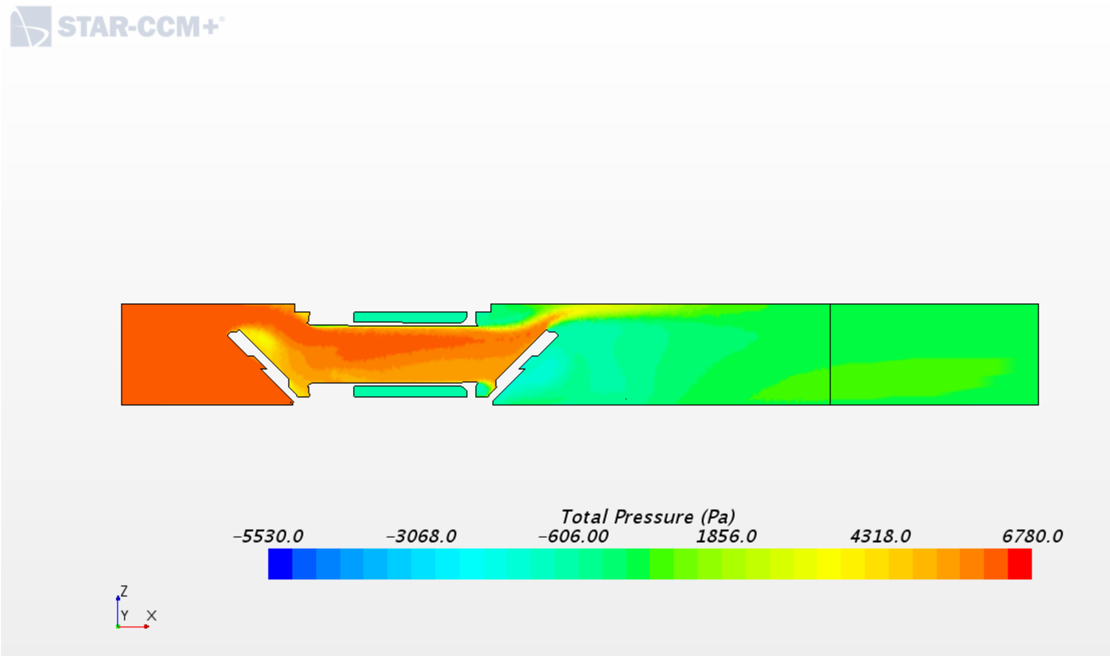

Figure B.7: The horizontal total pressure field of Prototype III.

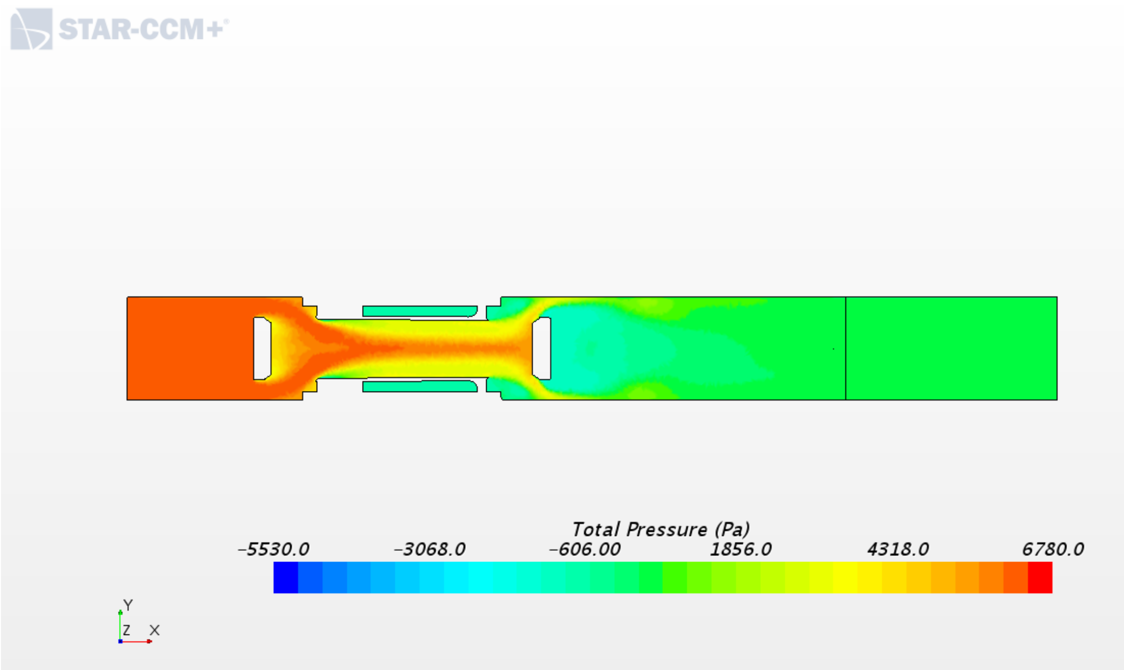

Figure B.8: The vertical total pressure field of Prototype III.

B.1.3 Prototype IV

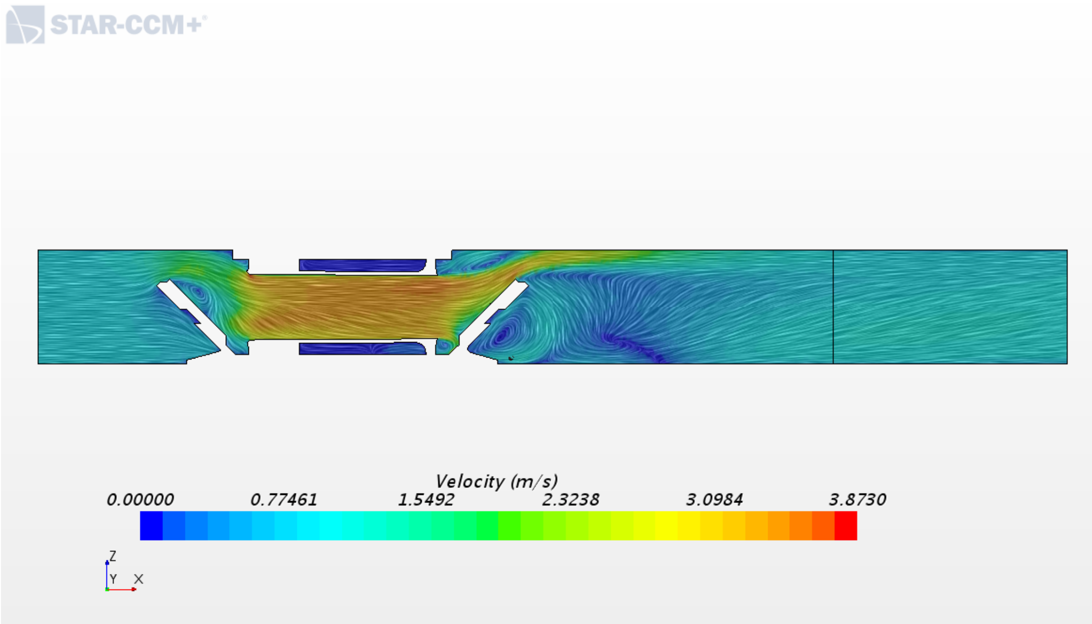

Figure B.9: The horizontal velocity field of Prototype IV.

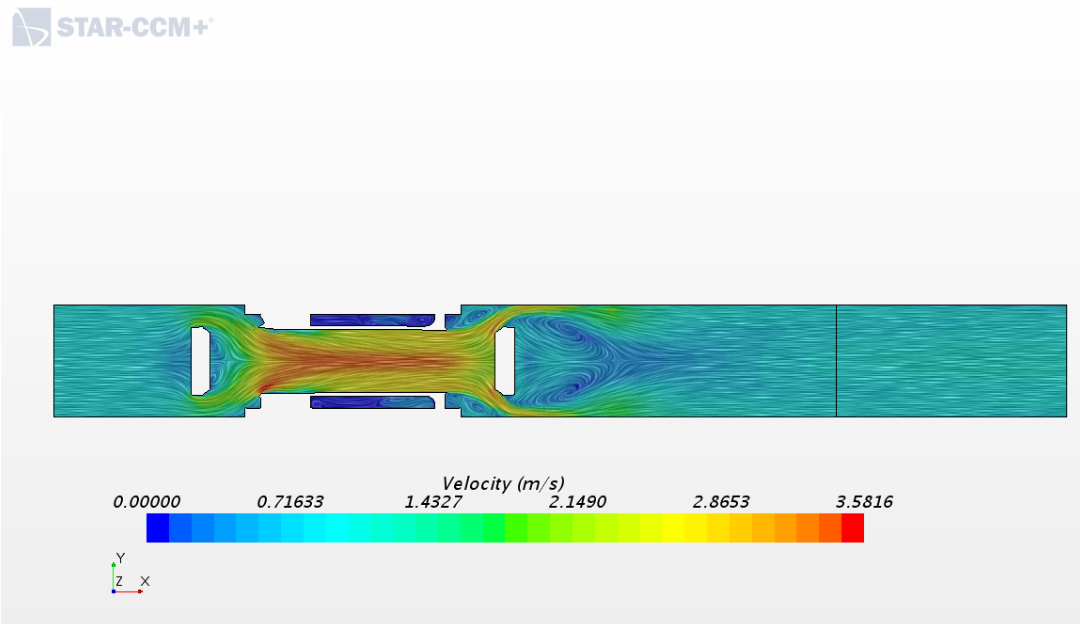

Figure B.10: The vertical velocity field of Prototype IV.

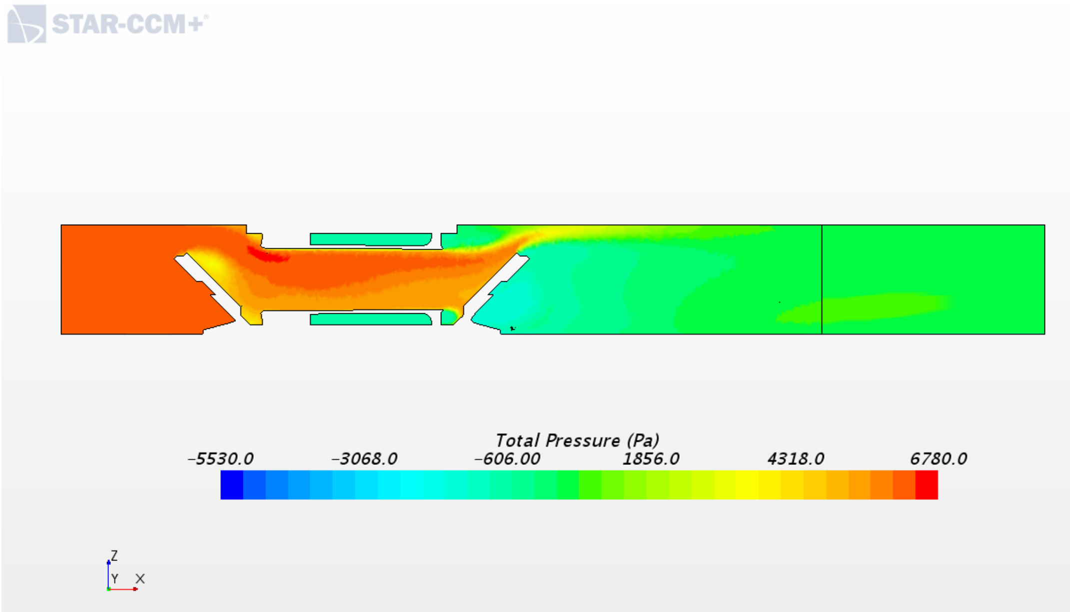

Figure B.11: The horizontal total pressure field of Prototype IV.

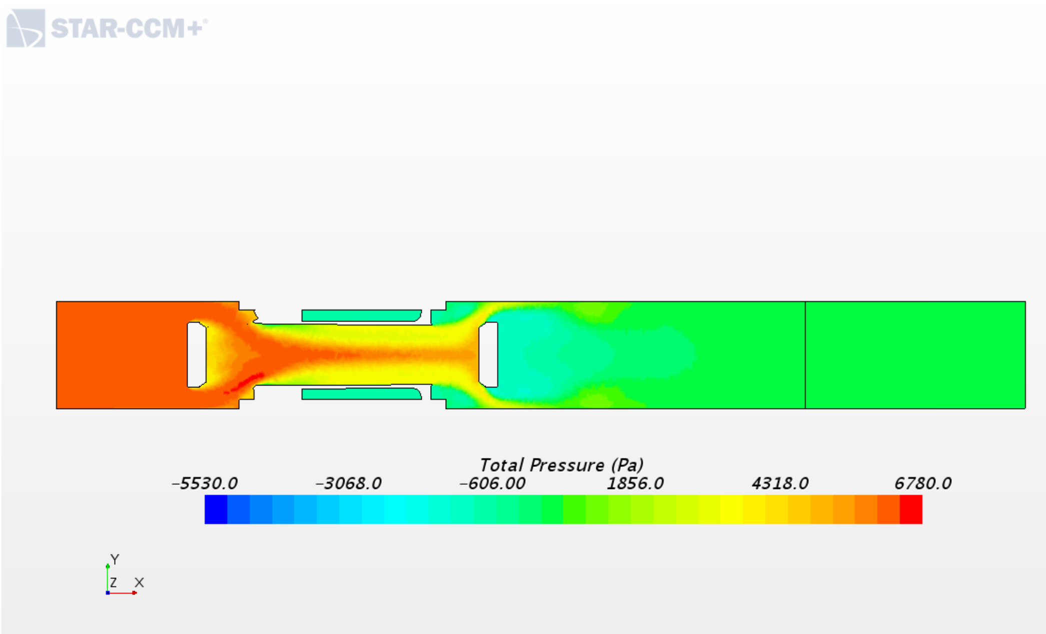

Figure B.12: The vertical total pressure field of Prototype IV.

B.1.4 Prototype V

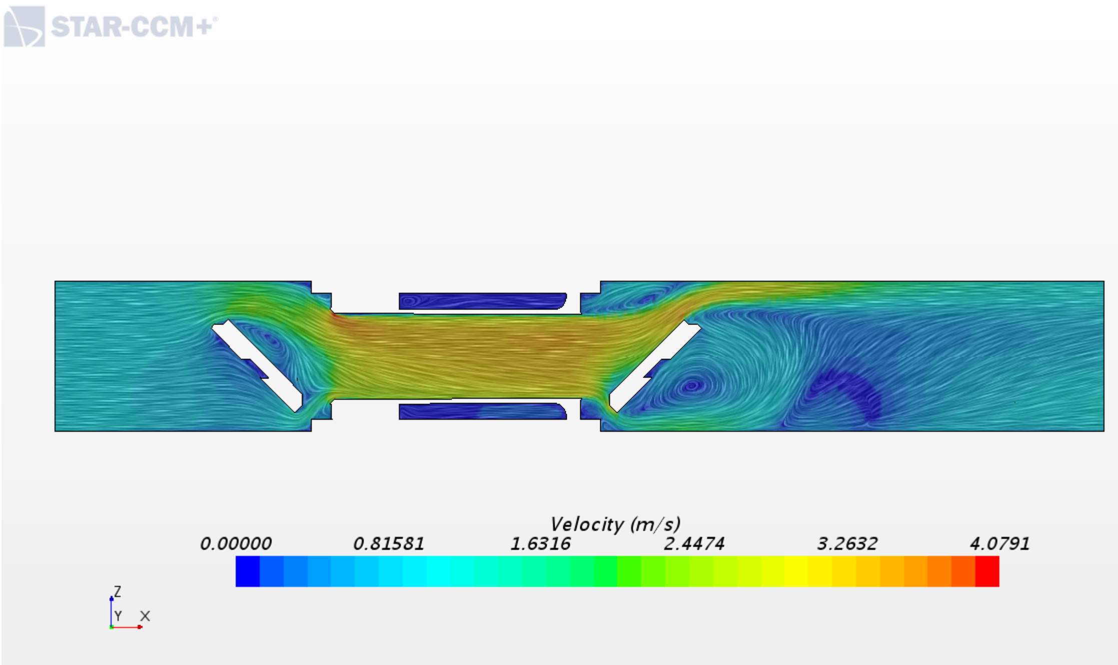

Figure B.13: The horizontal velocity field of Prototype V.

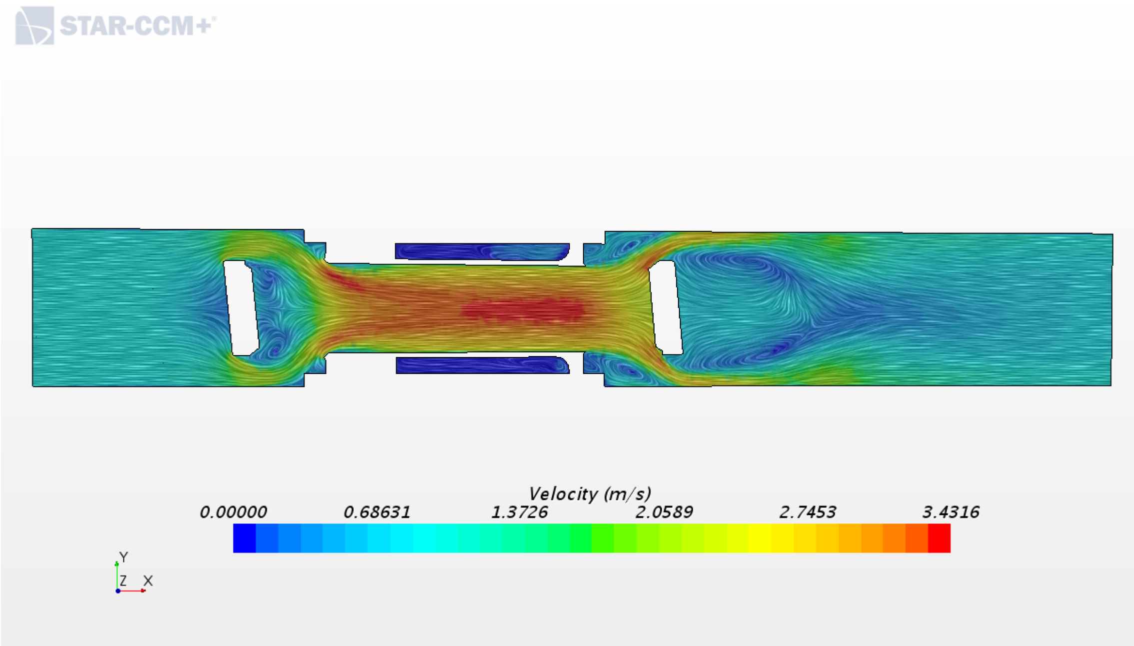

Figure B.14: The vertical velocity field of Prototype V.

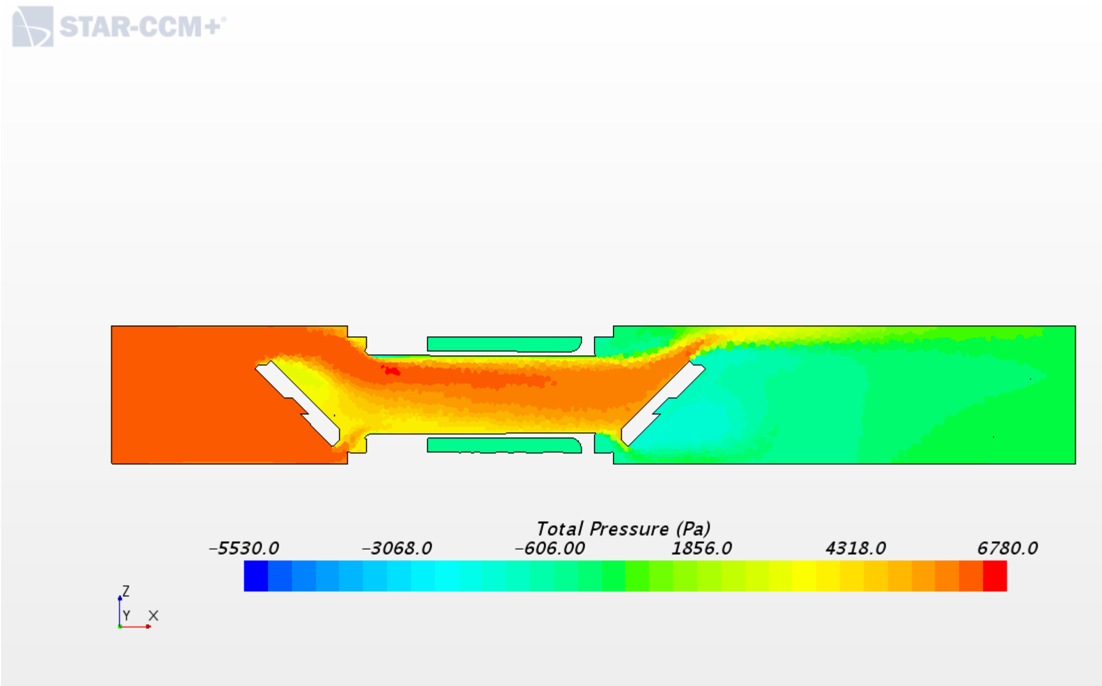

Figure B.15: The horizontal total pressure field of Prototype V.

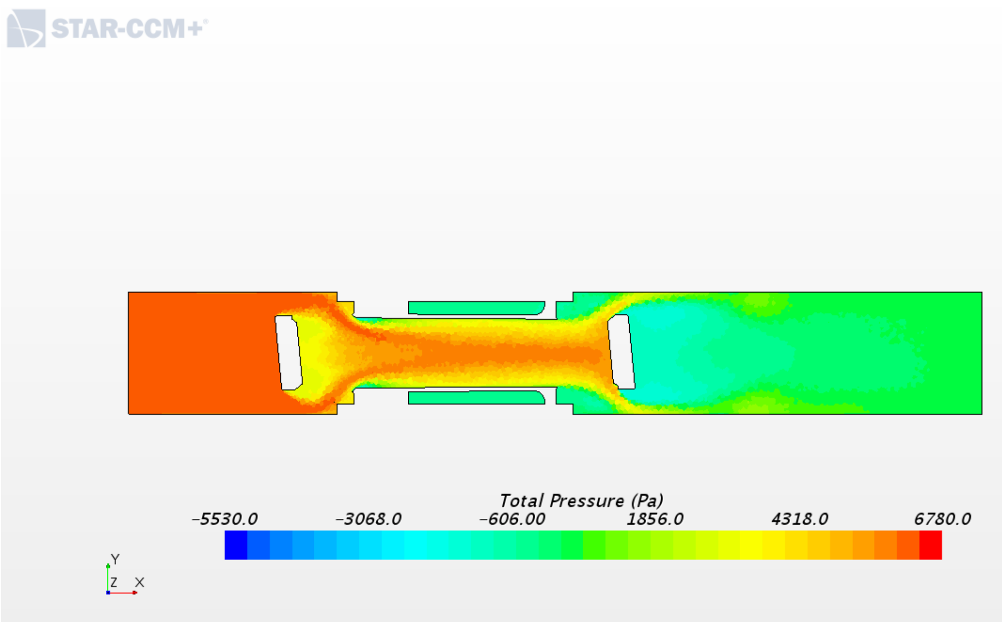

Figure B.16: The vertical total pressure field of Prototype V.

B.1.5 Prototype VI

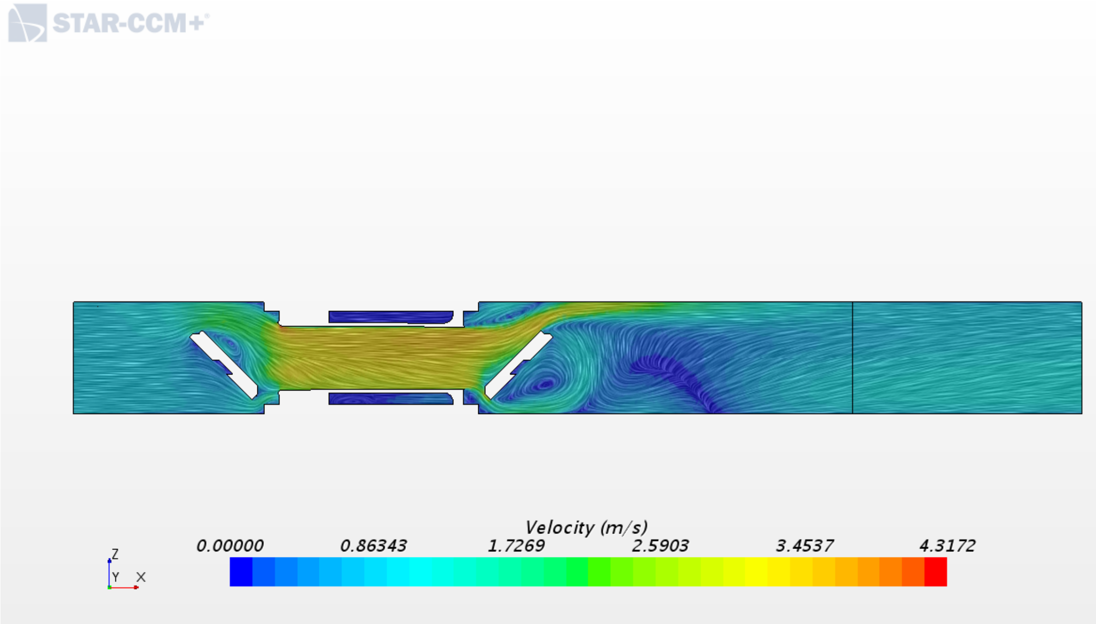

Figure B.17: The horizontal velocity field of Prototype VI.

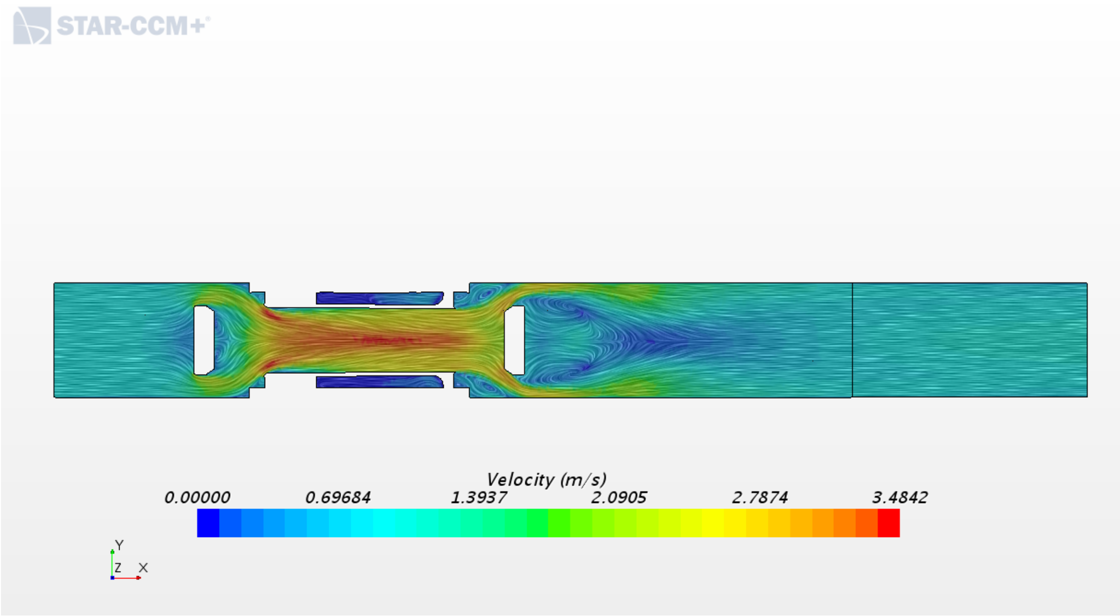

Figure B.18: The vertical velocity field of Prototype VI.

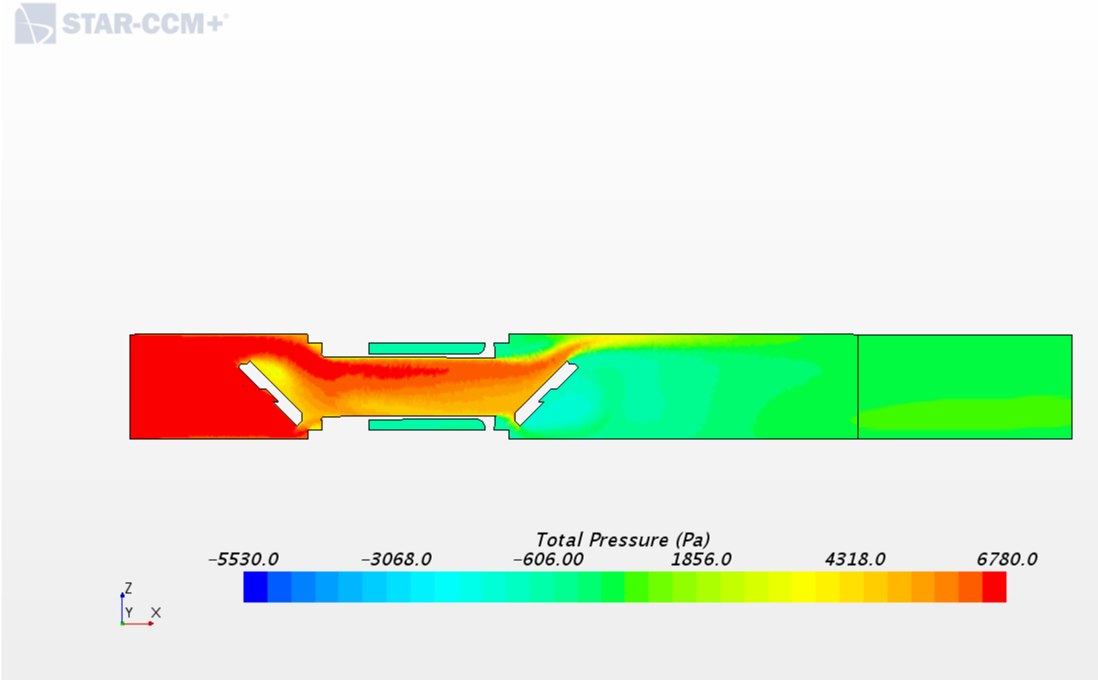

Figure B.19: The horizontal total pressure field of Prototype VI.

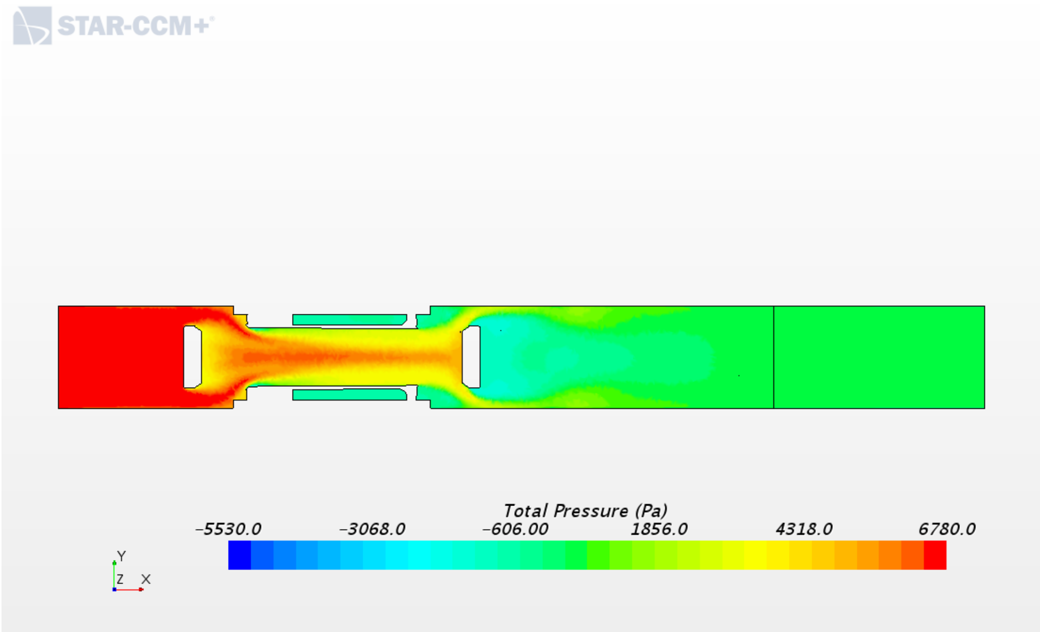

Figure B.20: The vertical total pressure field of Prototype VI.

B.1.6 Prototype VIII

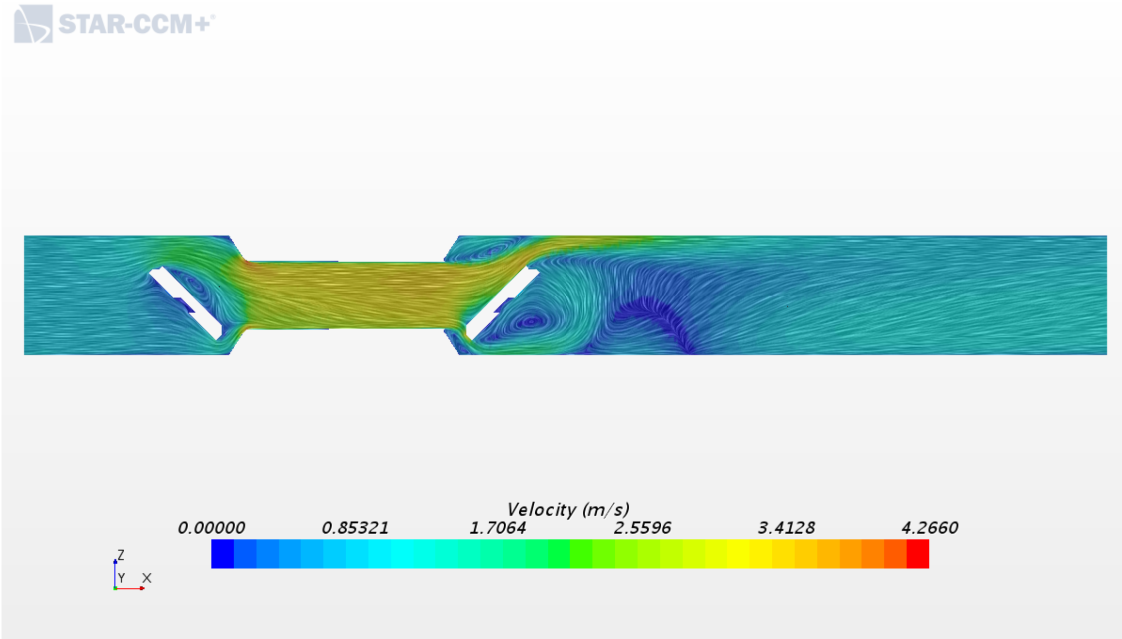

Figure B.21: The horizontal velocity field of Prototype VIII.

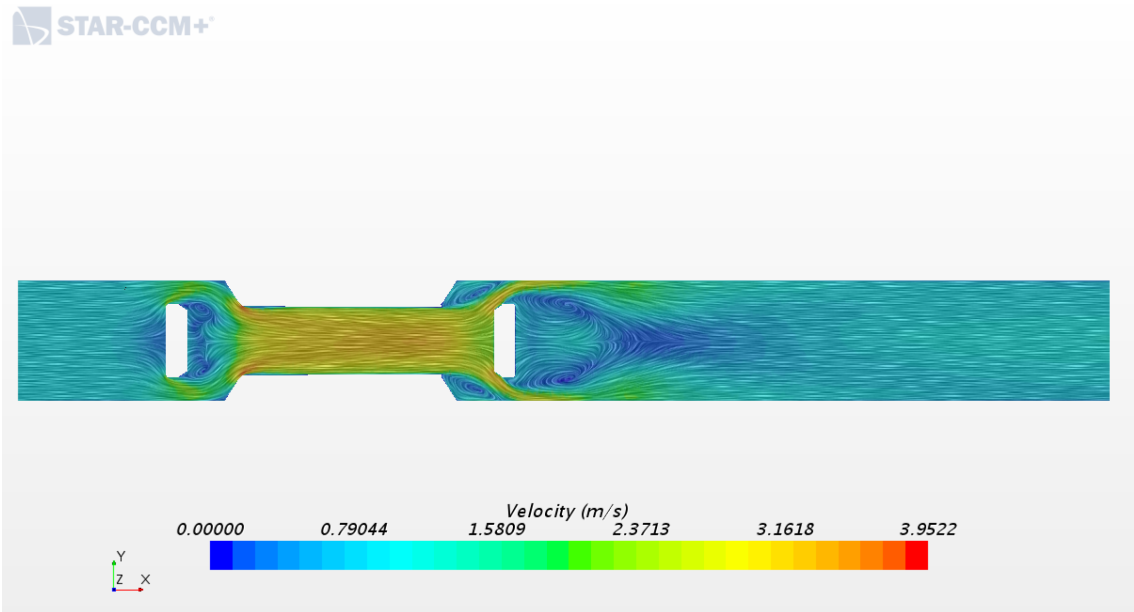

Figure B.22: The vertical velocity field of Prototype VIII.

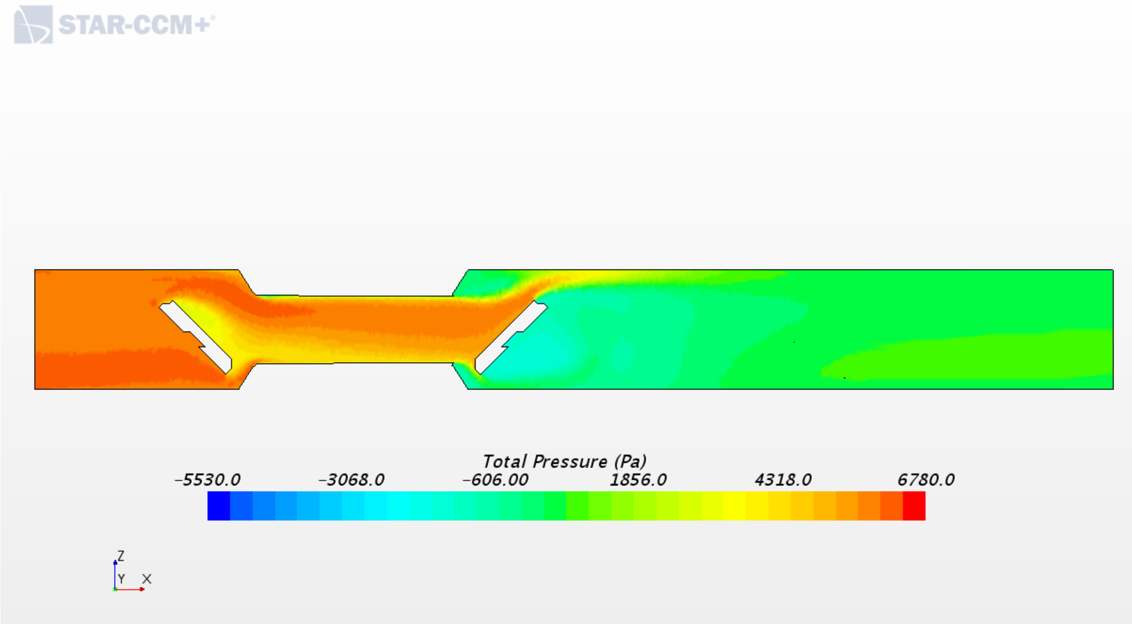

Figure B.23: The horizontal total pressure field of Prototype VIII.

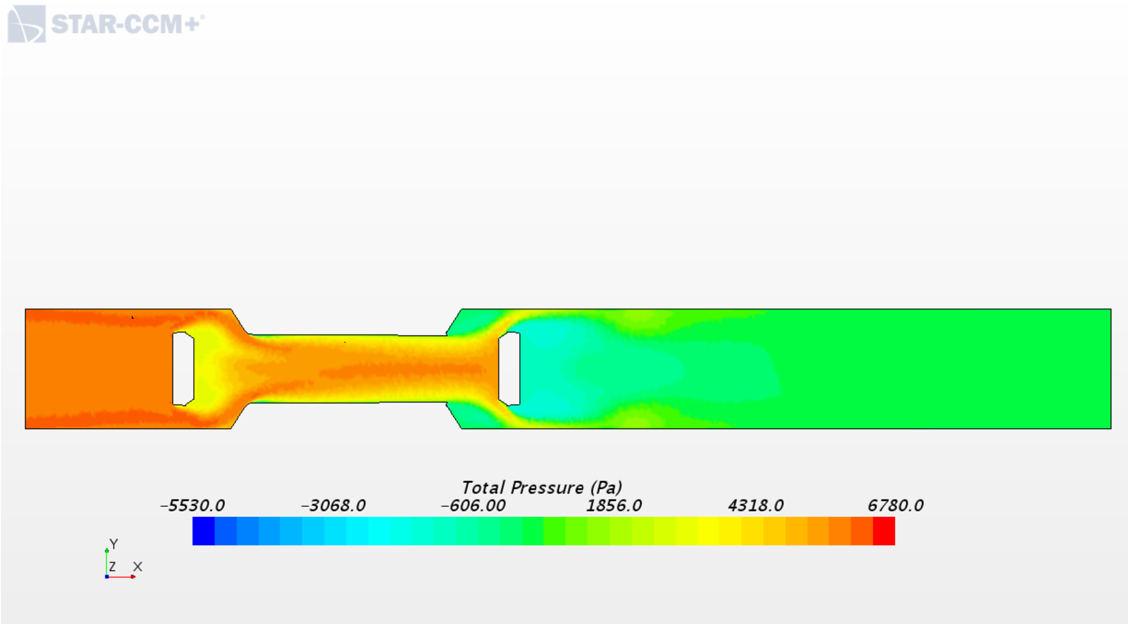

Figure B.24: The vertical total pressure field of Prototype VIII.

B.1.7 Prototype IX

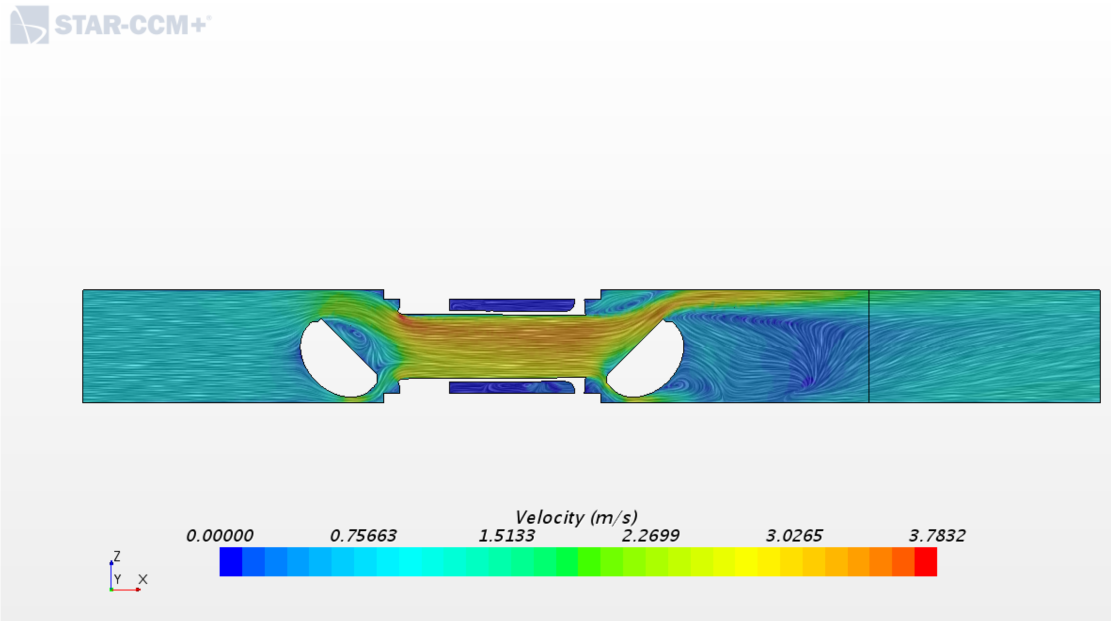

Figure B.25: The horizontal velocity field of Prototype IX.

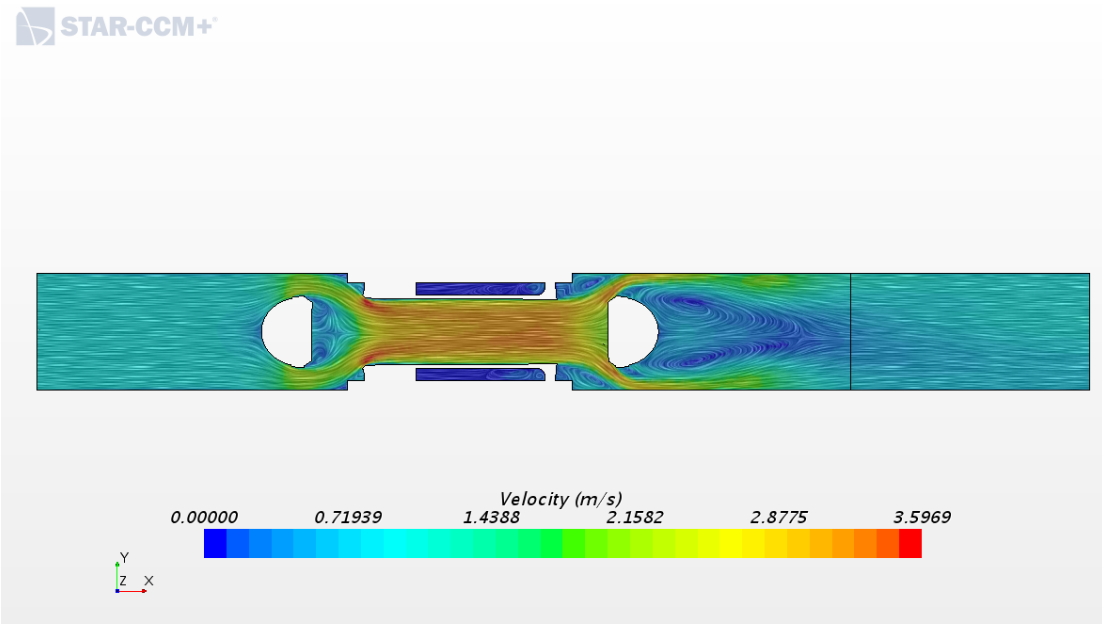

Figure B.26: The vertical velocity field of Prototype IX.

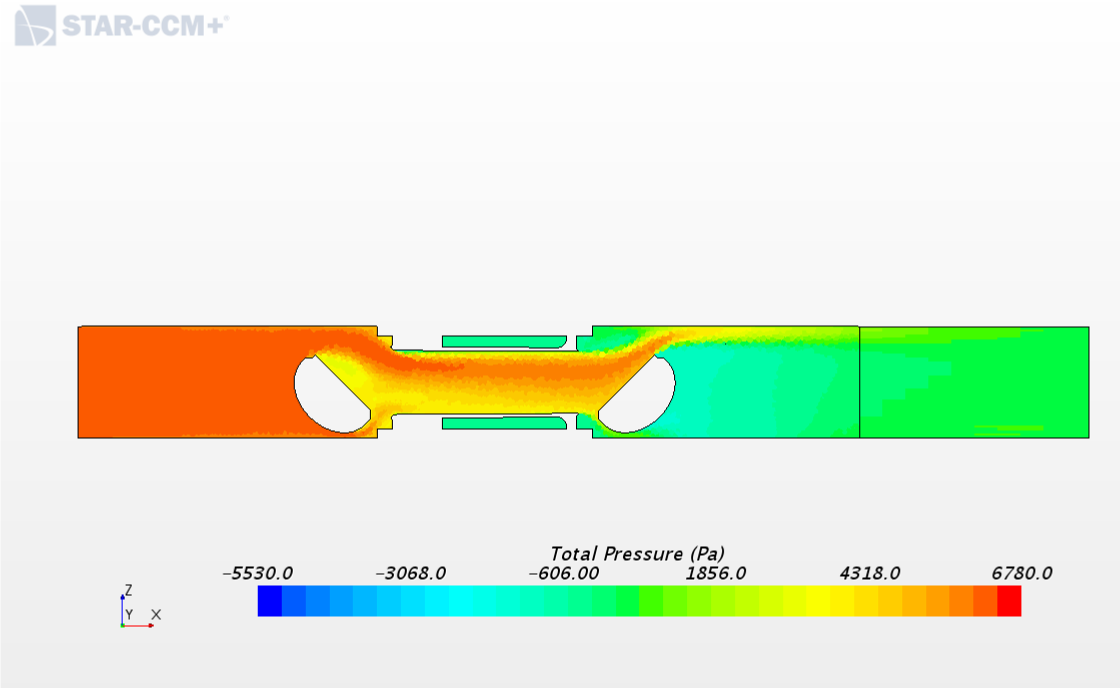

Figure B.27: The horizontal total pressure field of Prototype IX.

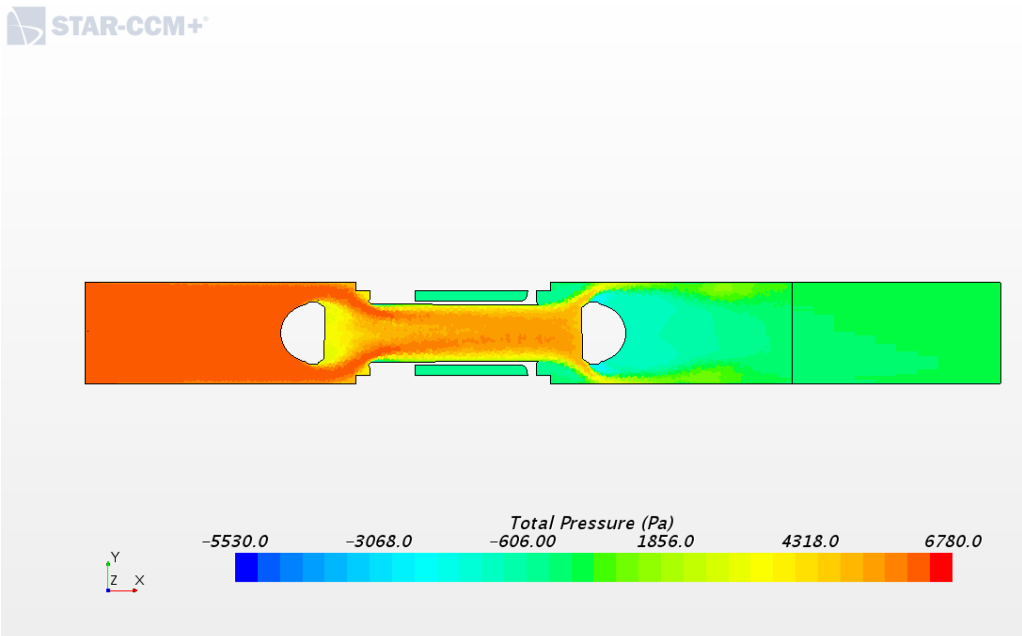

Figure B.28: The vertical total pressure field of Prototype IX.

B.1.8 Prototype X

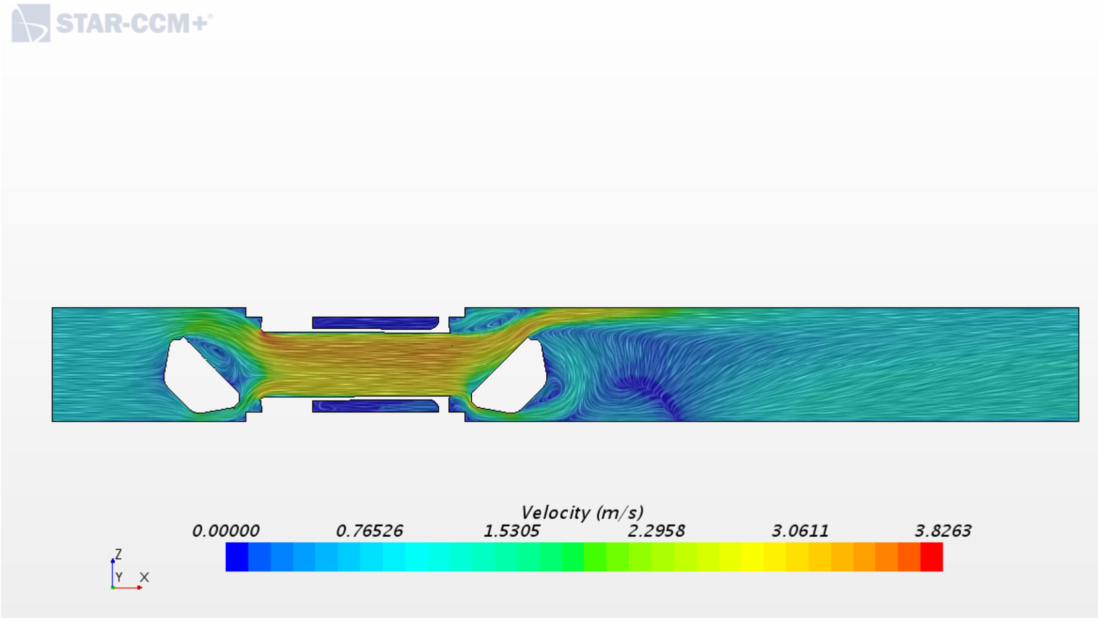

Figure B.29: The horizontal velocity field of Prototype X.

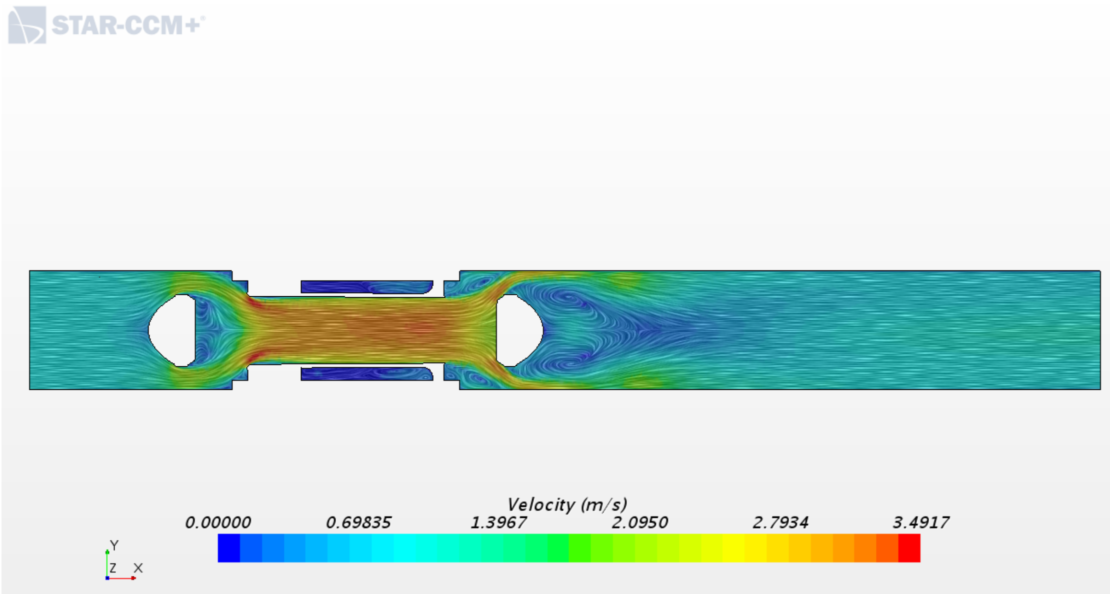

Figure B.30: The vertical velocity field of Prototype X.

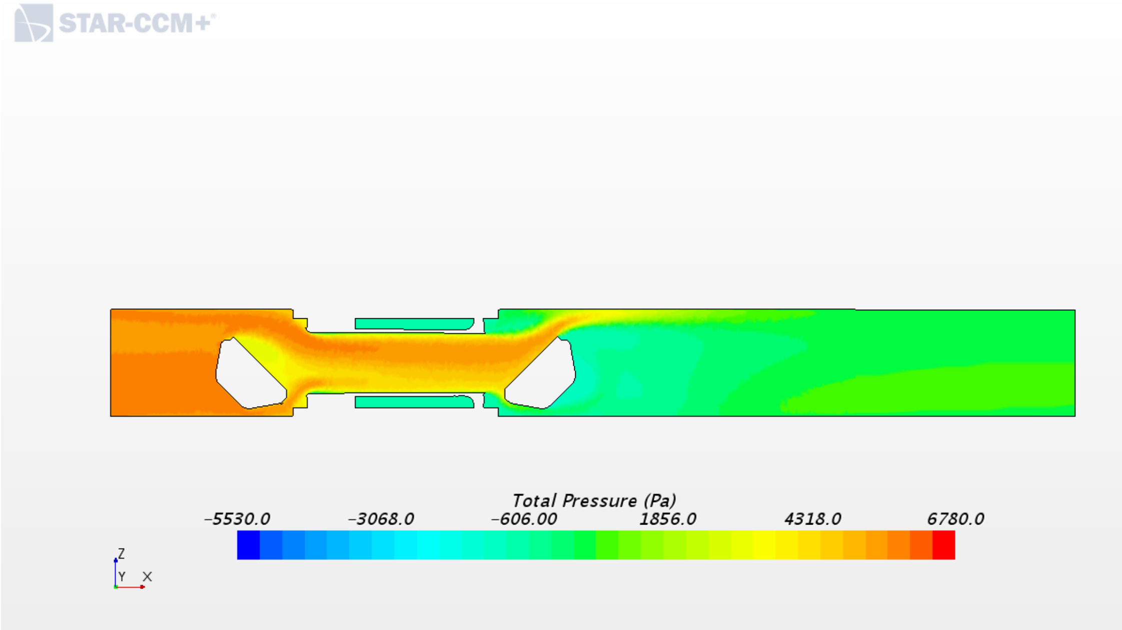

Figure B.31: The horizontal total pressure field of Prototype X.

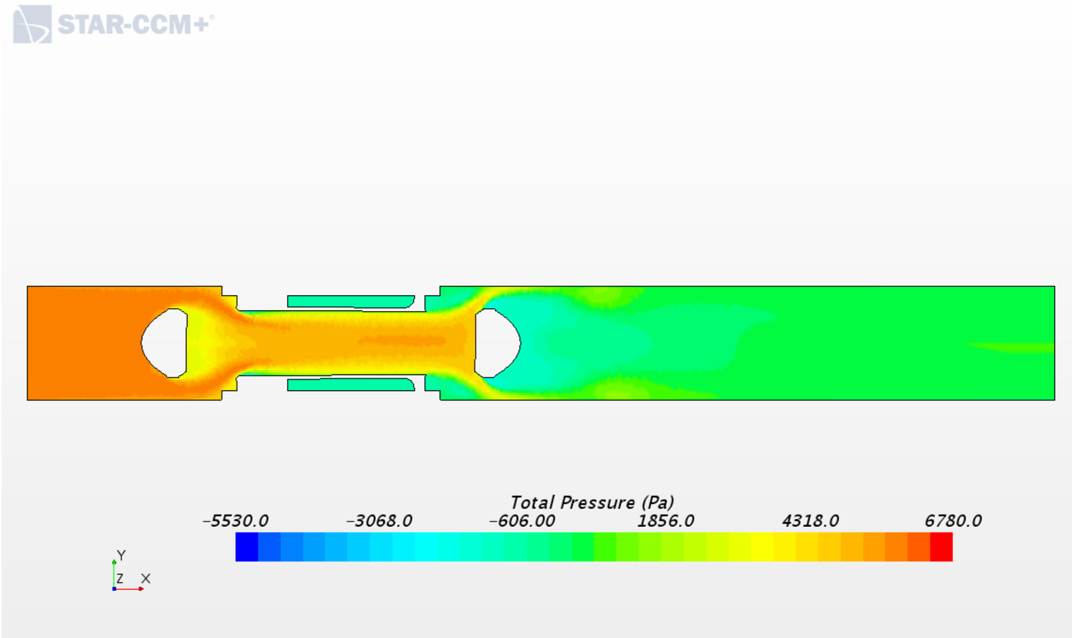

Figure B.32: The vertical total pressure field of Prototype X.

B.1.9 Prototype XII

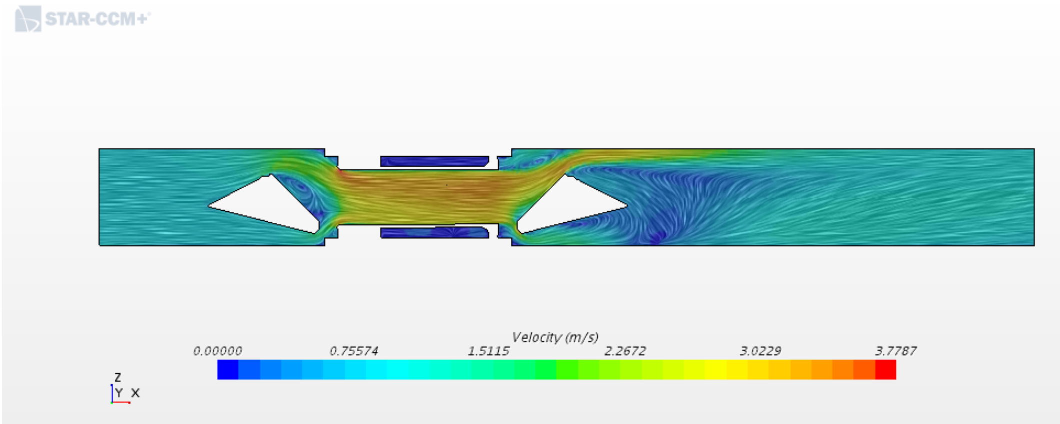

Figure B.33: The horizontal velocity field of Prototype XII.

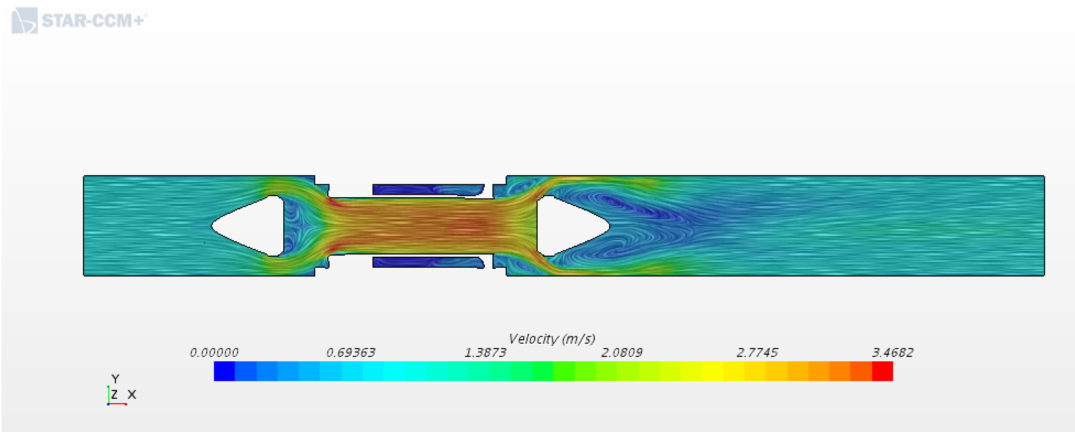

Figure B.34: The vertical velocity field of Prototype XII.

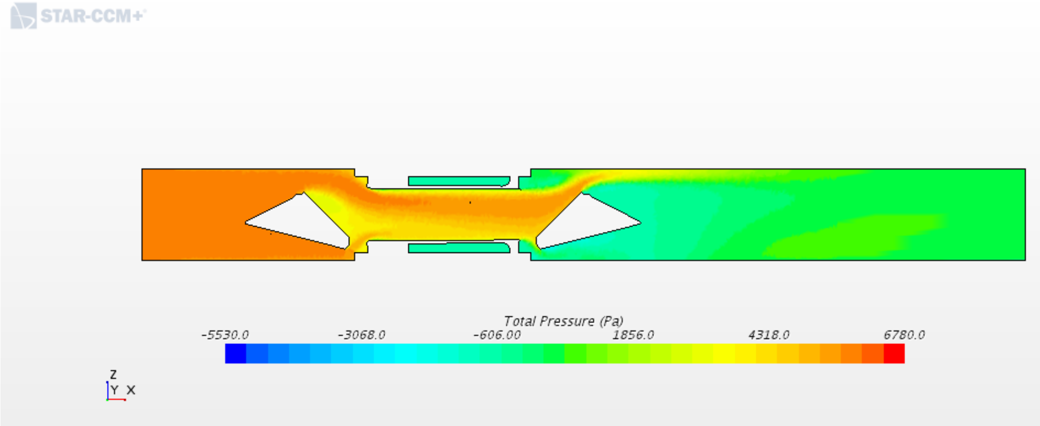

Figure B.35: The horizontal total pressure field of Prototype XII.

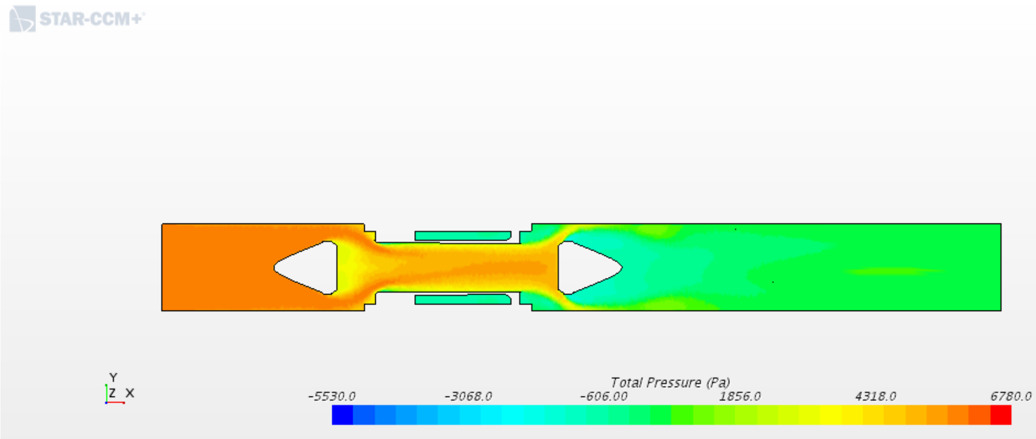

Figure B.36: The vertical total pressure field of Prototype XII.

DTU Mechanical Engineering
Section of Fluid Mechanics, Coastal and Maritime Engineering
Technical University of Denmark

Nils Koppels Allé, Bld. 403
DK-2800 Kgs. Lyngby
Denmark
Phone (+45) 4525 1360
Fax (+45) 4588 4325

www.mek.dtu.dk